FUEL UTILIZATION IMPROVEMENTS FOR HEAT PIPE MONOBLOCK MICROREACTORS

A Thesis
Presented to
The Academic Faculty

By

Aaron She

In Partial Fulfilment
Of the Requirements for the Degree
Master of Science in Nuclear Engineering

Georgia Institute of Technology

August, 2021

Copyright © Aaron She 2021

Fuel Utilization Improvements for Heat Pipe Monoblock Microreactors

Approved by:

Dr. Bojan Petrovic, Advisor
Nuclear and Radiological Engineering
School of Mechanical Engineering
Georgia Institute of Technology

Dr. Steven Biegalski
Nuclear and Radiological Engineering
School of Mechanical Engineering
Georgia Institute of Technology

Dr. Dan Kotlyar
Nuclear and Radiological Engineering
School of Mechanical Engineering
Georgia Institute of Technology

Dr. Piyush Sabharwall
Nuclear Science and Technology
Idaho National Laboratory

Date Approved: July 20, 2021

ACKNOWLEDGEMENTS

I would like to thank my advisor, Dr. Bojan Petrovic, for his guidance and patience throughout my graduate school experience. My deepest gratitude goes to Dr. Paula Gomez who has always believed, advocated, and supported me in my endeavors.

To Kyle Ramey, thank you for putting up with all my questions and pestering whenever I needed help. To Kevin Manalo, no doubt you saved me many hours of fruitless troubleshooting on the cluster, thank you.

To my brothers Nicholas and Cory, you are the best family I could ever wish for. To my mother Fawn, for your endless love and support I am forever grateful.

The majority of the work for this thesis was conducted during the Covid-19 global pandemic. I wish to express my appreciation for all the efforts of healthcare providers and frontline workers across the country and globe.

Table of Contents

List of Tables

List of Figures

Summary

Nuclear microreactors are an attractive technological concept that combine the advantages of lower capital costs and modularity to deliver reliable power generation for niche applications and remote communities that are otherwise not well served by conventional power utilities. Heat pipe microreactors use no moving parts and can operate at much higher temperatures than conventional light water reactors, which has advantages for remote operation and improved thermal efficiency. However, due to their physically small size, nuclear microreactors suffer from high neutron leakage, lowering their fuel utilization and increasing fuel cycle costs. This thesis investigates design tradeoffs to improve the fuel utilization and discharge burnup of a 15 MWth heat pipe monoblock microreactor fuel cycle, while retaining the advantages of microreactor concepts in economics and remote utility. Reactivity control is achieved using burnable absorbers, control sliders, and an emergency shutdown rod. It was found additional burnable absorber loading had a diminishing return on the cycle peak criticality while the penalty incurred to discharge burnup increased rapidly. Studies on the shutdown of the microreactor illuminated a positive reactivity coefficient due to the spectral shift of the neutron flux with increasing temperature – it is not clear if the single shutdown rod alone would be sufficient to shutdown the reactor and more studies are recommended. Heat pipe thermal operating limits were investigated. A sintered nickel wick heat pipe design is proposed that would enable the reactor to remain resilient to a failure of a heat pipe in the reactor hotspots with some margin. Finally, a simplified economic estimate suggests that the microreactor would be economically competitive and that implementing technology to improve the fuel utilization

at the cost of a longer cycle is a worthwhile tradeoff. The proposed microreactor has a fuel cycle estimated to last 25 years without refueling, with a discharge burnup of about 60 MWd/kgU.

1 Introduction

1.1 Background

Small modular reactors (SMRs) are a concept gaining renewed interest for nuclear power generation using advanced reactor technologies to provide power generation capability in modular units. SMRs vary in capacity, ranging from tens to hundreds of megawatts thermal power. The major advantages in small nuclear power generation capacity lies in reduced capital costs, small physical footprint, and the ability to be built at locations large conventional reactors cannot service [1].

Microreactors are a class of very small modular reactors (vSMRs) that typically produce between 1-20 MW thermal power [2] or between 1-10 MW electric power [3]. The potential consequences of low power microreactors is limited to on-site consequences, classifying them as Hazard Category 2 according to US regulations 10 CFR 830 [4] and DOE STD 1027 [5]. Historically, they trace their origins from space reactor designs, for instance SNAP-10A [6] or more recently the Kilopower [7] [8] reactor .

In recent years, microreactor concepts have sparked new interest for civilian use in commercial power production, and specialized applications for military or space. Microreactors target niche power markets needs that are largely untapped or unserviceable by conventional means of power generation. Remote regions, island communities, and in-situ process heat applications are all potential target applications for microreactors. Given the very different markets and objectives they aim to fulfil, microreactors must be designed for their target application in mind, namely affordability, reliability, flexibility, and sustainability [8]. Designs compact enough to fit on a flat-

bed truck could potentially be transported to any location accessible by road. Due to their lower power output, they may also be easier to incorporate into existing electrical grid infrastructure.

There are several ongoing commercial microreactor efforts across the globe. In Russia, Uniterm [9] and SHELF are ~30 MWth microreactor concepts using UO_2 fuel with water for moderation and cooling [10] [11], with fuel burnup of 115 and 160 MWd/kgU respectively [10]. Hydromine Nuclear Energy is developing the LFR-TL-X lead cooled fast reactor, with different models rated at 15/5, 30/10, and 60/20 MWth/MWe [10]. The reported discharge burnup of LFR-TL-X is about 40 MWd/kgU [10]. SEALER is another low power (8/3 MWth/MWe) reactor under development by LeadCold in Sweden, with a discharge burnup of 33 MWd/kgU [10]. In Japan, the 4S reactor is a sodium cooled fast reactor with a discharge burnup of 43 MWd/kgU and long design life of 60 years [10]. The microreactor concept most similar to this thesis is Westinghouse's eVinci microreactor, which has a discharge burnup of about 30 MWd/kgU [10] [12]. Like eVinci, this concept reactor is a monoblock type reactor with heat pipes and external reactivity control. summarizes similar commercial microreactors in development (non-exhaustive) that are designed for 30 MWth power or less [10] [11] [12].

Table 1-1. Comparison of < 30 MWt Microreactors Under Development (from [12])*

Reactor	Uniterm	SHELF	4S	LFR-TL-X	SEALER	eVinci	This Project
Institution	NIKIET	NIKIET	Toshiba	Hydromine Nuclear Energy	LeadCold	WEC	N/A
Country	Russia	Russia	Japan	Luxemborg	Sweden	USA	N/A
Power (MWt/MWe)	30/6.6	28.4/6.6	30/10	15/5 30/10 60/20	8/3	0.4-40 / 0.2-15 5/15*	15 / 5
Fuel Type	UO_2 CERMET	UO_2 pellet	U-Zr alloy	LEU	UO_2	UO_2 or UN	UN
Enrichment	19.75%	19.7%	<20%	19.75%	19.75%	19.5%	19.75%

Table 1-1 continued							
Coolant	Water	Water	Sodium	Lead	Lead	Na or K heat pipes	Na heat pipes
Spectrum	Thermal	Thermal	Fast	Fast	Fast	Epi-thermal	Thermal
Moderator	Water	Water	N/A	N/A	N/A	Metal hydrides	YH_2
Reactivity Control	Soluble boron, control rods	Control rods	Moving reflector	External flag-type movable absorber	Control rods	Control drums, burnable absorbers	Control sliders, burnable absorbers
DBU (MWd/kgU)	115	160	34	40	33	~30	~60
Cycle length/ Lifetime	200 mo. 25 yr.	6 yr. 60 yr.	- 60 yr.	~100 mo. 30 yr.	- 27 yr.	- 10 yr.	- ~15 yr.
Dimensions (diameter – height)	2.9 m 9.8 m	8 m 14 m	3.5 m 24 m	2 m 3.5 m	2.75 m 6 m	Not given	2.1 m 2.1 m

The advantage of heat pipe monolithic microreactors lies in their simplicity. Heat pipes are entirely passive heat transfer devices. Combined with solid fuel rods embedded in a solid structural monoblock, these reactors are “solid state” reactors with minimal moving parts [8]. Simplicity in design and eliminating moving machinery facilitates manufacturing and transportation.

In a heat pipe microreactor, the main mechanism by which heat is removed from the core is by a phase change in the working fluid of the heat pipe, typically Na, K, or Li. Heat is transferred via conduction from the core into the heat pipe walls, which transfers that heat to the heat pipe working fluid in contact with the inner walls [13]. The resulting vapor travels along the length of the heat pipe, out of the core, eventually condensing back into a liquid state by releasing latent heat. The liquid is then carried back into the core via gravity or capillary action via a wick. This method of heat removal for reactors is well studied; Los Alamos National Lab (LANL) has several decades (since 1963) of experience and research heritage with liquid metal heat pipes [13]. Heat pipes tend to work very well in their designed operating temperature range, but can encounter problems when

subject to conditions outside their functional limits [14]. Heat pipes in microreactors should be designed to operate well within functional limits such that a failure in one pipe will not cause a cascading failure of the surrounding heat pipes as they take up the thermal load of the failed pipe. To that end, Idaho National Lab's MARVEL (Microreactors Applications Research, Validation, and Evaluation) and MAGNET (Microreactor Agile Non-nuclear Experimental Test Bed) facilities under development will be critical for enabling heat pipe technology in microreactors [15].

Compared to conventional light water reactors (LWRs) which have relatively inexpensive fuel, microreactors' fuel costs are expensive and comprise a significant percentage of the total cost. Various approaches are used to improve the fuel utilization and discharge burnup. Increasing the enrichment increases the fissile inventory loaded in the core; but HALEU fuels cost significantly more than LEU fuels. Higher operating temperatures afforded by heat pipes may help offset the increased fuel costs by running power conversion systems at higher thermal efficiency. The neutron energy spectrum of a microreactor is highly influential on the design and utilization of the fuel. Thermal spectrum reactors have better neutron economy, whilst fast spectrum reactors typically designed as space microreactors are smaller/lighter and simpler in design

In general, heat pipe monoblock microreactors, like all physically small reactors, suffer from poor fuel utilization due to high neutron leakage. Civilian or commercial designs necessitate the use of low enriched uranium (LEU), which in turn incentivizes the use of a moderator to thermalize neutrons. Solid metal hydride moderators like zirconium or yttrium hydride must account for hydrogen migration; hydrogen atoms tend to relocate in the crystal structure of the moderator material due to temperature differentials [16]. To combat neutron leakage, the core is typically surrounded by a neutron reflector like beryllium oxide, stainless steel, alumina, or graphite [8]

[17]. Beryllium oxide is typically the best-performing reflector material due to its high moderating power and ratio, low neutron energy threshold Be(n,2n) reaction, and high temperature tolerance.

Since microreactors aim to target niche and remote markets, refueling/multi-batch fuel cycles are not possible. To attain longer fuel cycles, a good deal of excess reactivity is incorporated into the fresh core, which must be suppressed. Reactivity control methods range from conventional control rods to more unusual concepts such as control drums, sliding reflectors, hinged reflectors, and control shutters or petals [8]. Excess reactivity is also controlled with burnable absorber materials incorporated into the fuel [18]; the choice of element/isotopes and mass loading of burnable poisons is strongly dependent on the neutron spectrum and design of the core. The penalty to the discharge burnup of the fuel cycle must be carefully quantified and compared against the reactivity control attained with a particular burnable absorber control scheme.

Perhaps the largest problem microreactors face is their low fuel utilization. Low fuel utilization drives up costs overall; no matter how attractive or elegantly designed a reactor is, it will not be built for commercial enterprises unless it is economic. Due to their small size, microreactors suffer from high neutron leakage and poor neutron economy, leading to low fuel burnup and short cycle lengths. This thesis aims to develop strategies to improve the neutronic efficiency of microreactors, thereby increasing fuel utilization and reducing costs to make microreactor concepts more economically competitive.

1.2 Objectives

Any nuclear engineering design effort cannot hope to solve all the problems presented. The scope of the thesis research shall be limited to problems that are both tractable and important to resolve. Some aspects of the design will remain fixed, both to restrict the scope and to impose some reasonable limitations/requirements that a successful design must stay within/meet.

The objective of this effort is to improve the fuel efficiency of a thermal spectrum heat pipe-monoblock microreactor concept. Various measures to improve the neutronics and cost-savings of the reactor design will be undertaken and analyzed. This research will propose techniques to improve the economic competitiveness of microreactors from a fuel utilization perspective. The operating limits of heat pipes are found and heat pipe design is driven by redundancy in the case of a complete failure of the heat pipes in the hot spot of the reactor.

The thermal power of the reactor will be set to 15 MW. Since a major attractive feature of microreactors is their compactness, the dimensions of the reactor will be limited such that it can be transported on a typical flatbed truck. For commercial and civilian use, the enrichment must remain at 19.75% or below. Fuel cycle costs and the cost of electricity will be evaluated to determine cost drivers and trends, giving insight on how to bring microreactors to market.

Above all else, any nuclear reactor design must be safe. Therefore also included in the scope are heat pipe failure, excess reactivity and reactivity control. Safety from a thermal hydraulic standpoint will be dealt with by heat pipe failure analysis. The shifted thermal load of a failed heat pipe will be calculated to ensure neighboring heat pipes have not exceeded their functional operating limits. Reactivity control will be investigated with various configurations of moveable control surfaces and burnable absorbers. Since a long cycle length is desired for economic competitiveness, the core will be loaded with a good deal of excess reactivity that must be suppressed with burnable absorbers. The effect of burnable absorber on cycle length and discharge burnup must also be quantified and justified by cost. Passive criticality safety is highly desirable. Reactivity control is achieved through the combined use of burnable absorbers mixed in fuel, boron fuel coatings, and adjustable external control sliders.

1.3 Requirements and Metrics

Several aspects of the reactor concept will be designated as requirements that must be met to be considered a viable design. Most prominent among them would be safety related requirements, but also include requirements to ensure the competitiveness of the microreactor concept. Safety-related requirements include:

- The reactor must be able to be made passively safe and shutdown in the event of an accident
- Temperatures cannot exceed material limits (eg: fuel centerline temperature to not melt fuel)
- Singular heat pipe failure must not lead to a cascading failure or inability to remove heat

Likewise, there are several design-related requirements imposed. These limit the design space such that any concept that cannot meet these requirements would be excluded from further consideration.

- Discharge burnup of at least 50 MWd/kgU
- Minimum reactor fuel cycle lifetime of 10 years
- Maximum size of the reactor itself must be small enough to fit on a flatbed truck (excluding primary/secondary heat exchange loops and power conversion system)
- Thermal power of 10 MWth
- Reactor operating temperature must be high enough for sodium heat pipes to operate in their optimal range (with some margin for safety)

Closely related to the requirements are the metrics used to evaluate and quantify how the reactor concept adheres to the requirements. Metrics such as reactivity control or power density can be

measured directly from neutronics simulations, while others would be evaluated/estimated using other methods. Metrics such as fuel cost or discharge burnup quantify the economic competitiveness of the reactor concept. The metrics used in this thesis are:

- Discharge burnup of fuel
- Estimation of manufacturing and fabrication costs
- Breakeven cost of the reactor for a given electricity market

1.4 Design Parameters

The reactor concept studied comprises a solid monoblock with channels running axially through the block for fuel pins, moderator rods, and heat pipes. A hexagonal lattice structure divides up the core into 6 rotationally symmetric sectors with fuel, moderator, and heat pipes distributed all throughout. An axial and radial reflector improve the neutron economy and fuel utilization. The heat pipes continue through the upper axial reflector to a heat exchanger and power conversion system and the core is not symmetric axially across the midplane. The upper reflector is “spongy” and full of holes that accommodate the extra length of the adiabatic section of the heat pipes. Within the radial reflector are the control sliders used to regulate the excess reactivity. A large empty channel is set in the center of the core to serve as the emergency shutdown control rod, which could be spring-loaded or held back by tension outside its channel and insert automatically in the event of a loss of power to the core. The core is oriented horizontally/flat to the ground (due to heat pipe considerations in that the vertical liquid pressure drop in heat pipes is too much in a vertical position), so gravity cannot automatically insert the shutdown rod.

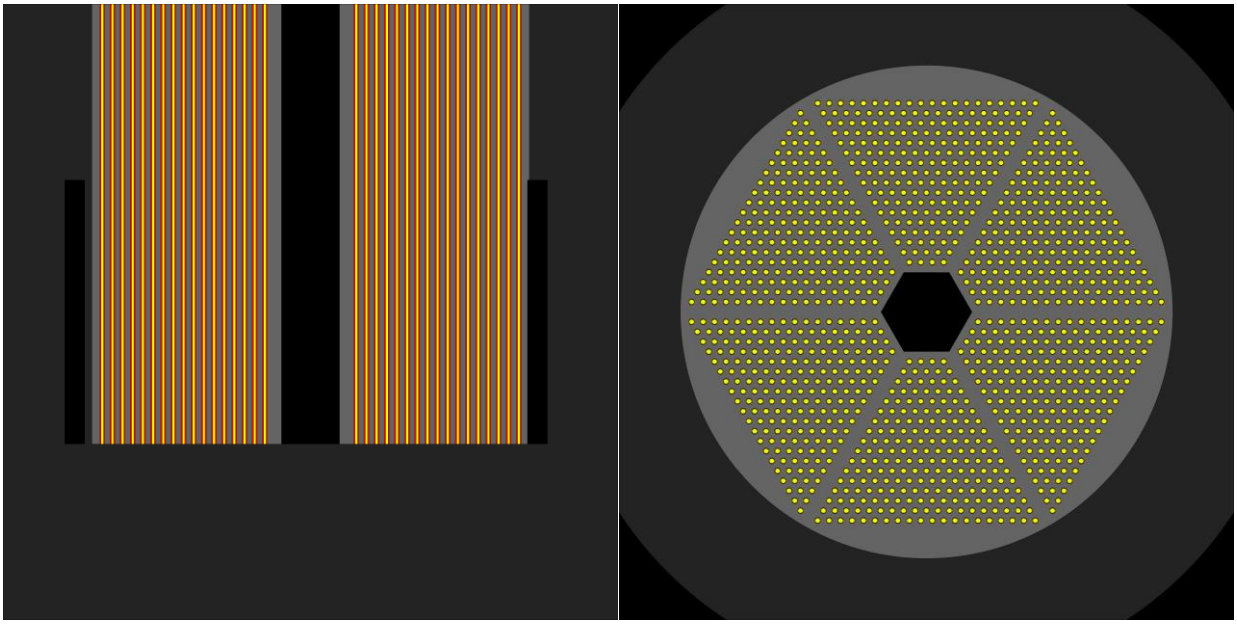

Figure 1-1. Axial (left) and radial (right) view of reactor, showing heat pipes penetrating through one side of the axial reflector.

To improve the neutron economy, a reflector is included radially and axially around the core. Reflector materials suitable for microreactor applications include beryllium, beryllium oxide, stainless steel, graphite [19]. Space nuclear applications value weight and neutronic performance over cost, whereas commercial microreactor concepts explored here must be economic. Various reflector materials and thicknesses are examined and evaluated against the neutronics benefit vs. cost to select the most economically attractive reflector parameters.

The heat pipe selected is a sodium coolant heat pipe. This was chosen based on the operational experience from Los Alamos National Lab gained in various long duration heat pipe experiments that justified the long-term performance and lifetime of these heat pipes [13]. Sodium also has a fairly low neutron absorption cross section, reducing parasitic neutron losses, and high boiling point, which allows the reactor to run at a higher thermal efficiency. Lithium may also be a feasible choice by contributing to neutron moderation thanks to the low atomic number of lithium-7. However lithium has a high boiling temperature of 1615 K (other solid materials in the reactor

may not tolerate this high temperature well) and requires high enrichment of lithium-7 to negate parasitic absorption from lithium-6, limiting its use [14]. Overall, sodium is deemed the more acceptable choice for this microreactor design.

Uranium nitride fuel has a higher density (and therefore uranium content loading) and better thermal conductivity compared to traditional UO_2 fuels used in LWRs. Uranium nitride pellets can be manufactured as high as 90-95% of the theoretical density by sintering at 1900-2000 °C [20]. Uranium nitride has excellent thermal conductivity at about 25 W /mK at 1200 K [21] compared to only about 3.37 for UO_2 at the same temperature [22]. The disadvantage of nitride fuels is naturally occurring nitrogen-14 (the most abundance isotope by far) has a large absorption cross section, necessitating enriching the nitrogen-15 content to 99.5-99.9% to negate a parasitic loss in reactivity [23] [24]. There does not yet exist any commercial or manufacturing-scale production capability for enriched nitrogen-15, however advancements by Ding et al. in ion-exchange chromatography indicate that economic large-scale nitrogen-15 enrichment may be feasible [25].

Since nuclear microreactors are plagued by neutron leakage, it is important to use neutron moderators to increase the probability of fission. Materials high in hydrogen make excellent moderators due to the kinematics of neutron scattering with hydrogen. Metal hydrides are well suited to microreactors due to their high hydrogen content and acceptable mechanical properties [26]. However, at high temperatures, the hydrogen in metal hydrides has a propensity to migrate throughout the crystal lattice and cross material boundaries [16] [27]. This can lead to lower hydrogen content at high temperature operation, hydrogen embrittlement, and hydrogen loss. It may be possible to encase the metal hydride in a silicon-carbide based clad to prevent hydrogen from escaping out of the hydride material [28]. If a plenum is extended over a moderator channel,

it could act as a passive safety feature where hydrogen diffuses out of the metal hydride moderator at high temperatures, collects in the plenum, and lowers the reactivity of the core.

Two metal hydride materials were initially evaluated for this study: zirconium hydride and yttrium hydride. Naturally occurring yttrium (monotonic yttrium-89) has a thermal absorption cross section nearly 2 orders of magnitude greater than zirconium [29]. However, yttrium hydride exhibits better hydrogen retention properties at higher temperatures compared to zirconium hydride. Zirconium hydride retains similar hydrogen density as water up to about 600 °C but would quickly lose much of its hydrogen by 850 °C [29]. Yttrium hydride tends to retain hydrogen well up to temperatures around 1350 – 1375 °C [27] [29] . Compared to zirconium hydride, yttrium hydride in equilibrium with 1 atm H_2 retains 1.6 and 2.6 times as much hydrogen at 900 °C and 1100 °C respectively [30]. Since this microreactor concept will operate at high temperature, yttrium hydride is the better suited metal hydride moderator.

For simulations of thermal reactor systems, thermal neutron scattering cross sections are important. In 2018, the National Nuclear Data Center (NNDC) at Brookhaven National Lab released the next set of Evaluated Nuclear Data Files (ENDF), ENDF/B-VIII.0 [31]. These also include new evaluations for several important materials in our microreactor concept: graphite at various porosity, uranium nitride, zirconium and yttrium hydrides, and silicon carbide. However, the cross section data files available for Serpent do not include these latest evaluations [32]. To include and validate the latest data for use in Serpent, the B-VIII.0 set was downloaded for MCNP as well as Serpent and a series of cross-validation tests performed (see S(α,β) Testing (ENDF/B-VIII.0 update)).

Gadolinium is an important isotope for excess reactivity control in LWRs. Gadolinium has a high neutron absorption cross section and can effectively flatten the reactivity curve through the

entire fuel cycle. When mixed with fuel at sufficiently high density, gadolinium self-shields and depletes slowly, allowing for long-term reactivity control over the entire fuel cycle. However, the most highly absorbing isotopes of gadolinium (Gd-155 and Gd-157) absorb a neutron and transmute to gadolinium isotopes with a much lower absorption cross section [33]. These low-absorbing gadolinium isotopes impose a penalty on the reactivity by the end of cycle. Several recent studies indicate that gadolinium may be loaded in nitride-based fuels in the form of GdN to use as a burnable poison [34, 35]. Gadolinium mixed in nuclear fuels lowers the thermal conductivity of the fuel rod, which is doubly disadvantageous since gadolinium-loaded rods are typically located at neutron flux hotspots where power generation peaks. However, UN has good thermal conductivity naturally and the reduced conductivity may not be as problematic for this microreactor concept [35] [36].

While gadolinium mixed with fuel is a good way to control long-term excess reactivity through the fuel cycle, it cannot be used to suppress beginning of cycle (BOC) excess reactivity (when excess reactivity is highest) without inducing an unacceptable penalty on cycle length. In light water reactors, zirconium diboride is used as an integral fuel burnable absorber (IFBA), essentially a thin coating of ZrB_2 on the outside of fuel rods. Since the coating is very thin, the boron-10 content will burn out completely by the end of cycle (EOC) and not incur a penalty on the cycle length [18] [37] [37] [38]. IFBA provides the majority of the BOC excess reactivity suppression while gadolinium-loaded fuel flattens the long-term reactivity curve. However, there is a question of chemical compatibility and thermal conductivity problems with a ZrB_2 based burnable absorber. Several efforts suggest that boron-nitride (BN) IFBA-like concept may be manufactured and coated on nuclear fuels to control excess reactivity. Eisenstatt and Radford show that BN can be applied as a coating on a nuclear fuel pellet [39]. Several studies have also investigated BN

coatings on UO_2 and UO_2-Gd_2O_3 (gadolinia) mixed fuels, with some samples produced by chemical vapor deposition and burnup characteristics studied [40] [41] [42] [43]. Boron nitride exists in two forms: hexagonal and cubic. The hexagonal form (hBN) is similar to graphite which may ease integrating into a graphite monoblock [44]. The chemical compatibility of a nitride-based IFBA-like coating on a nitride fuel may be easier to overcome and manufacture, justifying its selection.

Like its predecessors in space reactors, microreactors can utilize control surfaces to fine-tune the regulation of excess reactivity [8]. A control drum is a cylindrical surface with a strong neutron absorbing material coating part of its surface. The drum can be turned (via actuators or spring loaded) to allow more or less of the absorbing surface to face the core, reducing the neutron reflection back to the core, reducing the reactivity. Control shutters/sliders is a similar concept, but compared to drums, a slider would be a flat face along the periphery of the core instead of a curved surface. This geometry factor means a control slider has a greater reactivity worth compared to a similar control drum surface. However, there may be problems regarding bending/warping or buckling of the flat sheet compared to control drums. Furthermore, there is a reactivity penalty inherent to sliders due to the empty channel carved into the radial reflector region of the core.

A radial control surface configuration (as in drums/sliders) was chosen over control rods that would drop in axially from the top of the core. This is because the upper axial region is already extended to facilitate the heat pipes to exchange heat with a power conversion system; it would be difficult to find enough space to also accommodate a system of control rods in the same region, along with the mechanical devices to allow their use. Furthermore, control rod channels inside the core itself displaces fuel, lowering the total fuel content that can be loaded into the core and reduces the cycle length/DBU.

Emergency shutdown and SCRAM would be regulated by a central emergency control rod dropping down into the center cavity of the core. This insertion must have large enough reactivity worth to fully suppress the maximum excess reactivity of the core during its fuel cycle.

2 Analysis and Results

2.1 Reactor Design Choices

2.1.1 Monoblock and Reflector

Candidates for the monoblock and reflector materials considered were SA316L stainless steel, beryllium metal, beryllium oxide, zircaloy-4, and graphite. The effect on cycle length and reactivity of various reflectors is considered with a nominal case reactor consisting of a lattice with 2:1 ratio of equally sized YH_2 moderator and UN fuel rods surrounded by an effectively infinite reflector (100 cm thick reflector). The monoblock and reflector comparisons use the same material for both monoblock and reflector to avoid differences in thermal expansion, irradiation induced swelling, etc. from using two different materials. Aside from neutronic considerations, some candidate materials are infeasible due to structural and thermal concerns. Figure 2-1 shows the cycle of a nominal microreactor for various monoblock and reflector materials.

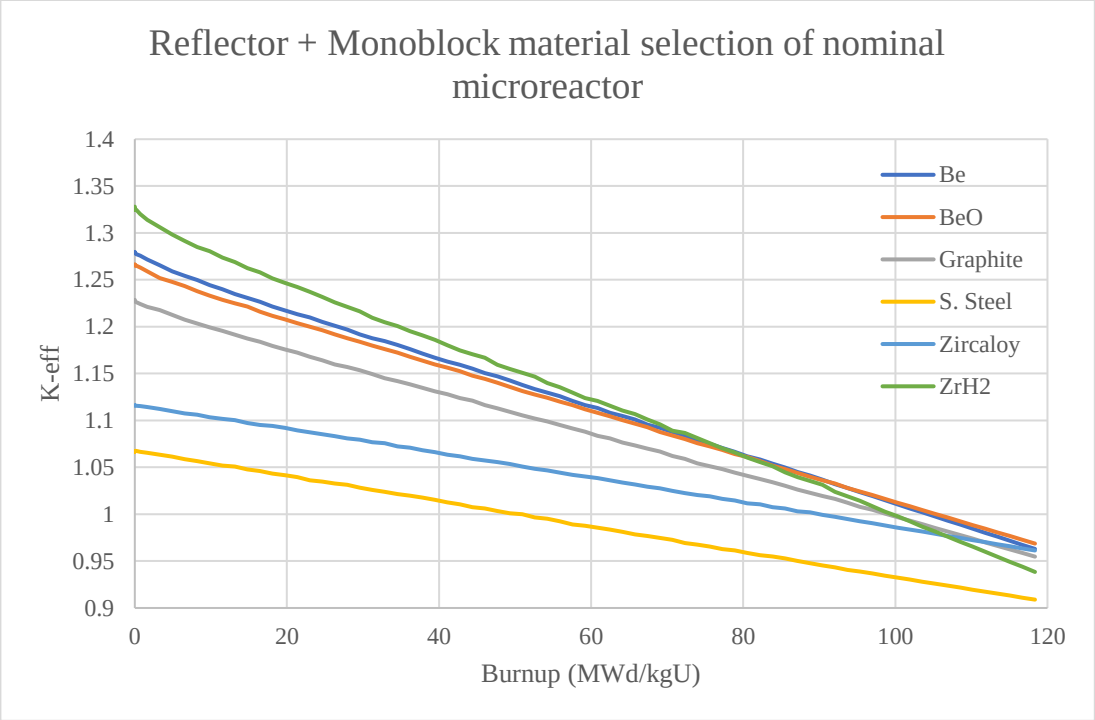

Figure 2-1. Cycle of the nominal microreactor with different monoblock + reflector materials. Simulation parameters: 10^4 particles per generation, 60 skipped cycles, 200 active cycles. Resulting uncertainties all within 30 – 48 pcm.

Stainless steel is structurally strong and has a high melting temperature, but incurs a significant reactivity penalty due to neutron absorbing isotopes of iron, chromium, and nickel. Beryllium has been considered as a moderator for nuclear reactors since the 1950's and for space reactor applications [45]. However for a commercial microreactor design, beryllium metal's high cost [46] and toxicity is undesirable. Beryllium metal also tends to form interstitials and undergo bubbling under neutron irradiation at temperatures around and above 400 °C [45]. Since the operating temperature of sodium heat pipes is between 600 °C to 1200 °C [47], the monoblock must necessarily be at a higher temperature to facilitate heat transfer, rendering beryllium infeasible. Beryllium oxide has nearly the same number density of beryllium atoms as beryllium metal, but suffers from a "severe reduction in the strength and thermal conductivity of BeO" for neutron fluences of 2×10^{20} n/cm^2 [45] which would be problematic for a reactor designed for ~10 year

lifetime with limited to no servicing. Metal hydrides (zirconium and yttrium hydrides) offer great moderation potential but are brittle and weak, rendering them unsuitable as a structural monoblock material [48]. Instead, metal hydride moderators are incorporated as cladded rods inserted into penetrations in the monoblock alongside fuel rods. Zircaloy is widely used in the nuclear industry thanks to excellent thermophysical properties, structural strength, and transparency to neutrons [49]. Graphite is also widely used in nuclear reactors, serving as structural support and a neutron moderator [50]. While the reactor is too small to be fully moderated with graphite alone, a graphite monoblock and reflector does contribute modestly to neutron moderation and so is the choice material after zircaloy.

2.1.2 Reflector Thickness Tradeoffs

Since microreactors are plagued by high neutron leakage, neutron reflectors can be a cost effective approach to improving the neutron economy and fuel utilization. The effect of reflector thickness was studied with a graphite reflector and monolith. Both radial and axial reflectors' thickness are increased equally in 15 cm increments.

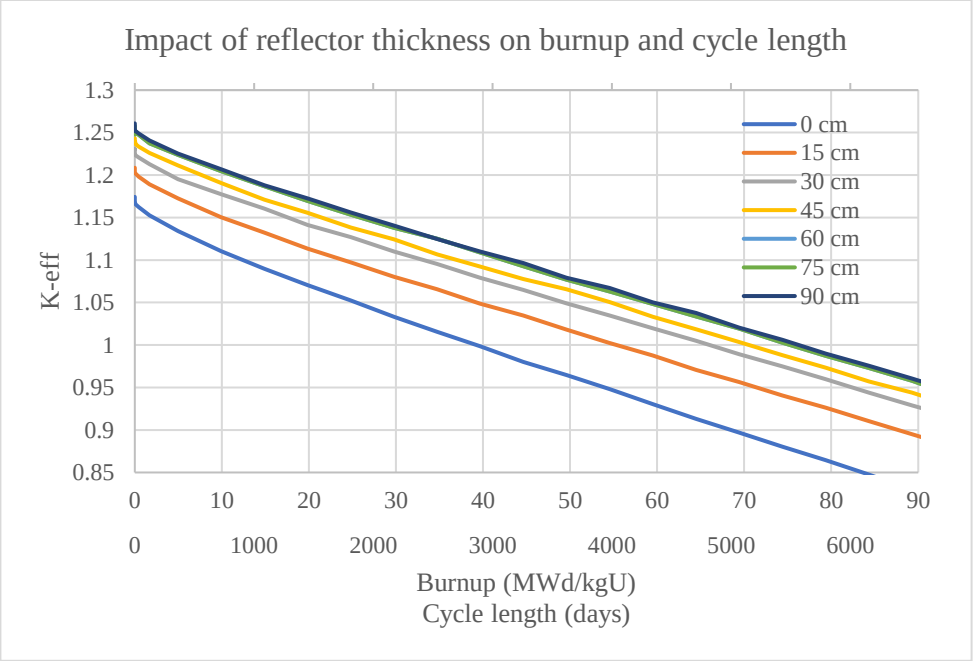

Figure 2-2. Graphite reflector thickness effect on cycle.

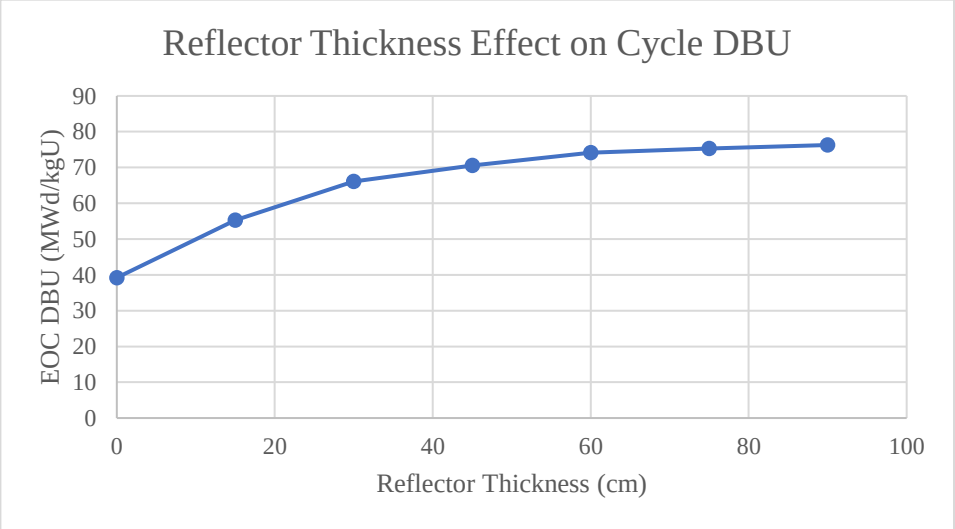

Figure 2-3. Graphite reflector thickness effect on cycle.

The effectiveness of the reflector saturates around 60 cm. Since reflector volume scales by the cube term of the thickness, there are diminishing returns to adding more and more reflector bulk. The cost-benefit analysis of the reflector is discussed later in the Economic Estimates section.

2.1.3 Lattice Pitch Expansion

The microreactor initial design had a lattice pitch of 1.675 cm with 1.575 cm outer diameter heat pipes. When heat pipe operating limits were calculated with these initial heat pipe dimensions, it was found the maximum power each heat pipe could remove was less than 6 kW. For a reactor with 1224 heat pipes and thermal power output of 15 MWth, each heat pipe would need to remove on average about 12.25 kW. Since heat removal capability of heat pipes scales with the cross sectional area of the pipe, it was determined that the lattice pitch must expand to accommodate larger heat pipes to remove sufficient heat from the reactor. It was found a 1.800 cm inner diameter heat pipe could be used to satisfy heat removal requirements with some margin. Using the same heat pipe wall thickness brought the heat pipe outer diameter to 1.920 cm. To accommodate the larger heat pipes, the lattice pitch is expanded from 1.675 cm to 2.020 cm, with some spacing reserved for structural graphite.

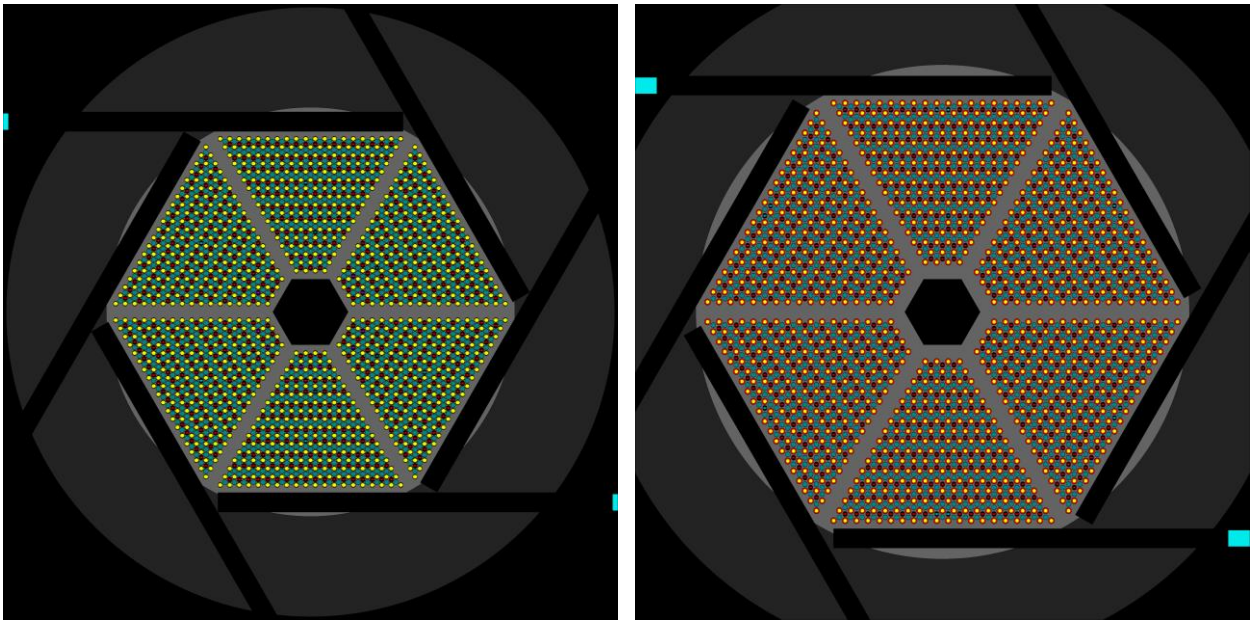

Figure 2-4. Comparison of initial (left) and expanded (right) lattice for the full core geometry.

Keeping the thickness of the radial reflector constant at 30 cm, this lattice expansion increases the microreactor outer radius from 92 cm to 105 cm. While 13 cm increase is significant, it would still meet the design requirement of fitting within the bed of a typical flatbed truck. A closeup look at the expanded lattice reveals that the spacing between elements is considerably larger compared to the initial lattice. In Figure 2-5, the moderator (blue) and fuel (solid red with rings) remain the same size (outer radius 0.7125 cm) while the heat pipes (red + yellow) have expanded in the larger lattice. Each heat pipe is also not adjacent to another heat pipe; heat pipes are only adjacent to fuel or moderator elements. This suggests it would be possible to tighten the lattice slightly by allowing heat pipes to "spillover" into adjacent lattice elements containing only moderator or fuel. This would present a significant difficulty in modelling the reactor however, as it implies a pin universe for heat pipes that is larger than the lattice pitch of the hexagonal lattice. To ensure the entire heat pipe geometry is captured, fuel and moderator pin universes would need to include the "spillover" of nearby heat pipes into their own universe definition. One would also need to ensure the remaining spacing is still sufficient for heat transport and structural purposes. In this thesis, this is not done and the expanded lattice is simply used as-is with a larger spacing between each element.

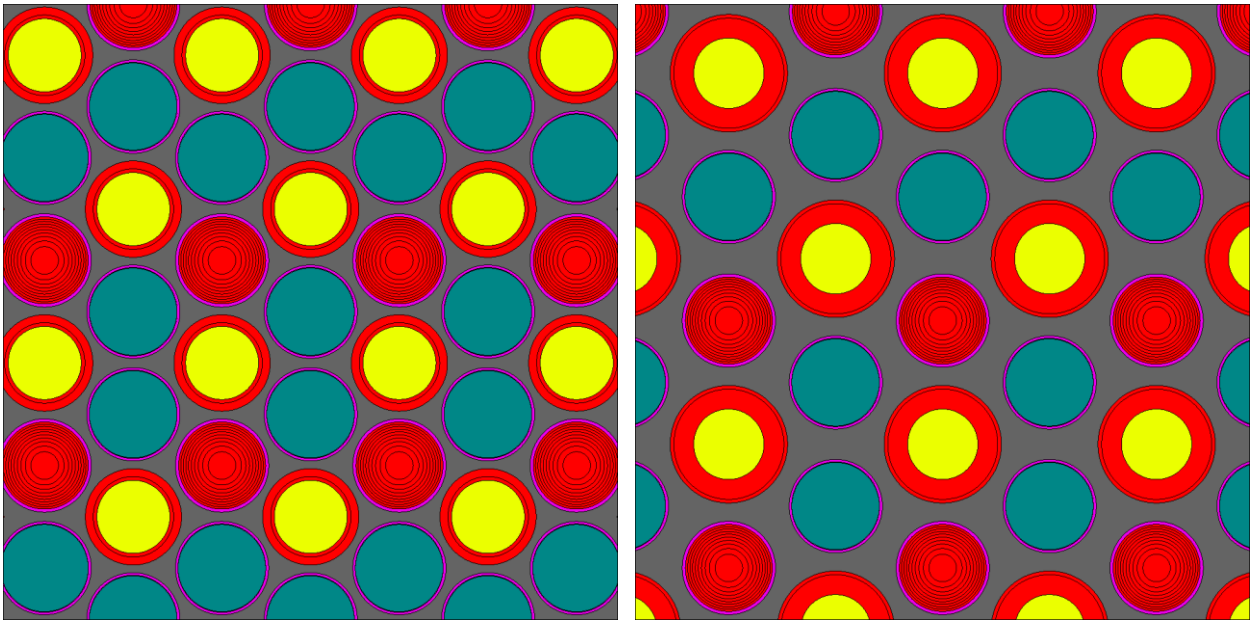

Figure 2-5. Comparison of initial (left) and expanded (right) lattice, closeup view of lattice. Plot windows are identical, highlighting the larger spacing between elements in the expanded lattice arrangement. Fuel rods (red), moderator rods (blue), heat pipes (red + yellow).

Some studies presented in this thesis were re-done with the expanded lattice if it was decided the lattice expansion would significantly alter the results. The reflector thickness study is one such case and results are presented for the expanded lattice. Other studies, such as the selection of monoblock and reflector material, were not redone if the lattice expansion would not significant affect the results or conclusions drawn.

2.1.4 Fuel to Moderator Ratio

The microreactor uses yttrium hydride moderator rods as YH_2 and assumes a hydrogen retention coating based on the Advanced Moderation Module (AMM) work done at Argonne National Lab would be sufficient to retain a stoichiometry of 2 hydrogen atoms per yttrium atom [28]. Initially, the radius of the YH_2 moderator rods is set to the same radius as the UN fuel rods

with 2 moderator rods for each fuel rod. See sections on Lattice Pitch Expansion and Thermal Performance for details on heat pipe studies.

The expanded lattice not only would accommodate larger heat pipes but also could accommodate larger YH_2 moderator rods. The YH_2 rods are expanded from the initial radius of 0.7125 cm up to 0.9375 cm, the largest size that fits within the expanded lattice including an AMM coating, in 0.375 cm increments. The AMM coating is taken as a 0.1 mm niobium substrate and 0.4 mm SiC hydrogen barrier [28]. The ratio of moderator rods to fuel rods remained the same, 2:1, as did the radius of fuel rods to preserve the fuel inventory for each case. Thus, by expanding the YH_2 rods, a comparison of moderator-to-fuel mass ratio effect on the cycle length is performed. For UN density of 14.016 g/cm^3 at 19.75% enrichment, the uranium density is 13.183 g-U/cm^3. Then, the ratio of moderator mass to fuel mass for this study is:

$$\varepsilon = \frac{(2)\left(4.3\frac{g \cdot YH_2}{cm^3}\right)}{(1)\left(13.183\frac{g \cdot U}{cm^3}\right)} * \frac{R_M^2}{R_F^2}$$

where R_M and R_F is the radius of the YH_2 moderating rod and UN fuel rod respectively. summarizes the ratio of moderator mass to uranium mass studied.

Table 2-1. Moderator to fuel mass ratio of each moderator rod size.

UN fuel rod radius: 0.7125 cm (fixed)	
YH_2 moderator rod radius (cm)	Ratio of YH_2 mass to U mass (ε)
0.7125	0.65235
0.7500	0.69086
0.7875	0.79692
0.8250	0.87463
0.8625	0.95594
0.9000	1.10409
0.9375	1.22159

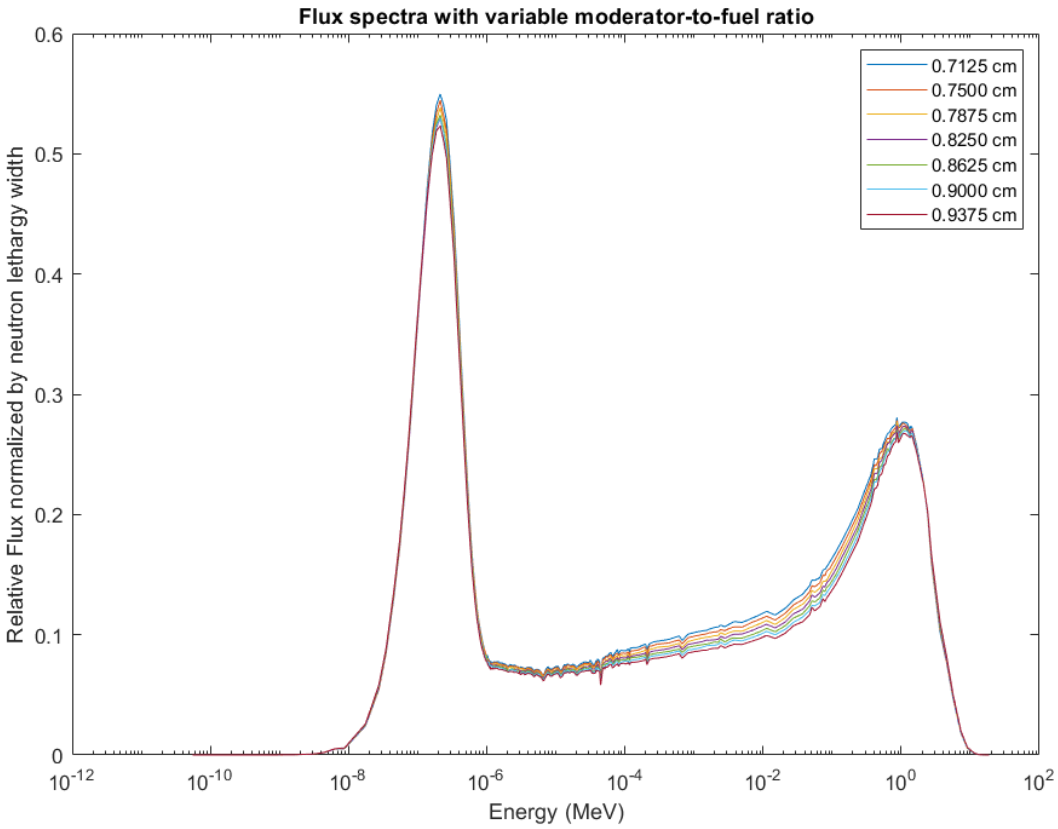

Figure 2-6. Normalized flux spectra wrt. moderator rod size.

Neutron flux is normalized to the width of the neutron lethargy bin for each energy tallied at the beginning of cycle. The neutron flux spectrum changes relatively slowly as the moderator to fuel mass ratio increases. The thermal peak in the flux spectrum decreases slightly as the radius of the moderator rods increases, evidenced by a lower thermal utilization factor, which decreases as the moderator-to-fuel ratio increases (number of H atoms to U atoms).

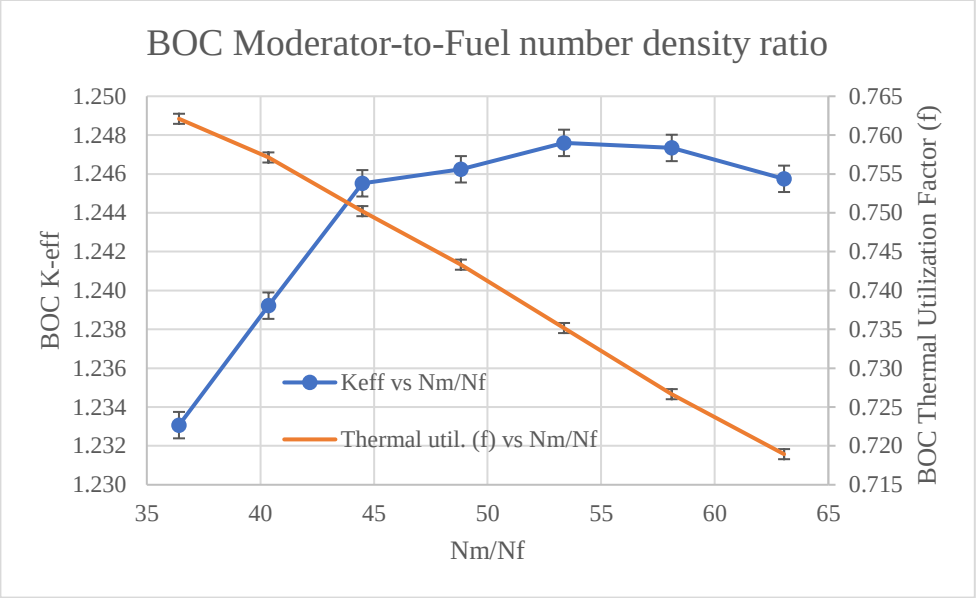

Figure 2-7. Thermal utilization and multiplication factor wrt. moderator-to-fuel mass ratio.

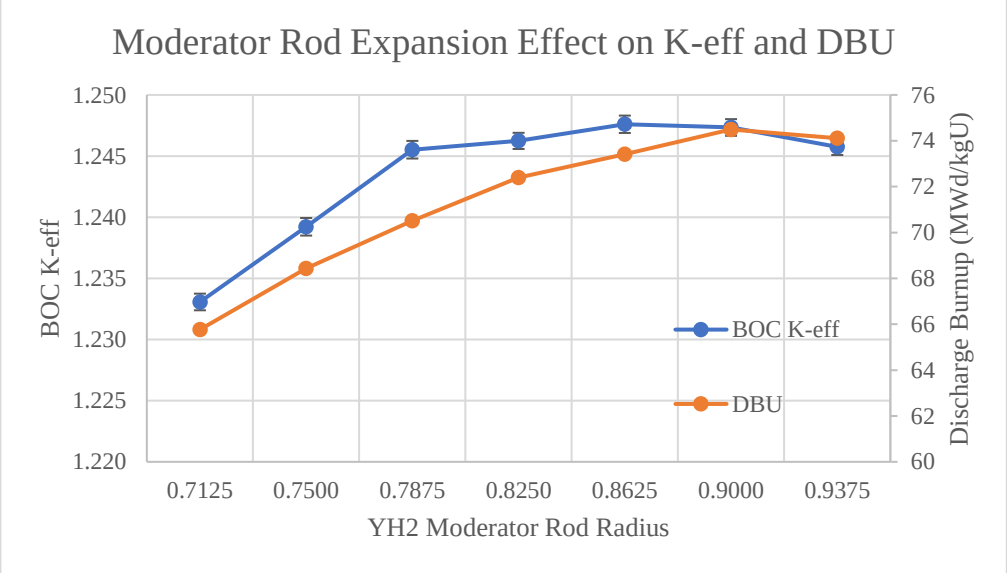

Figure 2-8. Multiplication factor and DBU with moderator rod size.

Several important conclusions are drawn from these charts. First, the beginning of cycle K-eff is quite sensitive to increasing the moderator rods size, increasing by about 1400 pcm from the nominal 0.7125 cm radius moderator rods to 0.8250 cm radius rods. Second, the reactor with nominal 0.7125 cm radius moderator rods is undermoderated. This is an important safety feature.

As the reactor power increases and heats up, hydrogen tends to migrate out of metal hydride moderators [16] [26] [27]. The loss of hydrogen decreases the number ratio of moderator to fuel atoms, which in turn decreases K-eff. Hence an undermoderated reactor has inherent negative reactivity feedback due to hydrogen migration when power is increased. Miao et al. have suggested the use of a hydrogen retention plenum for self-regulation of microreactors during power excursions [28], but it is not clear what mechanism would allow hydrogen to diffuse back into the metal hydride. If the moderator rod radius were 0.8625 cm (N_m/N_f of about 53, the highest BOC K-eff) or greater, the reactor would be overmoderated. Any conditions leading to an increase in the moderator temperature and hydrogen migration would also increase the multiplication factor – or positive reactivity feedback!

That said, increasing the moderator rod size does have benefits in increasing the discharge burnup and lengthening the fuel cycle. The moderator rods could be expanded to no more than about 0.8625 cm radius to avoid overmoderation, which would increase the discharge burnup from 65.7 MWd/kgU to 73.4 MWd/kgU and cycle length about 10%. However, for the remainder of this thesis, the moderator rods are kept at a radius of 0.7125 cm as to keep the reactor well undermoderated.

2.2 Reactivity Control

Excess reactivity is required for an extended fuel cycle with no refuelling for a microreactor operating in a remote location. In this reactor, the majority excess reactivity is controlled with burnable absorbers. Fine-tuned reactivity control is possible with adjustable control sliders external to the core.

2.2.1 Burnable Absorber

The burnable absorber design is inspired by the fuel design of the IRIS (International Reactor Innovative and Secure) by Franceschini and Petrovic, which mixed an integral fuel burnable absorber (IFBA) and erbia [18] [37]. For this reactor, an IFBA-like coating of boron nitride (BN) and gadolinium nitride (GdN) mixed in fuel is proposed. Gündüz et al. have shown it is possible to coat nuclear fuels with BN [40] [41] [42]. Uslu et al. have produced BN coated urania fuel and studied their neutronic performance [51]. Recent efforts at Oak Ridge National Laboratory show that the production of UN kernels with gadolinium burnable absorber is possible [34]. UN and GdN composite pellets with up to 38.4% weight GdN have been produced by spark plasma sintering [35]. The addition of gadolinium has long been known to reduce the thermal conductivity of fuel. Ahn and Kim have measured the thermal conductivity of UN-GdN composite fuel pellets and found the thermal conductivity still remains relatively high [35].

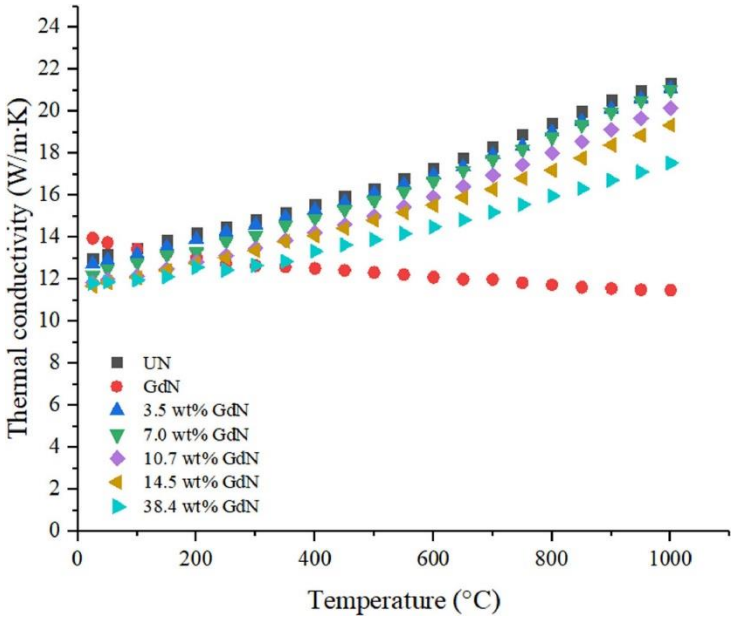

Figure 2-9. Thermal conductivity measured in UN-GdN composite fuel for pellets sintered at 1800 °C [35].

The neutron capture reaction with boron-10, $^{10}B(n,\alpha)^{7}Li$, produces helium. Accumulation of helium as burnup increases internal pressure on the cladding, eventually leading to creep and separation of the fuel from cladding and rising fuel temperatures [52]. To avoid this, the thickness of the BN coating is kept very thin at 0.1 mm on all fuel rods. This is equivalent to a boron loading of 3.578 mg boron per cm of fuel pin height. The boron-10 concentration is varied between natural boron (20% ^{10}B) to 100% enriched while the coating thickness remains fixed. GdN is treated as natural gadolinium with enriched nitrogen (99.99% enriched ^{15}N, same as fuel).

To determine a feasible combination of BN coating and GdN mixing, a scoping study was performed with an infinite 2D lattice with various combinations. The infinite 2D lattice features 18 fuel pins and a 2:1 fuel-to-moderator rod ratio. BN coating is applied to all fuel rods. GdN is applied to fuel rods in a 1/18, 2/18, 3/18, and 4/18 ratio at weight percentages of 2%, 6%, 10%, 16%, and 20%.

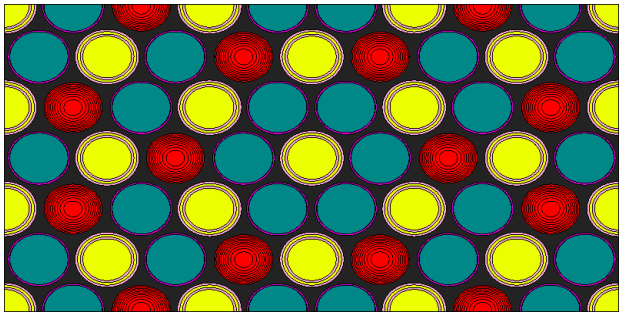

Figure 2-10. Infinite 2D lattice arrangement.

The baseline case is with no burnable absorbers. The baseline case found a BOC K-eff of 1.37016 ± 0.00014 and discharge burnup of about 106.8 MWd/kgU. and summarize the results for natural and 100% enriched BN with various GdN loadings.

Table 2-2. Infinite 2D lattice case with natural BN coating.

GdN loaded fuel with natural boron BN coating					
DBU of GdN-loaded cases (MWd/kgU)					
# rods w/GdN	2% GdN	6% GdN	10% GdN	16% GdN	20% GdN
1/18	105.5	104.1	101.7	100.0	98.38
2/18	99.83	98.23	96.83	91.73	90.29
3/18	87.63	85.19	83.53	75.25	73.74
4/18	72.18	68.82	66.91	56.18	54.53
DBU Penalty compared to base case (MWd/kgU)					
1/18	1.27	2.71	5.17	6.81	8.45
2/18	6.69	8.59	9.99	15.1	16.5
3/18	19.2	21.6	23.3	31.6	33.1
4/18	34.6	38.0	39.9	50.6	52.3
DBU Penalty in % of base case					
1/18	1.19%	2.54%	4.84%	6.37%	7.91%
2/18	6.54%	8.04%	9.35%	14.1%	15.5%
3/18	18.0%	20.3%	21.8%	29.6%	31.0%
4/18	32.4%	35.6%	47.4%	47.4%	48.9%

Table 2-3. Infinite 2D lattice case with 100% enriched BN coating

GdN loaded fuel with 100% boron-10 BN coating					
DBU of GdN-loaded cases (MWd/kgU)					
# rods w/GdN	2% GdN	6% GdN	10% GdN	16% GdN	20% GdN
1/18	102.8	100.6	98.09	96.89	94.84
2/18	96.09	94.30	92.81	87.14	85.02
3/18	82.72	80.49	N/A	N/A	N/A
4/18	64.45	N/A	N/A	N/A	N/A
DBU Penalty compared to base case (MWd/kgU)					
1/18	4.15	6.28	8.81	10.0	12.1
2/18	10.8	12.6	14.1	19.8	21.9
3/18	24.2	26.4	N/A	N/A	N/A
4/18	42.5	N/A	N/A	N/A	N/A
DBU Penalty in percentage of base case					
1/18	3.88%	5.88%	8.24%	9.37%	11.3%
2/18	10.1%	11.8%	13.2%	18.5%	20.5%
3/18	22.6%	24.7%	N/A	N/A	N/A
4/18	39.7%	N/A	N/A	N/A	N/A

Entries denoted in green, yellow, and red indicate a combination with less than 5% penalty, less than 10% penalty, and greater than 10% penalty to discharge burnup compared to the baseline case. Entries denoted in grey indicate cases that fail to reach criticality at BOC. Based on these findings, the enriched BN coating with 2-10% GdN on 1/18 fuel rods seemed the most promising.

Moving to a 3D model, it was decided to focus on enriched BN coating with GdN loadings of 2%, 3%, 4%, 6%, and 8% by weight in 11% of fuel rods. These studies were carried out on the unexpanded lattice and molybdenum wick (noting that this core configuration is unoptimized for thermal management of heat pipes, see the Section on Lattice Pitch Expansion for details. Again, the baseline case is treated as the 3D core without any burnable absorbers, which found a BOC K-eff of 1.24033 ± 0.00012 and discharge burnup of 71.01 MWd/kgU. The results of the full core study are summarized in Verification with the Expanded Lattice.

Table 2-4. Burnable absorber loading for the full core (unexpanded lattice).

3D full core, enriched BN coating, variable GdN loading				
Baseline case DBU: 71.01 MWd/kgU				
% wt. GdN loading	DBU (MWd/kgU)	DBU penalty	Percent penalty	Peak K-eff
2%	68.77	2.241	3.16%	1.07477
3%	67.73	3.286	4.63%	1.06500
4%	65.76	5.260	7.41%	1.05797
6%	59.45	11.56	16.3%	1.04727
8%	54.62	16.40	23.1%	1.04069

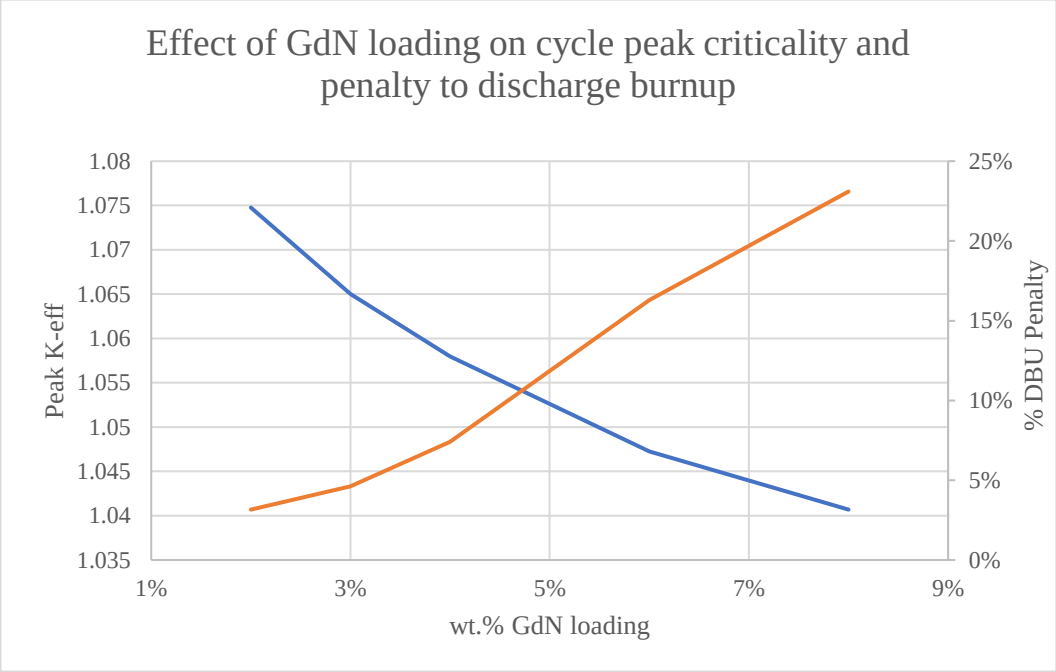

Figure 2-11. Effect of BA loading on cycle peak criticality and discharge burnup penalty.

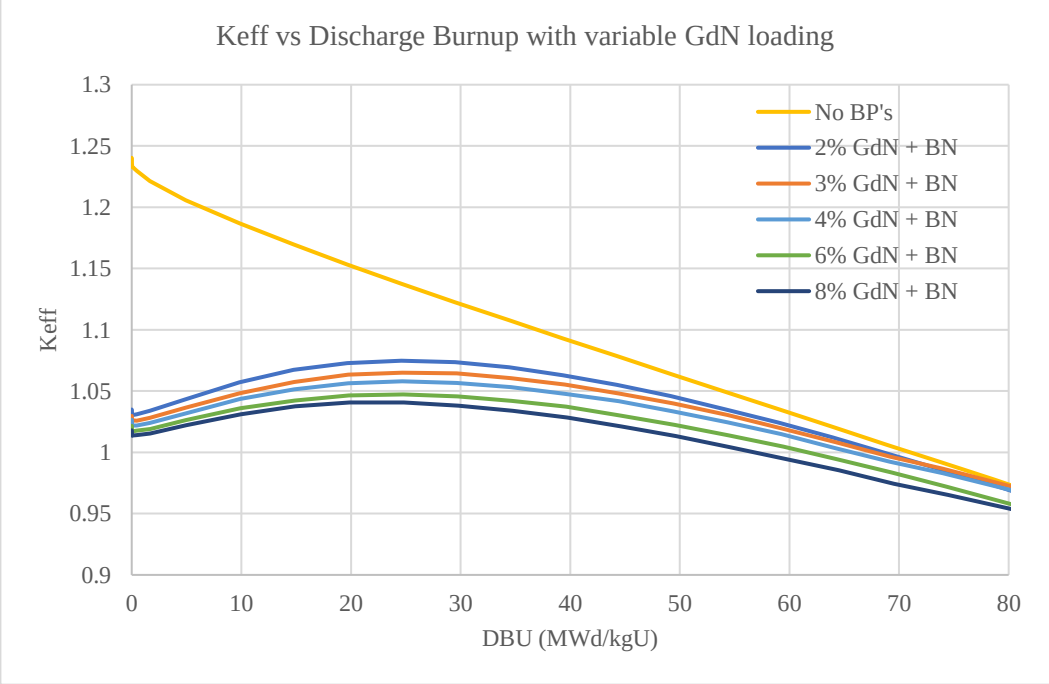

Figure 2-12. DBU of cycle with burnable absorbers loaded for the full core (unexpanded lattice). Uncertainties range from 12 - 30 pcm.

2.2.2 Adjustable Control Sliders

The selected burnable absorber loading combination depends on the reactivity worth provided by the external control sliders. The total reactivity worth of the sliders is simply the change in reactivity when fully withdrawn versus fully inserted. Reactivity is computed in the customary way as $\rho = \frac{k_{eff}-1}{k_{eff}}$.

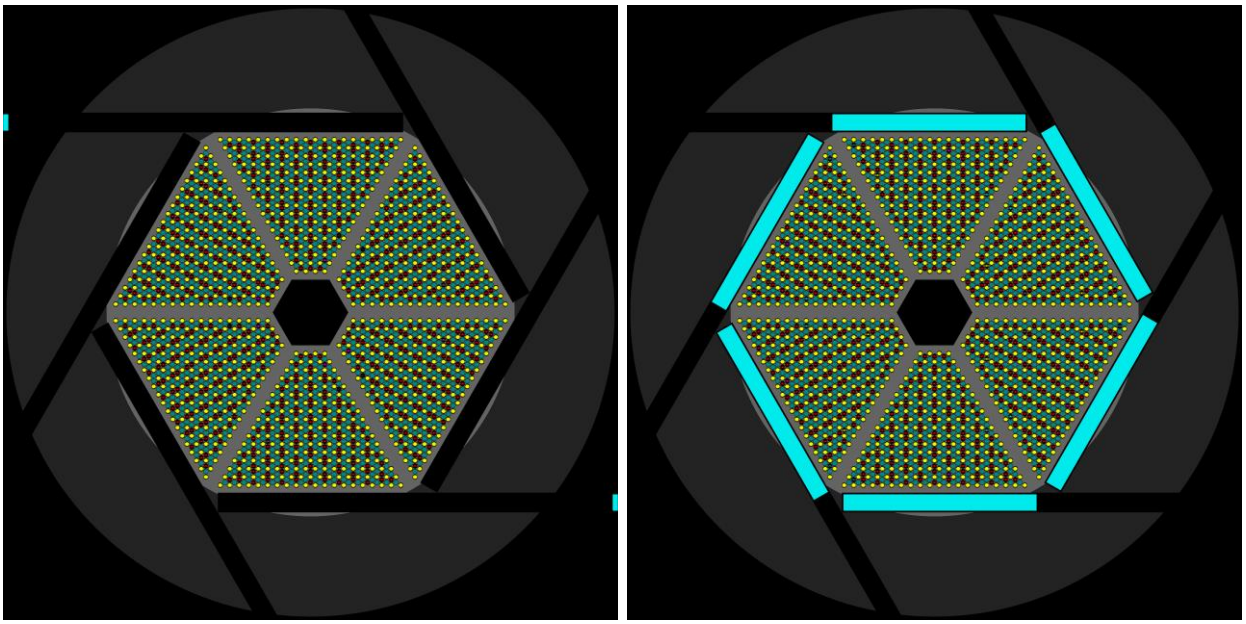

Figure 2-13. Full core configuration with control sliders fully withdrawn (left) and fully inserted (right) (unexpanded lattice configuration). Notice the deep grooves carved into the reflector to accommodate the movement of the control sliders.

The baseline case with no burnable absorbers at BOC (as to not distort the reactivity of the core with absorbers or fission products) is used to compute the reactivity worth of the slider insertion. In the unexpanded/tight lattice core, the control sliders have a net reactivity worth of about 0.04673, or equivalently a K-eff of 1.24036 ± 0.00022 fully withdrawn to 1.17241 ± 0.00020 fully inserted – a net change in the multiplication factor of 0.06795 ± 0.000297.

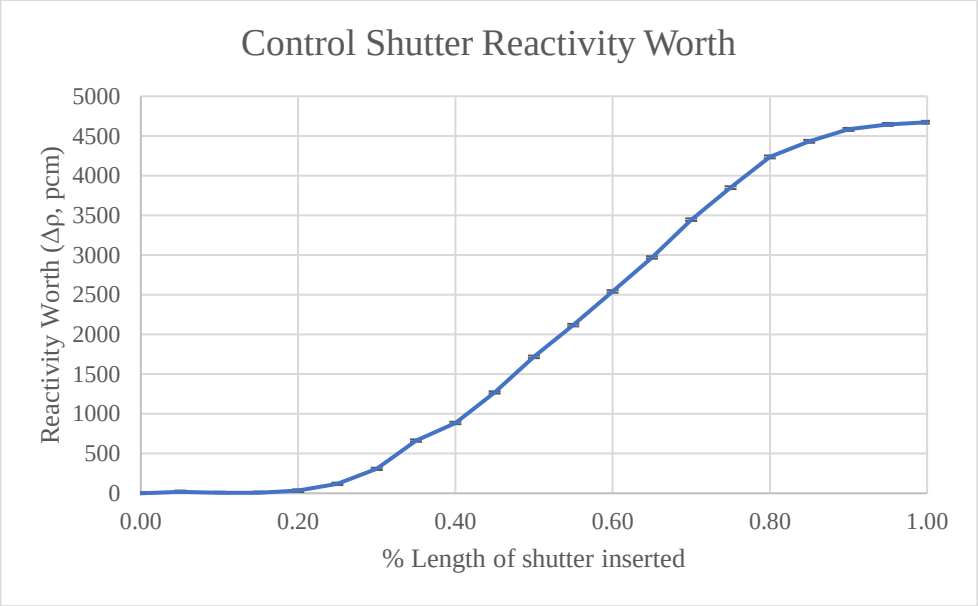

Figure 2-14. Integral reactivity worth of control sliders wrt. % length insertion (unexpanded lattice).

Based on this, the selected burnable absorber loading is 4% GdN by weight with natural BN coating on all fuel rods. The peak multiplication factor for this configuration is 1.05797 ± 0.00025, which occurs at a burnup of 24.7 MWd/kgU. The control sliders would be able to compensate the excess reactivity of this configuration at its peak with about a 998 pcm margin on the shift in K-eff. It is also noted that the 3% GdN loading case may also be feasible, with a peak multiplication factor of 1.06500 ± 0.00027. However, the margin on the change in K-eff in this case is only 295 pcm; given the uncertainty of 25 pcm on ΔK-eff, this may not be enough to satisfy safety concerns given that there are numerous other uncertainties (ex: temperature, cross section libraries) that may push the margin on K-eff too close.

To accommodate the movement of the control sliders, deep groove penetrations are carved into the radial reflector, which effectively reduce the reflector thickness. The penalty to discharge burnup associated with the slider grooves is computed by comparing the baseline case with no

burnable absorbers against an otherwise identical case with the grooves filled in with graphite. The filled in grooves result in a discharge burnup of about 79.3 MWd/kgU, a penalty of about 8.3 MWd/kgU to the baseline case. This is a relatively steep penalty to the fuel utilization; some of the lost burnup could potentially be "bought back" by thickening the reflector (see Reflector Thickness Tradeoffs).

2.2.3 Verification with the Expanded Lattice

The performance of burnable absorbers is verified on the expanded lattice configuration with larger heat pipes using nickel wicks (see Lattice Pitch Expansion and Heat Pipe Down-Selection for details on the lattice expansion). The baseline case of the expanded lattice configuration is considered as the core with no burnable absorber loading and a nickel heat pipe wick (see Heat Pipe Down-Selection), which yields a discharge burnup of 68.85 MWd/kgU. However, it was found that the same burnable absorber loading of 4% GdN on 11% of rods and 0.1 mm enriched BN coating would be insufficient for the control sliders to compensate the remaining reactivity swing at the maximum in the cycle. The gadolinium loading was increased to 4.5% wt. and BN density increased to 2.25, effectively increasing the boron content loading from 3.578 mg/cm to 3.833 mg/cm. Consequently, the discharge burnup is reduced to 61.217 MWd/kgU.

Likewise, the control slider reactivity worth is recomputed for the expanded lattice configuration. Given that the core diameter has expanded 26 cm, the control sliders will be slightly less effective as they operate on the periphery of the core. For the new burnable absorbers with increased GdN loading, the peak multiplication factor is 1.051670 ± 0.00014. The control sliders in the expanded lattice found K-eff of 1.19763 ± 0.00016 to 1.14327 ± 0.00017, a change of 0.05436. The control sliders in this configuration are still sufficient to control excess reactivity at

the cycle peak, but with reduced margin of only 269 pcm ± 22 pcm. Again, it must be noted that this margin would be affected by other sources of uncertainty (eg: systematic uncertainties in cross section data) and may not be sufficient margin for safety concerns.

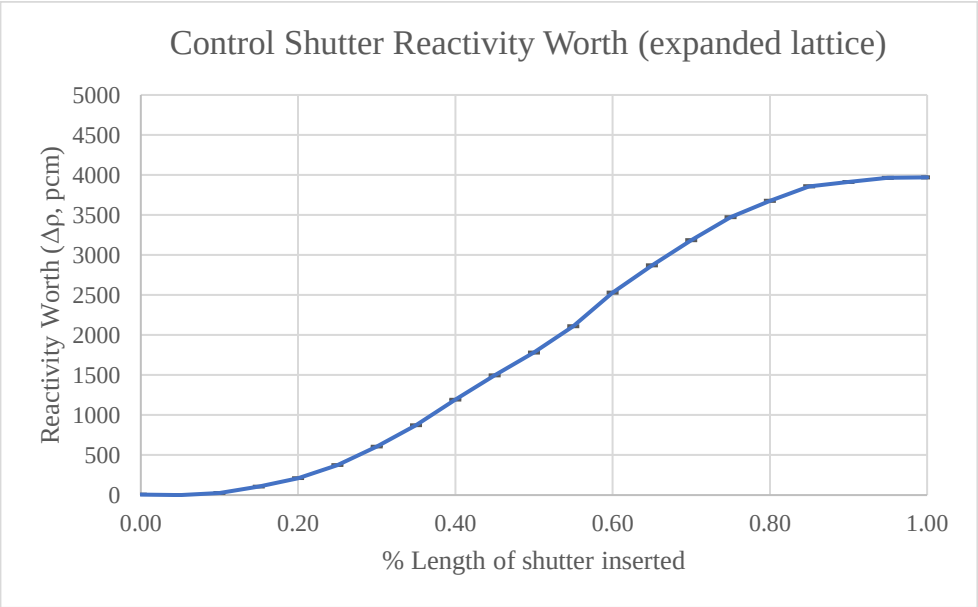

Figure 2-15. Integral reactivity worth of control sliders wrt. % length insertion (expanded lattice).

2.2.4 Shutdown

The central empty channel accommodates the emergency shutdown control rod. The shutdown rod not only must compensate for maximum reactivity when first inserted, it must also deal with the power defect as the reactor cools back to room temperature. Two cases are presented: the reactivity change with respect to temperature of the core both with and without burnable absorbers. The case without burnable absorbers at BOC has a K-eff of 1.24033 ± 0.00012. The case with burnable absorbers at BOC has a K-eff of 1.01856 ± 0.00017. The reactivity worth of the shutdown rod is computed as the change in reactivity when inserted vs BOC K-eff of the baseline. For this

simple approximation, reactor temperature is treated as setting the temperature of all materials in the geometry to the same temperature, including thermal scattering data (see S(α,β) Testing (ENDF/B-VIII.0 update) for comments on temperature interpolation of scattering data).

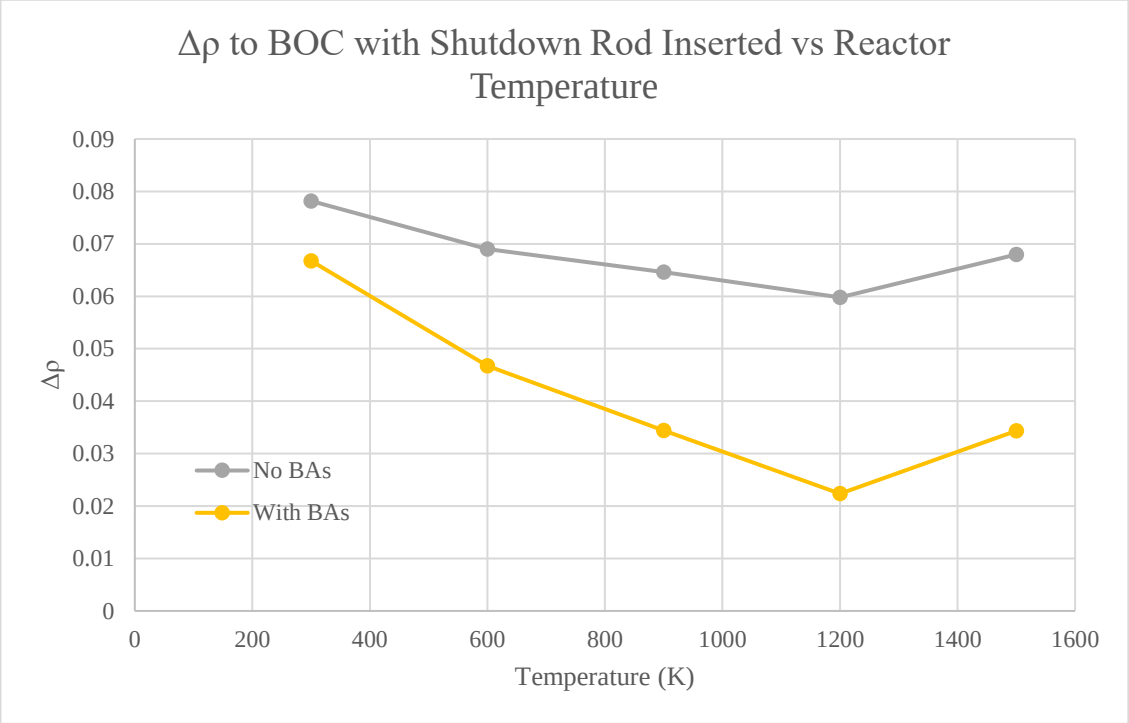

Figure 2-16. Isothermal full core reactivity worth, showing positive reactivity coefficient up to 1200 K.

The maximum reactivity of the expanded lattice cycle is 0.052223 ± 0.00012. For a maximum reactivity of 0.052223, the above results indicates the core may not shut down the poisoned core, with the caveat that the reactivity worth is calculated at the BOC when the shutdown rod has the least impact due to the gadolinium loaded rods at the center of the core are unburnt at BOC. Furthermore, there is the troubling trend in both cases where the reactivity of the core increases from 300 K to 1200 K; or in other words as the reactor warms up from to 1200 K, the core becomes more reactive in the same geometry. One slight positive is that the effect reverses past 1200 K, ie:

for an increase in power resulting in higher temperatures, the reactivity of the core decreases, which will tend to have a stabilizing effect above 1200 K. An increase in power at 1200 K that increases material temperatures has a negative change in reactivity. Additionally, for the BA-loaded case, the reactivity worth of the shutdown rod is lowest at 1200 K at only $\Delta\rho = 0.022359$, close to operating temperature of the reactor. To be clear, this result is for BOC of the BA-loaded core, whose flux is highly depressed at the center of the core where the shutdown rod lies (see Core Power Distribution and Peaking Factors). At the maximum reactivity of the cycle, the flux distribution will have shifted to be more centrally peaked, which should increase the reactivity worth of the shutdown rod. This has also not accounted for any thermal expansion or density change of materials, which is expected to make the reactivity coefficient less positive or potentially negative.

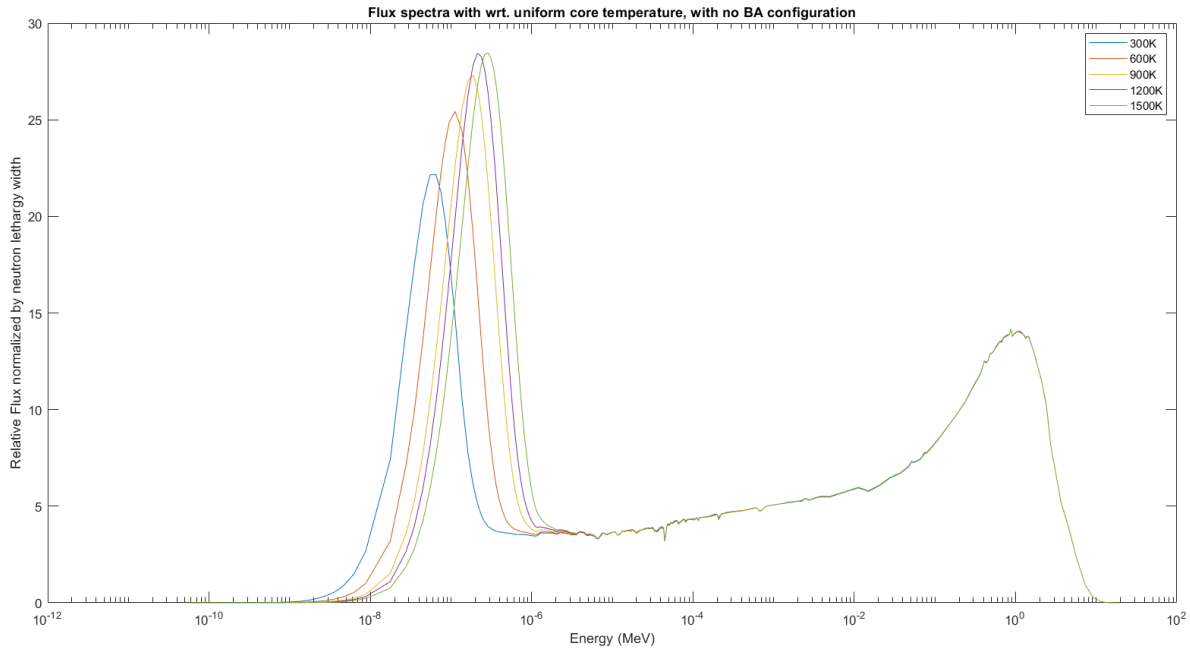

Figure 2-17. Neutron flux spectra shift with temperature of the unpoisoned core.

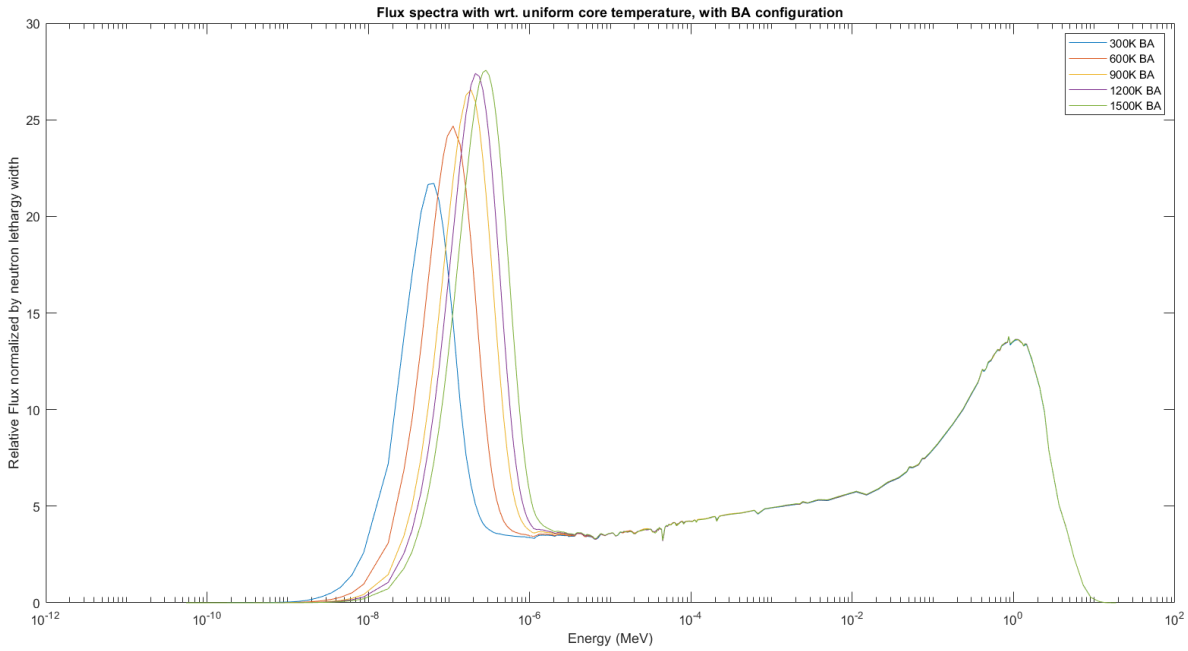

Figure 2-18. Neutron flux spectra shift with temperature of the poisoned core.

It was found the change in reactivity worth of the control rod at different temperatures was caused by a spectral shift of the neutron flux of the core. The neutron spectrum for both cases shows that as temperatures increase, the thermal peak shifts to a harder spectrum and higher peak magnitude. Qualitatively, this spectral shift matches the change in reactivity seen; a slightly harder spectrum would lower K-eff slightly but a higher peak magnitude would increase K-eff. Between 1200 K and 1500 K, the spectral shift plateaus and only shifts the thermal peak to a higher energy while the magnitude of the peak is relatively unchanged, which is apparent in the decrease in K-eff at 1500 K. The spectral shift of the flux is likely attributed to the metal hydride moderator as Trellue et al. note that yttrium hydride is predicted to have a positive reactivity coefficient [53]

[54]. Kimura and Wada studied a SMR concept moderated with calcium hydride and poisoned with gadolinium oxide. They attributed the positive reactivity to the shift in thermal equilibrium energy between neutrons and hydrogen; as temperature increases, the thermal energy of the neutron shifts higher. The thermal absorption cross section of gadolinium in the $1/v$ region decreases as v increases, which increases the availability of neutrons in the core and shifts the thermal peak of the spectrum to a higher energy [55]. In the non-poisoned core, there is no gadolinium absorber and the spectral shift is attributed only to the positive moderator coefficient – evidenced by the steeper slope of the reactivity for the poisoned core compared to the non-poisoned core. In Figure 2-17 and Figure 2-18, which are plots of the neutron flux in only the active core, the neutron spectra for the unpoisoned core cases all exhibit a slightly greater thermal peak compared to the poisoned core.

Likewise, a look at the relative fission rate of both the unpoisoned and poisoned core a clearer example that the fission rate increases in the unpoisoned core case, as seen in Figure 2-19 and Figure 2-20. These are plots of the neutron flux in the active core normalized to the width of the neutron lethargy bin multiplied by the macroscopic fission cross section. It can be clearly seen the relative fission rate is greater in the unpoisoned core, as expected. The peaks also tend to follow the same trend in that they increase up to 1200 K and decrease at 1500 K. However, the peak at 1200 K for both the unpoisoned and poisoned core seems abnormally high; that is the magnitude of the increase from 900 K to 1200 K does not seem to follow the trend. This cannot be attributed to the presence of burnable absorbers (BN coating and UN-GdN composite fuel) as the two cases are otherwise identical yet the anomaly appears in both cases. A more thorough investigation is warranted to determine which material is responsible for the spectral shift and anomaly at 1200 K.

It is also possible there may be an inconsistency in the cross sections or thermal scattering data files.

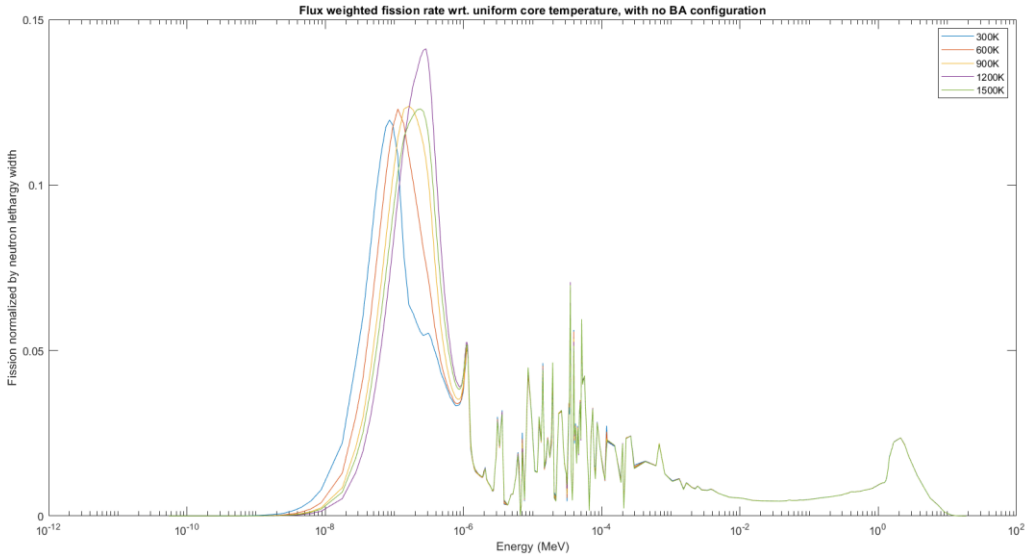

Figure 2-19. Relative fission rate of the unpoisoned core at different temperatures.

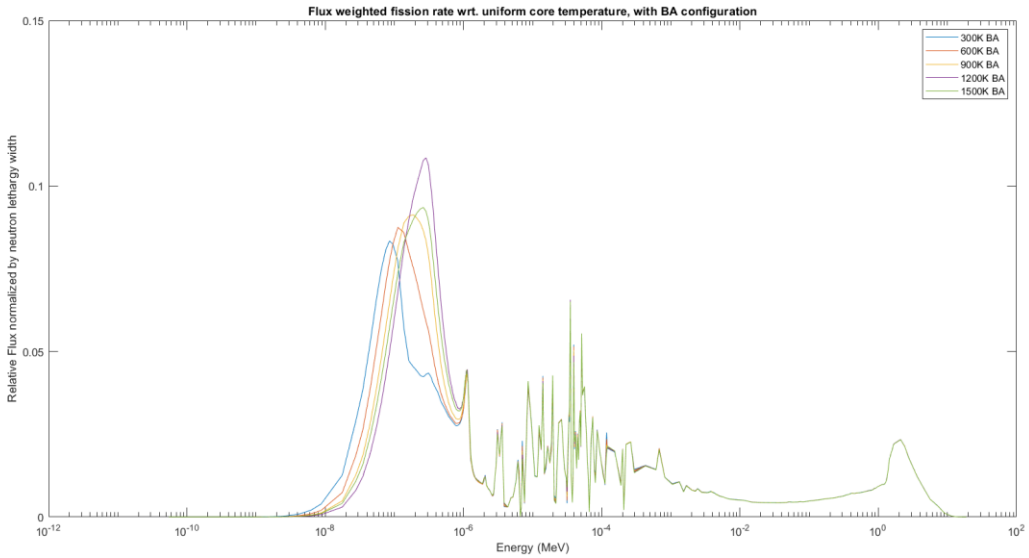

Figure 2-20. Relative fission rate of the poisoned core at different temperatures.

Based on these results, it is not clear if the shutdown rod designed as-is would be sufficient by itself to shut down the core in an emergency. Further studies are recommended and discussed in Future Work.

2.3 Thermal Performance

2.3.1 Heat Pipe Operating Limits

Heat pipes are isothermal heat transfer devices capable of transferring large amounts of heat without the use of pumps or other moving parts by a phase change transition and capillary action of a working fluid. High temperature heat pipes use for nuclear reactor applications generally use liquid metal coolants, such as potassium, sodium, or lithium.

Heat pipes are subject to temperature and power related operating limits. Outside of these limits, heat pipes can fail or underperform. The main operating limits of heat pipes are the viscous or vapor pressure limit, sonic limit, entrainment limit, capillary or wicking limit, and the boiling limit. **For the convenience of the reader, the equations and correlations to compute heat pipe operating limits as discussed in Zohuri's textbook are summarized succinctly in the following sections, with some portions included verbatim.**

The viscous limit occurs when the pressure drop in the vapor core is overcome by the viscous forces opposing it [56] [14]. This limit is typically encountered at low vapor pressures during startup when the working fluid is more viscous and sluggish, for cryogenic heat pipes, or heat pipes with very long condenser sections [56]. During normal operation with fully melted metal coolant, this limit is not encountered [14]. The viscous limit is found as:

$$\dot{Q}_{viscous} = \frac{r_v^2 \lambda \rho_{ve} P_{ve}}{16 \mu_{ve} L_{eff}}$$

where

- r_v is the radius of the vapor core (m).
- λ is the latent heat of vaporization (kJ/kg).
- ρ_{ve} is the vapor density in the evaporator section (kg/m^3).
- P_{ve} is the vapor pressure in the evaporator section (Pa).
- μ_{ve} is the vapor dynamic viscosity in the evaporator section (Pa-s).
- $L_{eff} = L_{adiabatic} + \frac{1}{2}(L_{evaporator} + L_{condenser})$, the effective length (m).

The sonic limit or choking limit occurs when vapor leaves or enters the evaporator or condenser sections at sonic speeds. Since mass transfer and circulation of liquid occurs in both the evaporator or condenser sections, they tend to act as a nozzle for vapor flow. The converging-diverging path imposed on the vapor flow can choke at sonic velocities since "the velocity [of vapor] at a choke point cannot be greater than the local speed of sound." [56] The sonic limit is typically encountered during frozen startup and disappears in the normal operating range. The sonic limit is given by [56]:

$$\dot{Q}_{sonic} = A_v \rho_0 \lambda \left[\frac{\gamma_v R_v T_v}{2(\gamma_v + 1)}\right]^{\frac{1}{2}}$$

where

- A_v is the cross sectional area of the vapor core (m^2).
- λ is the latent heat of vaporization (kJ/kg).
- ρ_0 is the vapor density at the stagnation point (kg/m^3) which can be found for isentropic flow (for a calorically perfect gas) with the following equation [57]:
    - $\frac{\rho_0}{\rho_v} = \left(1 + \frac{\gamma_v - 1}{2} M^2\right)^{\frac{1}{1-\gamma_v}}$

- M is the Mach number, the ratio of the fluid velocity to the fluid speed of sound. The Mach number is not known a-priori and in this case is assumed to be equal to 1 (sonic flow). A Mach number greater than 1 is supersonic flow.
- R_v is the specific gas constant of the vapor (J/kg-K), which can be found as:
    - $R_v = \frac{\bar{R}}{\bar{M}}$, where $\bar{R}$ is the ideal gas constant (8314 J/kg-mol-K) and $\bar{M}$ is the molecular number of the vapor.
    - In the case of sodium, $\bar{M} = 23\ \text{mol}^{-1}$ and thus $R_v = 361\ \frac{\text{J}}{\text{kg·K}}$.
- T_v is the vapor temperature (K).
- $\gamma_v = \frac{C_V}{C_P}$ is the ratio of specific heats at constant volume and pressure respectively.

The entrainment limit refers to the shear force applied as vapor and liquid move past each other in opposite directions. The magnitude of this shear force depends on the thermophysical properties of the coolant, the temperature, and the velocities of the fluid and vapor flow. When the shear force exceeds the surface tension of the liquid, it can tear away liquid droplets from the liquid flow channel – and at large enough shear forces will cause dryout in the evaporator [56]. The wick structure of the heat pipe may help ameliorate entrainment; a wick with a smaller surface pore hydraulic radius will tend to retain its liquid content better. The entrainment limit is found with [56]:

$$\dot{Q}_{entrainment} = A_v \lambda \left(\frac{\sigma \rho_v}{2 r_{h,s}} \right)^{\frac{1}{2}}$$

where

- A_v is the cross sectional area of the vapor core (m^2).
- λ is the latent heat of vaporization (kJ/kg)

- σ is the surface tension of sodium liquid (N/m).
- $r_{h,s}$ is the surface pore hydraulic radius of the heat pipe wick (m) .
    - For various types of wicks, $r_{h,s}$ is determined as [56]:

Table 2-5. Wick hydraulic radius.

Wick Type	$r_{h,s}$	Data
Wrapped Wire Screen	$r_{h,s} = 0.5w$	$w =$ wire spacing
Rectangular Grooves	$r_{h,s} = w$	$w =$ groove width
Packed spheres (sintered wick)	$r_{h,s} = 0.41r_s$	$r_s =$ sphere radius

The capillary or wicking limit is one of the most important limiting cases for heat pipe operation. The capillary limit is encountered when liquid coolant in the wick is vaporized faster than it can be replenished by capillary pumping or wicking action. When the capillary limit is encountered, liquid will continuously deplete from the wick until dryout. The structure of the wick is crucial to avoiding the capillary limit to select a wick that can sufficiently meet the rate of liquid removal. The capillary limit is chiefly determined by the pressure drops of the working fluid and frictional terms governing the capillary pumping of liquid by the wick. A simplified equation for the capillary limit is presented by Zohuri as [56]:

$$Q_{capillary} = \frac{(QL)_{cap}}{L_{eff}}$$

and

$$(QL)_{cap} = \frac{\frac{2\sigma}{r_c} - \Delta P_{\perp} - \rho_l g L \sin(\psi)}{F_l + F_v}$$

where

- r_c is the effective capillary radius (m), which can be found for different wick types:

Table 2-6. Wick effective capillary radius.

Wick Type	r_c	Data
Wrapped Wire Screen	$r_c = \frac{w+d}{2} = \frac{1}{2N}$	w = wire spacing d = wire diameter N = mesh number (number of wires per unit area)
Rectangular grooves	$r_c = w$	w = groove width
Packed spheres (sintered wick)	$r_c = 0.41 r_s$	r_s = sphere radius

  - The wire mesh number and either the wire diameter or wire spacing is typically selected/chosen when designing a heat pipe and the remaining quantity calculated.

- The $\Delta P_\perp$ term refers to the normal hydrostatic pressure drop, or the pressure drop perpendicular to the axis of the heat pipe. This pressure drop requires "circumferential communication" [56] of the fluid. If the wick type does not permit circulation along the circumference of the heat pipe inner wall (for example, a rectangular grooves wick), then this term is zero.
- $\Delta P_\perp = \rho_l g d_v \cos(\psi)$.
  - ρ_l is the liquid density (kg/m^3).
  - g is gravitational acceleration (9.8 m/s^2).
  - d_v is the diameter of the vapor core (m).
  - ψ is the inclination angle of the heat pipe.
- The $\rho_l g L \sin(\psi)$ term refers to the axial hydrostatic pressure drop, or $\Delta P_\parallel$. Here, L is the total length of the heat pipe (m).
- F_l and F_v are the liquid and vapor frictional coefficients respectively ([N/m^2]/Wm)

Liquid frictional coefficient is found using [56]:

$$F_l = \frac{\mu_l}{K A_w \lambda \rho_l}$$

where

- μ_l is the liquid dynamic viscosity (Pa-s).
- K is the permeability (m^2).
- A_w is the wick cross sectional area (m^2).
- λ is the latent heat of vaporization.
- ρ_l is the liquid density (kg/m^3).

The permeability depends strongly on the type of wick. For different wick types, the permeability and porosity could be found using [56]:

Table 2-7. Wick porosity and permeability.

Wick Type	Porosity, ϵ	Permeability K (m^2)	Data
Wrapped Wire Screen	$\epsilon = 1 - \frac{1.05N\pi d}{4}$	$K = \frac{d^2\epsilon^3}{122(1-\epsilon)^2}$	$d =$ wire diameter $N =$ mesh number
Rectangular Grooves	$\epsilon = \frac{w}{s}$	$K = \frac{2\epsilon r_{h,l}^2}{f_l Re_l}$	$w =$ groove width $s =$ groove pitch $r_{h,l} = \frac{2w\delta}{w+2\delta}$ • The liquid hydraulic radius • δ is the groove depth $f_l Re_l$ is the drag coefficient and Reynolds number. For rectangular groove wicks, refer to Figure 2-21
Packed Spheres (sintered wick)	ϵ porosity as high as 0.900 has been reported for sintered nickel wick.	$K = \frac{r_s^2\epsilon^3}{37.5(1-\epsilon)^2}$	$r_s =$ sphere radius ϵ, the porosity, depends the material and manufacture of the wick

$f_l Re_l$ for rectangular groove wicks can be found using Figure 2-21 reproduced from Zohuri [56]. Note that this figure assumes laminar flow. For non-laminar flow, see Zohuri [56] for correlations. Liquid metal heat pipes typically have low liquid velocities and laminar flow is a good assumption.

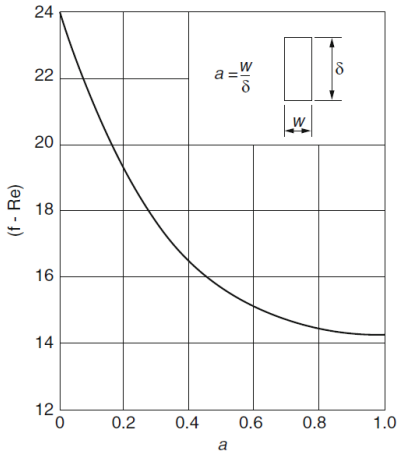

Figure 2-21. Vapor drag and Reynolds number for laminar flow in rectangular groove wick heat pipes.

Vapor frictional coefficient is found using [56]:

$$F_v = \frac{(f_v Re_v)\mu_v}{2r_{h,v}^2 A_v \rho_v \lambda}$$

where

- $f_v Re_v$ is the vapor drag coefficient and Reynolds number respectively, see figure below.
- μ_v is the vapor dynamic viscosity (Pa-s).
- $r_{h,v}$ is the hydraulic radius of the vapor flow (see above for hydraulic radius of various wick types).
- A_v is the vapor core cross sectional area (m^2).
- ρ_v is the vapor density (kg/m^3).

- λ is the latent heat of vaporization.

For flow in annular channels, the vapor drag coefficient and Reynolds number is given in Figure 2-22. Note that a wire screen wick and packed spheres/sintered wick are not the same as an annular channel wick, but in this analysis, the correlation for the annular wick is used for both (lacking a better alternative).

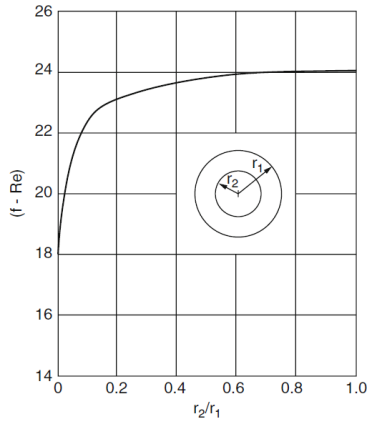

Figure 2-22. Vapor drag and Reynolds number for laminar flow in circular cross section heat pipes

The boiling limit is also an important operating limit that typically places restrictions on the upper bounds for temperature and heat removal capabilities of heat pipes. The boiling limit occurs when vapor bubbles forming in the wick as the coolant evaporates become trapped in the wick itself. The trapped vapor bubbles block the returning liquid flow in the wick and eventually leads to dryout of the wick. The boiling limit is typically not encountered for liquid metal heat pipes used in nuclear reactor applications [56]. The boiling limit is sensitive to the formation and size of vapor bubbles, which in turn is determined by nucleation sites in the wick, surface roughness properties, and the contact angle of vapor bubbles during formation [56]. These parameters would depend on the materials used, manufacturing process of the wick, etc. and can be difficult to determine without experimental measurements of a prototype design. However Holland and

Winterton have collected experimental measurements of the nucleation radius of sodium at incipient boiling for various pressures and temperatures. At 1 atm and 861 °C, the radius of nucleation bubbles was about 2.8 μm [58]. The boiling limit is then found using [56]:

$$\dot{Q}_{boiling} = \frac{2\pi L_E k_{eff} T_v}{\lambda \rho_v \ln\left(\frac{r_i}{r_v}\right)}\left(\frac{2\sigma}{r_n} - P_c\right)$$

where

- L_E is the length of the evaporator (m).
- k_{eff} is the effective thermal conductivity of the liquid-wick combination.
    - For different wick structures, the effective thermal conductivity of the liquid saturated wick can be found with the following expressions (from Zohuri) [56]:

Table 2-8. Wick effective thermal conductivity.

Wick Structure	k_{eff}
Wrapped wire screen	$k_{eff} = k_l \frac{(k_l + k_w) - (1-\epsilon)(k_l - k_w)}{(k_l + k_w) + (1-\epsilon)(k_l - k_w)}$ • ϵ is the porosity.
Rectangular grooves	$k_{eff} = \frac{(w_f k_l k_w \delta) + (w k_l)(0.185 w_f k_w + \delta k_l)}{(w + w_f)(0.185 w_f k_w + \delta k_l)}$ • w_f is the groove fin thickness. • w is the groove thickness. • δ is the groove depth.
Packed spheres/sintered	$k_{eff} = k_l \frac{(2k_l + k_w) - 2(1-\epsilon)(k_l - k_w)}{(2k_l - k_w) + (1-\epsilon)(k_l - k_w)}$

    - k_l and k_w are the thermal conductivities of the liquid and wick material respectively.
- T_v is the vapor temperature (K).
- λ is the latent heat of vaporization (kJ/kg).
- ρ_v is the vapor density (kg/m^3).

- r_i is the radius of the inner wall of the heat pipe (m).
- r_v is the radius of the vapor core (m).
- σ is the surface tension (N/m).
- r_n is the nucleation radius of vapor bubbles at incipient boiling (m).
- P_c is the capillary pressure (Pa).
    - The boiling limit reaches its minimum at the maximum capillary pressure.
    - Maximum capillary pressure can be found as:

$$P_{c,\max} = \frac{2\sigma}{r_c}$$

where r_c is the effective capillary radius.

Since the nucleation radius of vapor bubbles during formation tends to be much smaller than the capillary radius, the boiling limit seldom occurs in liquid metal heat pipes.

2.3.2 Heat Pipe Down-Selection

Sodium is the choice of working fluid for its high boiling point, operating temperature, and transparency to neutrons. Sodium heat pipes' useful temperature range is typically between 873 K to 1473 K (600 °C to 1200 °C) [59] with a neutron absorption cross section in the sub-millibarns range [60]. The performance of a fluid for a heat pipe is qualified by the merit number as a function of temperature, which is found as:

$$N_l = \frac{\rho_l \sigma \lambda}{\mu_l}$$

where all symbols have their usual significance [47]. Among liquid metal coolants, sodium has the highest merit number [47]. Furthermore, sodium heat pipes have gained much experience with long-running experiments accumulating tens to hundreds of thousands hours of operation [61].

The choice of wick structure determines the power and temperature operating limits of the heat pipe. Wick materials compatible with sodium include stainless steel, Inconel, nickel, and molybdenum [47]. Of these, nickel is the choice of material for the wick. Various studies have been conducted investigating and experimenting with sintered nickel powder wicks, providing evidence of experimental measurements and manufacturing capability for high performance sintered nickel wicks [62] [63] [64] [65].

Next, for a given heat pipe geometry, the operating limits are calculated (see Heat Pipe Operating Limits). The capillary and entrainment limits were found to be the most constraining limits. For a sintered wick, the capillary limit is very strongly dependent on the porosity (ϵ) of the wick, since ϵ^3 and $(1-\epsilon)^2$ appears in the numerator and denominator of the permeability of the wick respectively. Even a small change in the porosity can greatly swing the capillary power limit over all temperatures. The capillary limit is also dependent on the radius of the vapor core and powder particle diameter, albeit not as strongly as the porosity. Recalling the equations for the liquid and vapor frictional coefficients:

$$F_l = \frac{\mu_l}{K A_w \lambda \rho_l}$$

$$F_v = \frac{(f_v Re_v)\mu_l}{2 r_{hv}^2 A_v \lambda \rho_v}$$

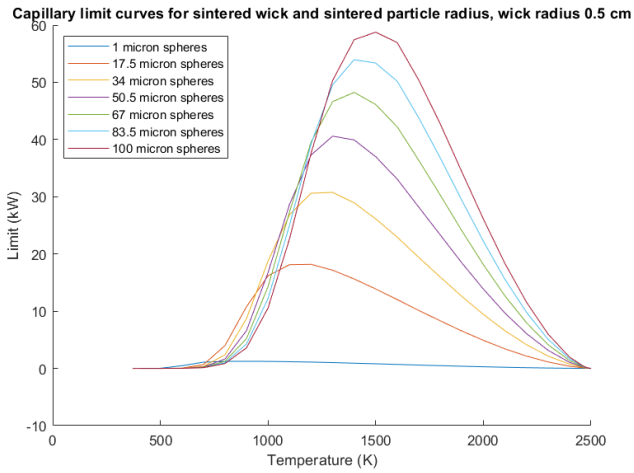

Figure 2-23. Typical family of capillary limit curves for a sintered wick with variable powder particle size.

The cross sectional area of the wick and vapor core both depend on the radius of the vapor core, which in turn is determined by or determines the thickness of the wick. The capillary limit will maximize at some intermediate value of the vapor core radius where the sum of the liquid and vapor coefficient terms is minimized. With this in mind, the vapor core radius and powder particle size can be parametrized to calculate the capillary limit for various combinations, each combination a unique wick thickness and sintered powder particle size.

Likewise, the entrainment limit depends on the size of the vapor core and the inverse square-root of the hydraulic radius, which only varies linearly with powder particle diameter. Supposing that the vapor core radius is close to its optimum, increasing it will tend to also increase the entrainment limit at the cost of decreasing the capillary limit. Also, increasing the sintered particle sphere size will decrease the entrainment limit but increase the capillary limit. Designing the heat pipe around the capillary and entrainment limits will involve trade-offs between these two limits.

For a given heat pipe inner radius, there will exist a vapor core radius that maximizes the capillary limit. When the best vapor core radius is identified, the particle size of the sintered wick powder is varied until the capillary and entrainment limit requirements balance out. The maximum operating power of the heat pipe balanced between the capillary and entrainment limit is ultimately limited by the inner radius of the heat pipe; if this is found to be too low to remove sufficient heat from the reactor, the heat pipe inner radius must be increased, and the process repeated.

The initial heat pipe design considered three types of wicks: rectangular grooves, wrapped wire screen, and sintered. It was quickly found for realistic wick features, the rectangular grooved and wrapped wire screen wicks' liquid frictional coefficient would be far too high; the capillary pumping capability of these wicks was not sufficient to overcome the pressure drop over the pipe.

The sintered wick initial design parameters and final design parameters are found in Table 2-9. The final design was found by the process described above, by parametrizing the vapor core radius and sintered particle sphere size and calculating the most limiting operating limits (capillary and entrainment) for each unique wick combination. For a reactor power of 15 MWth and a total of 1224 heat pipes, each heat pipe needs to remove about 12.25 kW of power on average. Heat pipes located near peak power regions would need to remove more (see Core Power Distribution and Peaking Factors). Also accounting for a failed heat pipe scenario and including a conservative operating margin further increases the total heat each pipe must be able to remove. With these constraints in mind, the desired heat removal for the heat pipe design is about ~25 - 30 kW.

Table 2-9. Sintered wick heat pipe parameters.

Sintered wick HP design parameters	Initial	Final
Wick material	Molybdenum	Nickel
Inner pipe radius (cm)	0.6575	0.9000

Table 2-9 continued		
Vapor core radius (cm)	0.4000	0.5750
Radius of powder particle (μm)	400	45
Porosity	0.64	0.868
Calculated permeability (m^2)	$8.63*10^{-9}$	$2.03*10^{-9}$
Evaporator section length (m)	1.5	1.5
Adiabatic section length (m)	0.3	0.3
Condenser section length (m)	0.6	0.6
Heat pipe inclination angle (degrees)	0	0

The initial heat pipe design is only able to remove a maximum of about 6 kW at best. A larger heat pipe inner radius is necessary to increase the capillary and entrainment limits. This necessitates an increase in the lattice pitch of the reactor core block to accommodate larger heat pipes. The porosity of molybdenum wicks is assumed to be 0.64. The porosity is the most sensitive parameter when calculating the capillary limit (see Heat Pipe Operating Limits); increasing the capillary limit by improving the porosity allows the entrainment limit to be tweaked as well. Studies on sintered nickel wicks have shown very high possible porosities using filamentary nickel powder [62] [63] [64] [65]. The selected porosity is 0.868, but Holley and Faghri have claimed the porosity of a nickel wick as high as 0.900 [62] (see Future Work). The finalized heat pipe design increases the radius of the heat pipe by about ~36% but pushes the peak power removal to over 30 kW. Furthermore for the initial case, it is unclear how realistic 800 micron diameter molybdenum particles are in regards to manufacturing a sintered molybdenum powder wick. Commercial suppliers of molybdenum powder typically provide particles in the <10 micron size range [66], whereas nickel powders can be supplied up to 150 microns particle size [67].

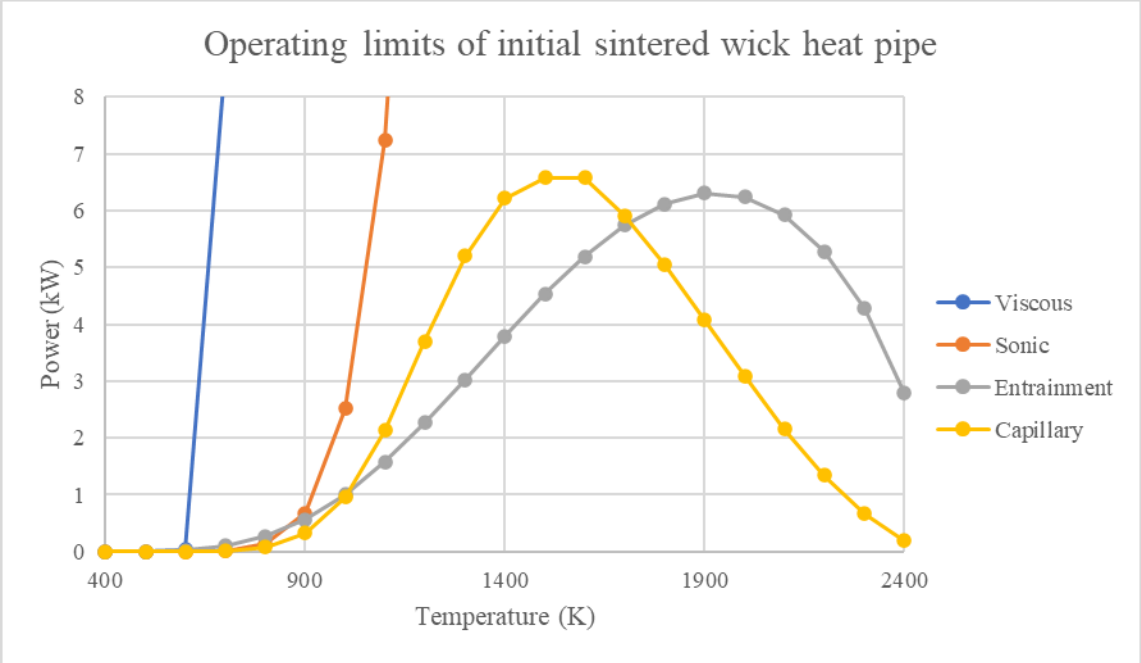

Figure 2-24. Calculated operating limits of a heat pipe with sintered molybdenum wick and 0.6575 cm inner radius.

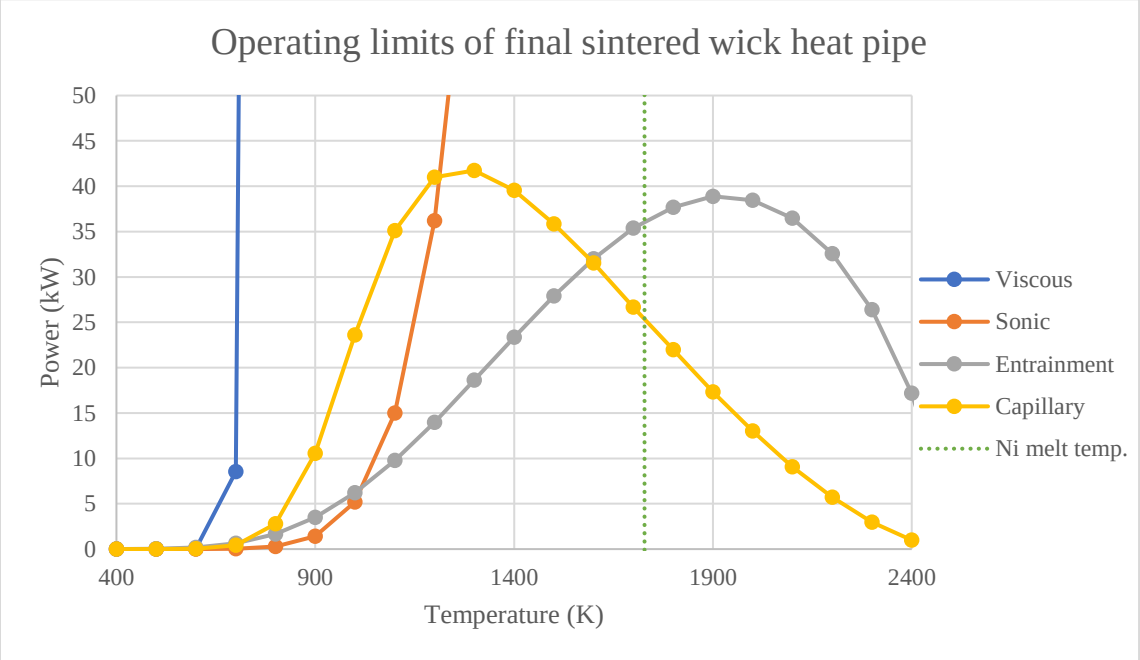

Figure 2-25. Calculated operating limits of a heat pipe with sintered nickel wick and 0.9000 cm inner radius.

The limits important for the proposed heat pipe design are the sonic, capillary, and entrainment limits. The viscous limit above 700 K is well above the maximum power needed to be removed by each heat pipe. The boiling limit only becomes important near the boiling temperature of sodium (2503.7 K) and otherwise does not inhibit the heat pipe in its normal operating envelope. For reference, the boiling limit was calculated for the nickel wick but is not meaningful to show included in the plot for Figure 2-25; at 1700 K, the boiling limit is in the ~10^6 kW range. The capillary and entrainment limits eclipse the boiling limit within the relevant temperature range. The full operating range of the heat pipe is the overlapping area enclosed under all curves: the roughly triangular envelope between 800 K to 2400 K, but also includes the cutoff at the nickel melting temperature at 1728 K.

The nickel wick incurs a neutronic penalty compared to a molybdenum wick. This effect was quantified by using the 3D full core geometry (original/unexpanded lattice) and 30 cm thick radial and axial graphite reflector and 30 MW thermal power (which is later set to 15 MW). Comparing the cycle of otherwise identical reactors with nickel vs molybdenum wicks at 0.75 porosity (or 0.25 theoretical density) found that:

- Nickel Wick
    - BOC K-eff: 1.24964 ± 0.00022
    - DBU: 68.8496 MWd/kgU
    - ~5475 days cycle length (~15 years)
- Molybdenum Wick
    - BOC K-eff: 1.25472 ± 0.00021
    - DBU: 73.7675 MWd/kgU
    - ~5730 days cycle length (~15.7 years)

A penalty of about 6.66% to the discharge burnup is significant, but not prohibitive. While this test run did not use the expanded lattice with larger heat pipes, it is anticipated the discharge burnup penalty in the expanded lattice will be comparable. Additionally, the wick porosity of the expanded heat pipes is higher than the test run at 0.868 compared to 0.75, which should modestly reduce the burnup penalty as well. With this in mind, the use of a nickel wick to meet heat pipe operating limits is a justifiable tradeoff.

2.3.3 Core Power Distribution and Peaking Factors

The thermal power distribution in the core determines hot spot peaking factors and sets limits on the required heat pipe performance – that is the heat pipe design must be able to remove heat from the hottest parts of the core with some margin. To calculate the power distribution, each fuel pin in the Serpent model is created as its own universe and depletable material. The power distribution is taken as the fission energy production in each fuel pin tallied with a hexagonal lattice detector over the entire core. By partitioning the tally lattice and fuel pins themselves into 10 equal length segments, both radial and axial distributions of power are found. For illustrative purposes, Figure 2-26 shows the power distribution of the core at BOC and EOC; see Full Core Power Distribution Plots in the appendix for full plots at all cycle steps.

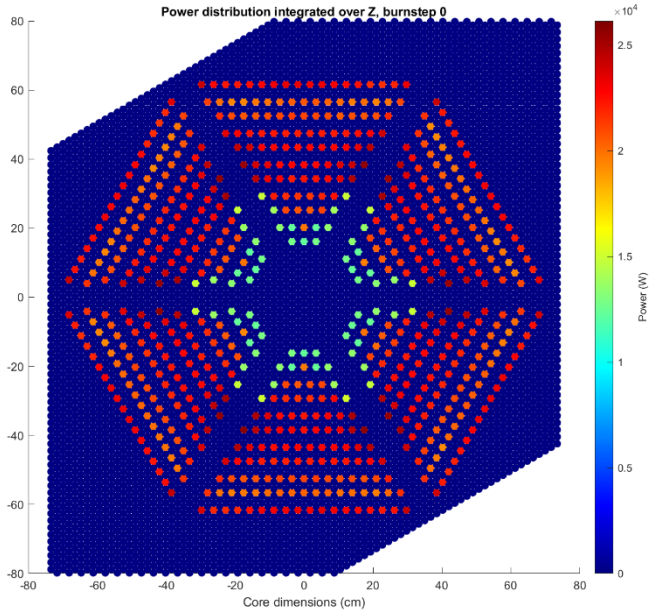

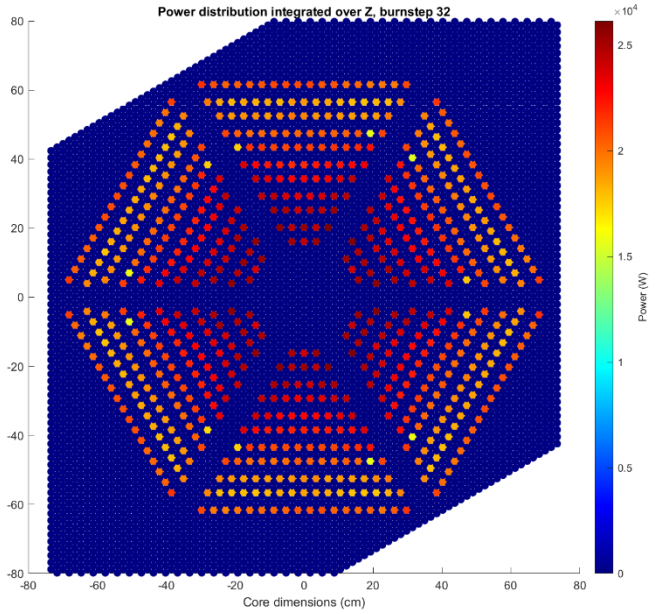

Figure 2-26. Thermal power distribution of the first and last, tallied by fission energy generation in fuel rods.

Peaking factors can then be calculated from the numerical power tallies. The radial peak to average over the full core is the ratio of the full power (over its entire axial length) of the highest

power producing fuel pin to the average thermal power of all fuel pins. The radial peak to minimum over the full core is the full power of the highest power producing fuel pin to the full power of the lowest/coldest power producing pin. The full core itself is segmented into 10 axial segments. The hot-slice peak to average is the power produced by the hottest fuel pin segment in the hottest core slice to the average power of that slice. The axial average peaking factor is the average power produced in the hottest slice to the average full core power of the whole reactor. For clarity, only the peaking factors for the poisoned core loaded with GdN is shown in Figure 2-27. In Figure 2-28, the peaking factors for both the poisoned and unpoisoned core are plotted together to show the effect of gadolinium loading on the peaking factors over the fuel cycle.

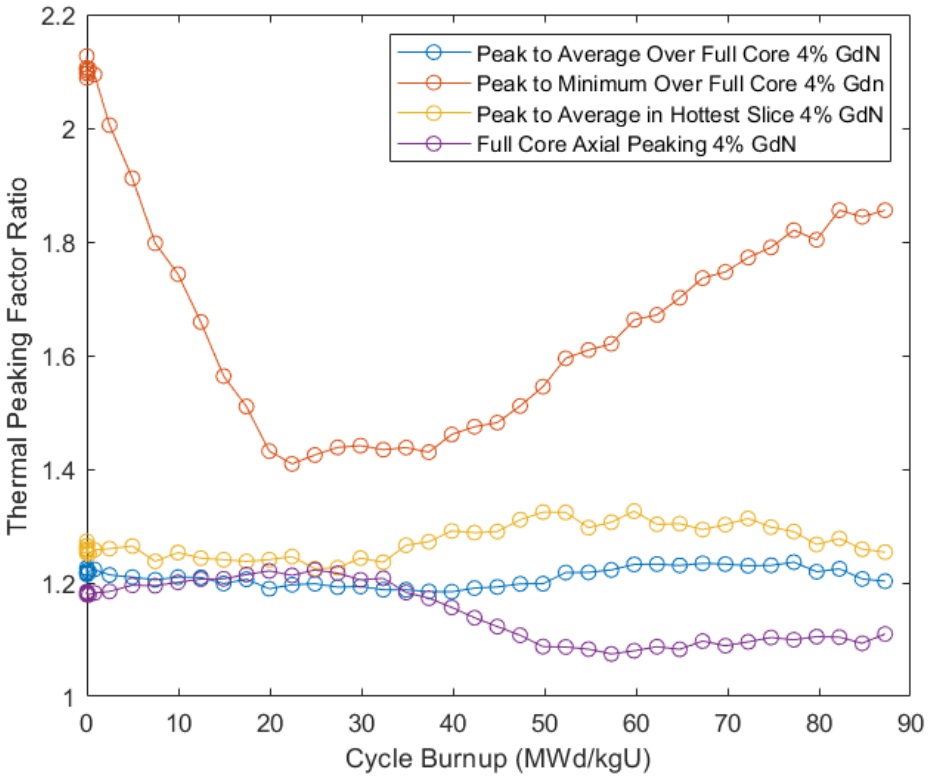

Figure 2-27. Change in thermal peaking factors over the cycle.

The addition of gadolinium nitride burnable absorber has a strong dampening effect on the thermal power distribution towards the beginning of cycle, as is seen in Figure 2-28. GdN is selectively loaded in the center-most group of fuel pins, which otherwise would be the highest power at BOC. As the rest of the core burns, the GdN loaded fuel pins gradually warm up as well; eventually the thermal distribution shifts the hot spot back towards the center of the core. However, since these fuel pins have already burned some throughout the cycle, the local hot spot peaking factor is not as severe as in the case where no GdN is loaded into the center fuel pins. The core without any burnable absorbers has a high peaking factor at the beginning of cycle at about 1.45 over the full core and 1.57 within the hottest slice. The peaking factors level off as the cycle progresses. In comparison to the full core loaded with burnable absorbers, the peaking factors tend to stay relatively constant, peaking near the end of cycle (~60 MWd/kgU) at about 1.23 over the full core and 1.35 in the hottest slice. In both cases, the peak-to-minimum peaking factors are very high near at beginning of cycle, fall off as fuel burns mid-cycle, and rise again as long-lived poison fission isotopes accumulate in the most burnt fuel pins. The axial average peaking factor is also computed; for both the poisoned and unpoisoned core it remains relatively low, peaking only slightly above 1.2.

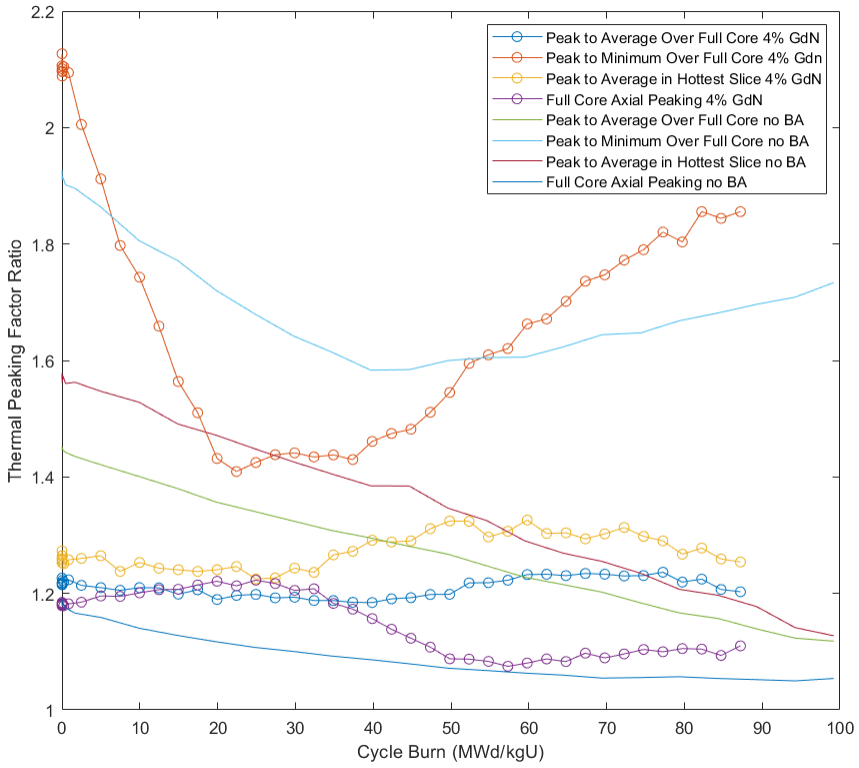

Figure 2-28. Peaking factors for the full core without any burnable absorbers and with 4% wt. GdN + BN coating burnable absorbers

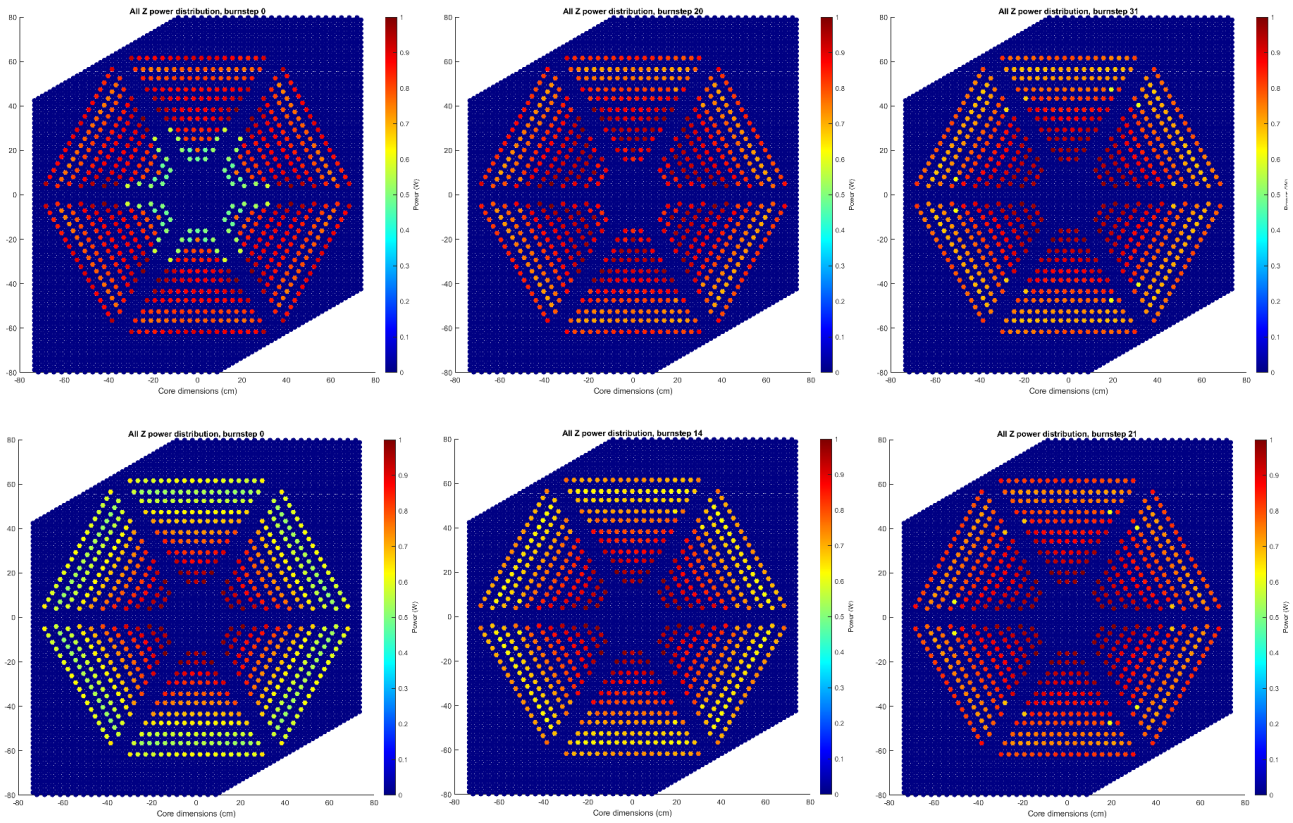

Figure 2-29. Thermal power distribution at BOC, mid-cycle, and EOC. Top: core loaded with burnable absorbers. Bottom: core with no burnable absorbers.

2.3.4 Single Heat Pipe Failure and Cascades

The heat pipes are designed such that the failure of a single heat pipe should not cause neighboring heat pipes to exceed their operating limits. Such failures must not lead to a cascading failure of multiple heat pipes and failure of the entire system. The lattice of the full core is designed such that each fuel rod is not directly adjacent to another fuel rod, that each fuel rod is directly adjacent to 3 heat pipes, and that each heat pipe is adjacent to no more than 2 fuel rods. Note that

some heat pipes are directly adjacent to one or no fuel rods. Other lattice layouts were designed and considered, but ultimately rejected since they do not meet these criteria.

Since every fuel rod is directly adjacent to 3 heat pipes, it is assumed that all fuel rods disperse 1/3 of its heat evenly to its neighboring heat pipes. And since each heat pipe is directly adjacent to no more than 2 fuel rods, the maximum total heat a single heat pipe is assumed to receive is 1/3 of the power generated by both its neighboring fuel rods.

In the expanded lattice with the reactor operating at 15 MWth power, the hottest fuel rod produces 26.15 kW of heat. Next, conservatively assuming the hotspot has 2 such fuel rods next to the same heat pipe both producing 26.15 kW of heat, the heat pipes servicing the hottest fuel rods would need to remove $2 * \left(\frac{1}{3}\right)(26.15\ kW) = 17.43\ kW$. Using the calculated operating limits of the heat pipe (see Heat Pipe Down-Selection and Figure 2-25), this power requirement can be satisfied by operating the heat pipe at least at ~1300 K.

Suppose one of the heat pipes operating at the hot spot fails. The hottest fuel rod would be directly adjacent to 2 operating heat pipes. Again, assuming the fuel rod transports its heat uniformly to its neighboring heat pipes, each of these 2 heat pipes would be required to remove half of the heat generated by the fuel rod. Again, assuming at the hotspot there are 2 such fuel rods producing 26.15 kW, these heat pipes are then required to remove $\left[\left(\frac{1}{3}\right) + \left(\frac{1}{2}\right)\right] 26.15\ kW = 21.79\ kW$. This power level would fall within the heat pipe operating limits at about ~1350 K. However, the increase in temperature in a heat pipe upon failure of a neighboring pipe would need to be determined through a detailed calculation accounting for transient behavior of the heat pipe [14]. A similar analysis by Galloway et al. had found a failed heat pipe caused an increase in coolant temperature of the neighboring heat pipes by about 120 °C [14]. A conservative approach

is to design such that each heat pipe must be able to accommodate a temperature increase of 200 °C (200 K). A projection of the possible allowed operating temperature range followed by a subsequent increase in power (to 21.79 kW) and temperature (by 200 K) is shown in Figure 2-30.

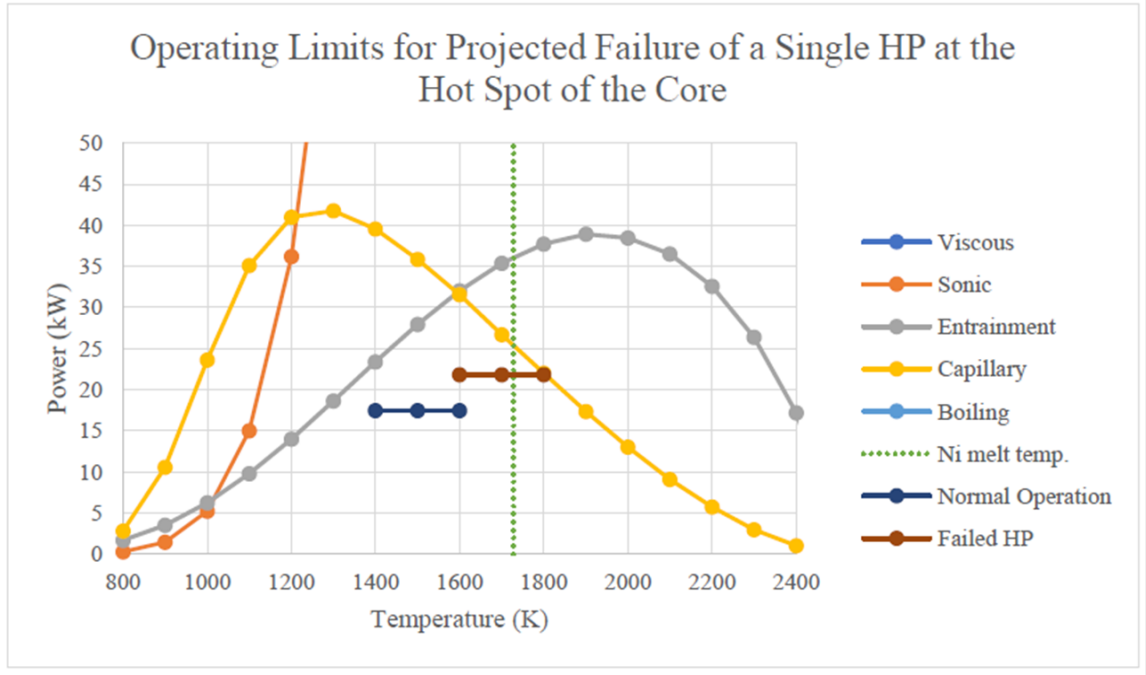

Figure 2-30. Projected operating temperature range and failed HP scenario of the HP's servicing the hottest fuel rods.

In this case, suppose the operating temperature range is set between 1400 K to 1600 K. During normal operation, the heat pipe will operate well under its operation limits within this temperature range. But in the case of a failed heat pipe and conservatively assuming an increase in the coolant temperature by 200 K would exceed the melting temperature of the nickel wick if the normal operating temperature is set to higher than 1528 K. Therefore, to avoid melting the wick while accommodating a failed heat pipe and conservative 200 K coolant temperature increase, the normal operating temperature range of the heat pipe should be set between 1400 K to 1500 K. This proposed temperature range is nearly aligned with the typical useful operating temperature range of sodium in heat pipes at 873 K to 1473 K (600 °C to 1200 °C) [47]. In this case, the heat pipe

would operate well under its operating limits during normal circumstances and still operate after a single heat pipe failure while still retaining some margin. It should be noted that this places the failed heat pipe range on the right side of the "triangle" under the operating limit curves; i.e.: the operating limit begins decreasing with respect to temperature past 1600 K. While there still remains enough margin to not exceed the operating limits, this is a salient concern that warrants final validation and verification through a detailed calculation of heat pipe transients or experimental measurement.

2.4 Economic Estimates

Economics analysis is undertaken as a break-even cost analysis. There are many unknowns that make it very difficult if not impossible to accurately calculate the costs of a microreactor. Generally speaking, technology improvements such as metal hydride moderators, the Advanced Moderation Module, monoblock manufacturing, etc. costs for procurement, fabrication and so on are not known. Some quantities, such as the fuel cost, can be estimated with some certainty. For a given cost of electricity, and for a set of known costs, the break-even cost to bring the reactor to market for all other expenses could be estimated.

2.4.1 Fuel Cost

Uranium enrichment is fixed at 19.75%. The cost of enrichment is calculated using the following equations [68] [69].

The relationship between feed (F), enriched uranium (P), waste tailings (W) on a per-mass basis, and their respective concentrations ($x_{f,p,w}$):

$$F = P + W$$

$$x_f F = x_p P + x_w W$$

$$\frac{F}{P} = \frac{x_p - x_w}{x_f - x_w}$$

$$\frac{W}{P} = \frac{F}{P} - 1$$

Separation potential and SWU-factor expressed in SWU per kg (separative work units):

$$V(x_i) = (2x_i - 1)\ln\left(\frac{x_i}{1 - x_i}\right)$$

$$S = V(x_p) + \frac{W}{P}V(x_w) - \frac{F}{P}V(x_f)$$

The price of enrichment per kg of uranium is then expressed as:

$$\dot{P}_E = \left[\frac{\dot{P}_U}{(1 - \ell_c)(1 - \ell_f)} + \frac{\dot{P}_C}{(1 - \ell_f)}\right]\frac{F}{P} + \frac{\dot{P}_S}{1 - \ell_f}S$$

where $\dot{P}_E, \dot{P}_U, \dot{P}_C, \dot{P}_S$ are the costs of enrichment, uranium ore, conversion, and SWUs per kg respectively. ℓ_f and ℓ_c are losses during fuel fabrication and conversion respectively; zero losses are assumed for this analysis.

Fuel cost is then the cost of enriched uranium plus the cost of fabrication. For nitride fuel, it is assumed the fabrication cost (per kg) includes the cost of nitriding. Nitrogen is required as enriched nitrogen-15, which is also assigned a cost in a per kg basis. For a fixed uranium enrichment and stoichiometry of uranium mononitride (UN), the kg of nitrogen per kg of uranium in fuel will be known. Thus, the final fuel cost per kg is found as:

$$\dot{P}_{UN} = \dot{P}_E + \dot{P}_F + \eta\dot{P}_N$$

where $\dot{P}_{UN}, \dot{P}_E, \dot{P}_F, \dot{P}_N$ are the costs of UN fuel, enrichment, fabrication, and nitrogen-15 in a per kg basis, and η is the mass ratio of nitrogen-15 to uranium in the final fuel product.

Fuel rods are clad in silicon carbide (SiC). The cost of SiC material and cladding fabrication is not known with certainty. However in 2012, Barrett et al. studied advanced cladding for LWRs,

including SiC clad for UO_2 fuel, which they estimated cost about 30 times more than standard zirconium alloy cladding [70]. Based on a zirconium alloy cost of $37 - $55 per kg LEU, the cost of SiC can be estimated assuming a similar fabrication process and cladding thickness.

2.4.2 Core Material Cost Estimate

Not every material cost is known. Nor is the cost associated with manufacturing, assembly of the core, licensing, or any on-site construction. The costs of fuel, moderator, and monoblock are estimated on a mass basis. No attempt is made to assess the costs of the heat pipes, hydride moderator hydrogen barrier cladding [28], or burnable absorber materials. shows the assumed price of the associated materials.

Table 2-10. Assumptions for UN fuel cost estimates.

Item	Value	Comment
UN Fuel Costs		
U_3O_8 ore ($\dot{P}_U$)	121.25 ($/kgU) [71]	55 ($/lb)
Conversion Price ($\dot{P}_C$)	12 ($/kg-UN) [71]	
SWU Price ($\dot{P}_S$)	142 ($/SWU) [71]	
Fabrication Price ($\dot{P}_F$)	275 ($/kgU) [71]	
Nitrogen-15 ($\dot{P}_N$)	1130 ($/kg-^{15}N) [71]	
SiC Cladding ($\dot{P}_C$)	1650 ($/kg-UN) [70]	Based on 30x the price of zirconium alloy cladding for LWRs priced at $55 per kg LEU
Core Materials		
Nuclear-grade graphite	15 ($/kg) [72]	Cited price ranges from $7,000 to $20,000 per metric ton for 99.9% purity graphite (Dec. 2011 prices)
YH_2 Powder	50 ($/kg) [30]	

Based on these prices, the cost of cladded fuel is determined to be $13,497.03 per kg.

The active core measures 150.7 cm in diameter and 150 cm in height for the expanded lattice configuration (see Lattice Pitch Expansion). There are a total of 708 and 1416 fuel and moderator rods respectively. The graphite monoblock is assumed to be milled or drilled to create penetrations

for fuel, moderator, and heat pipes, and so the total mass of graphite required is for the unmilled, solid cylindrical block. summarizes the relevant dimensions, densities, total volumes, and calculated material costs for fuel, moderator, and graphite monoblock.

Table 2-11. Fuel, monoblock, reflector, and moderator material cost estimates.

Item	Size	Quantity	Total Vol.	Density	Material Cost ($)
UN fuel	1.423/150 cm dia/height	708 rods	168900 cm^3	14.016 g/cm^3	32,041,027.52
Graphite monoblock	150.7/150 cm dia/height	-	2675500 cm^3	2.20 g/cm^3	72,830.38
Graphite reflector*	30 cm* thick	-	2574400 cm^3	2.20 g/cm^3	84,956.65*
YH_2 moderator	1.425/150 cm dia/height	1412 rods	338750 cm^3	4.3 g/cm^3	88,292.05

The cost of the reflector varies based on the thickness of the reflector. Assume the thickness of the radial and axial reflectors is the same. The volume of the radial reflector is simply $V_{ref,r} = (R_o^2 - R_i^2)\pi T$ and the axial reflector is $V_{ref,a} = 2(\pi R_o^2 T)$ where R_i and T is the active core radius and thickness of the reflectors respectively. The outer radius of the radial reflector is simply $R_o = R_i + T$. Using the same graphite pricing and using the same thickness for both radial and axial reflectors, the cost of the reflector ranges between about $85,000 to $340,000 for a thickness of 30 cm to 90 cm.

2.4.3 Cost of Electricity to Breakeven

The core configuration considered for fuel cycle cost is the expanded lattice with nickel heat pipe wick and 1:1 fuel to moderator rod size (0.7125 cm moderator rods). A thermal power of 15 MWth is prescribed so that all heat pipes will operate within operational limits, even if a heat pipe

in the hot spot of the reactor fails, with some extra margin. The discharge burnup for this cycle was found to be 62.09 MWd/kgU with a cycle length of 25 years. The conversion efficiency and capacity factor is assumed to be 33% and 95% respectively.

For a given cost of electricity assumed constant, the reactor will receive a fixed equal payment each month. This sum is treated as a monthly annuity stream of equal payments and using the 25-year cycle length, and these payments must be discounted to the present value. Likewise, all other costs of the reactor have been treated as a lump sum payment 1 year prior to the present value; or in other words, the opportunity cost of the capital investment to construct the reactor is the interest that would have otherwise been earned by investing the cost of the reactor. The present value of an annuity stream is:

$$PV_{as} = P\frac{1-(1-i_m)^{-N}}{i_m}$$

and the present of the lump sum payment is:

$$PV_{ls} = L(1+i_m)^M$$

where P is the payment received each month for selling electricity, L is the lump sum payment to build the reactor, N, M are the number of payments in the period, and i_m is the monthly interest rate. For simplicity, the interest rate is kept constant and the same interest rate is assumed for both payments received and payment due. All quantities in the payment model are known (cost of electricity, power of the reactor, and payment period). The total lump sum payment is not known, but given that the number of payments and interest rate is known, it will be possible to determine the value the lump sum cannot exceed to breakeven on costs.

The material costs discussed earlier are treated as just one component of the lump sum payment due 1 year prior to reactor startup. Then the lump sum is written as $L = MC + RC$ where MC are

the material costs (fixed at approximately \$32.2 M) and RC are all other costs associated with bringing the reactor online (lumping manufacturing, unknown other materials, construction, licensing, R&D, etc. costs all together). Setting the present value of the received payments stream and lump sum payment due to build the reactor equal then:

$$PV_{as} = PV_{ls}$$

And rearranging this equation to determine the unknown lump reactor cost finds:

$$RC = P\frac{1-(1-i_m)^{-N}}{i_m(1+i_m)^M} - MC$$

MC is a fixed cost. As stated earlier, M, the number of payment periods prior to reactor startup, is treated as a fixed constant of 12 months. Since the reactor cycle lifetime was determined to be 25 years, N is 300 months. The payment received P depends but is uniquely determined by the price electricity could be sold at market (since reactor burnup and power are known and fixed). Likewise, the interest rate may vary. Thus, it is possible to find the cost to bring the reactor to market, minus material costs of fuel, moderator, and monoblock for any combination of electricity price and interest rate. This is essentially the breakeven "budget" that the reactor must remain within to bring the reactor to market. If the reactor is built under the budget, the difference is profit. Two trends are noted for the above equation. First, as the market rate of electricity becomes more expensive, the reactor costs become more economical. Secondly, the reactor cost favors lower interest rate. This is because with a high interest rate, the capital required to build the reactor is better off being invested to start generating income immediately, instead of being spent to build a reactor that only generates a fixed income over a number of years into the future. The future income is discounted to the present value; ie: \$1,200 today is worth more than \$100 every month for a year.

Electricity costs in Alaska vary considerably for different regions and providers. According to the IAEA, about "10% [of utilities] can supply electricity at a reasonable price below $0.10/kWh. More than 50% of utilities supply very expensive electricity at over $0.30/kWh [73]." For example, electricity prices range from $0.41/kWh in Nome, Alaska to $1.02/kWh in Takotna, Alaska [74]. Another potential market are mining operations, which typically pay between $0.20/kWh to $0.50/kWh [74]. Furthermore, for mining operations, there may be potential for co-generation of process heat and the need for highly reliable power generation. The first of its kind in the market microreactor would compete against expensive utility providers; as more experience is gained and more units manufactured, the costs could conceivably be reduced to compete against cheaper providers.

Operations and maintenance (O&M) costs for microreactors are affected by a variety of factors, such as the remoteness of the installation location, new/unfamiliar reactor designs, level of autonomy in operation, and so on. The Nuclear Energy Institute (NEI) has estimated the cost of O&M to range between $250/kWe to $450/kWe per year [74]; however these estimates may be somewhat too generous. At a cost of $450/kWe, the equivalent cost to electricity would be about $0.0514/kWe. For a simple first degree approximation, this figure could be subtracted from the market rate of electricity for a particular market to come up with an equivalent cost of electricity with O&M costs factored in. In the following economic estimates (, , and), the O&M costs can be thought of as being included in the market rate for electricity at just over 5 cents per kWe.

Regarding the actual cost to build a real microreactor, nuclear reactor project costs are notoriously difficult to estimate. For instance, NuScale projected costs of $1,200/kWe capacity in the pre-conceptual phase of its 45 MWe SMR in 2003, but later increased to $5,000/kWe in 2017 [75]. Suppose a pessimistic view is adopted that a new and untested reactor technology (meaning

not a LWR) would cost more per unit capacity, at least for the first unit entering the market. The NEI has estimated the cost to bring a "first-of-its-kind" microreactor to market would range between $10,000/kWe to $20,000/kWe [74]. Adopting the conservative estimate of $20,000/kWe, the total budget for the 5 MWe microreactor cannot exceed $100 M. After factoring in $32.2 M for fuel and raw material costs, the remaining budget must not exceed $67.8 M. shows that for this simplified economic estimate, the microreactor may be economically competitive, especially favoring low interest rates and expensive electricity markets.

Table 2-12. Breakeven budget of the microreactor with fuel and material costs accounted for.

Monthly income for a given Cost of Electricity									
COE $/kWh	$0.10	$0.15	$0.20	$0.25	$0.30	$0.35	$0.40	$0.45	$0.50
Income (month)	$346K	$520K	$694K	$867K	$1.04M	$1.21M	$1.39M	$1.56M	$1.73M
Interest	Reactor Breakeven Budget (Millions of $) (including fuel cost estimate of $32.2 M)								
0%	71.89	123.94	175.99	228.04	280.09	332.13	384.18	436.23	488.28
1%	59.01	104.61	150.21	195.82	241.42	287.03	332.63	378.24	423.84
2%	48.22	88.44	128.65	168.86	209.08	249.29	289.50	329.72	369.93
3%	39.15	74.83	110.51	146.19	181.87	217.55	253.22	288.90	324.58
4%	31.48	63.32	95.17	127.01	158.85	190.69	222.54	254.38	286.22
5%	24.96	53.54	82.12	110.70	139.28	167.86	196.44	225.02	253.60
6%	19.38	45.17	70.96	96.75	122.54	148.33	174.12	199.91	225.71
7%	14.58	37.98	61.37	84.76	108.16	131.55	154.94	178.34	201.73
8%	10.44	31.76	53.09	74.41	95.73	117.05	138.37	159.69	181.02

Regarding interest rates, low interest rates (~2%) may be possible for state or community funded projects with guarantees for low interest over the period. A very low interest rate (0-1%) might correspond to a scenario where the reactor is built with an already low interest rate in a market where the cost of electricity rises each year. Higher interest rates are more typical of projects funded by capital investments.

An alternative market for microreactors is the generation and selling of process heat. An economic analysis for the NuScale 45 MWe reactor in the Alaskan market assumed 3 times the electrical energy output could be sold as process heat for $5.00 per million BTU [76]. Converting 1 million BTU to 293.07 kWh thermal power and selling the process heat at the same $5.00 rate per 293.07 kWh for 3 times the electrical energy output (15 MWth) yields an effective rate of $0.0512/kWh for process heat. This is well below the cost of electricity; even the most affordable market sells electricity for $0.10/kWe. At these rates, process heat may not be a feasible market for electricity, but this paradigm may change if there is a specific niche that can afford to pay more for process heat at a rate competitive with the cost of electricity.

The eVinci microreactor under development by Westinghouse Electric Company is very similar to the proposed microreactor; both are heat pipe monoblock microreactors operating at similar thermal power. While many design details and cost estimates are proprietary, eVinci is set to operate on a shorter 10-year cycle [10] and lower discharge burnup of about 30 MWd/kgU [12]. A direct comparison is made with eVinci, using the same set of assumptions for economics. Since details needed to estimate fuel costs are unknown, the breakeven cost for eVinci reported in is simply the net revenue from selling electricity discounted to present value.

Table 2-13. Estimate of eVinci breakeven budget, fuel and material costs unknown.

eVinci Net Revenues and Breakeven Budget									
COE $/kWh	$0.10	$0.15	$0.20	$0.25	$0.30	$0.35	$0.40	$0.45	$0.50
Income (month)	$346K	$520K	$694K	$867K	$1.04M	$1.21M	$1.39M	$1.56M	$1.73M
Interest	Reactor Breakeven Budget (Millions of $) (including fuel cost estimate of $32.2 M)								
0%	43.83	65.74	87.66	109.57	131.49	153.40	175.32	197.23	219.15
1%	41.29	61.93	82.58	103.22	123.87	144.51	165.16	185.80	206.45
2%	38.95	58.43	77.90	97.38	116.85	136.33	155.81	175.28	194.76

Table 2-13 continued									
3%	36.80	55.19	73.59	91.99	110.39	128.78	147.18	165.58	183.98
4%	34.80	52.21	69.61	87.01	104.41	121.82	139.22	156.62	174.02
5%	32.96	49.45	65.93	82.41	98.89	115.38	131.86	148.34	164.82
6%	31.26	46.89	62.52	78.15	93.78	109.41	125.05	140.68	156.31
7%	29.68	44.52	59.36	74.21	89.05	103.89	118.73	133.57	148.41
8%	28.22	42.32	56.43	70.54	84.65	98.76	112.87	126.97	141.08

Of course, it is unknown how much eVinci-like reactor will ultimately cost. But suppose the same pessimistic view is adopted again and eVinci will also cost $20,000/kWe capacity. At this price, eVinci's breakeven budget is also $100 M. Compared to the proposed reactor, eVinci has a tighter budget, despite operating for a shorter 10-year cycle and that favors the discount of revenue generated to present value. While crude, these economic estimates suggest a longer fuel cycle (10 years to 25 years) and higher discharge burnup (~30 MWd/kgU to ~62 MWd/kgU) is a favorable tradeoff and improves the economic competitiveness of microreactors, especially for low interest rates and low cost of electricity where margins are even tighter.

3 Conclusions

Fuel utilization improvements are achievable through metal hydride moderators and a moderating graphite monoblock + reflector. Yttrium hydride is the selected moderator due to its hydrogen stability at higher temperatures. The Advanced Moderator Module developed at Argonne is also an enabling technology, but the cost to bring this technology to market remains an open question. Higher moderation and fuel enrichment content leads to excess reactivity, which may prove a challenge to control or SCRAM the reactor.

Various technology improvements are proposed to improve the fuel utilization of a heat pipe and monoblock microreactor concept. The most comparable real-world reactor to this concept is the eVinci reactor under development by Westinghouse Electric Company. Both would operate at 15 MWth and 5 MWe. The discharge burnup is estimated around 30 MWd/kgU and a cycle length of 10 years for eVinci [10] [12], compared to the proposed reactor concept of about 62 MWd/kgU with a cycle length of 25 years. eVinci does have the advantage of a shorter cycle, and therefore earning its return on investment sooner. However, HALEU fuel costs may be the driving factor in the cost of a microreactor (e.g.: fuel cost for this reactor is over $32 M), and economic estimates suggest that increasing the discharge burnup at the expense of a longer cycle is a justified tradeoff.

4 Future Work

Many tradeoffs and studies were evaluated to improve the fuel cycle of the microreactor concept. Based on engineering judgement and safety concerns, not all options are pursued aggressively. For instance, the fuel-to-moderator mass ratio (see Fuel to Moderator Ratio) was deliberately kept quite low so that the reactor remains well undermoderated, a criticality safety feature. However, the findings of that study suggest expanding the moderator rods from a radius of 0.7125 cm to 0.8250 cm would confer great benefit to the fuel cycle while remaining *just barely* undermoderated. Another parameter that may be improved is the reflector thickness; graphite is cheap and doubling the reflector thickness from 30 cm to 60 cm would improve the discharge burnup by about 8 MWd/kgU, a significant improvement. The main arguments against expanding the reflector are the size and thermal limitations of heat pipes. One requirement set out for this concept development was small size: the microreactor must be small enough to be shipped by a flatbed truck to a remote location. Thickening the reflector would also increase the adiabatic length of the heat pipes, which would be detrimental to the capillary operating limit of the heat pipe (longer adiabatic length means the capillary forces driving liquid flow must transport coolant a further distance). Nonetheless, utilizing double ended heat pipes, like those used in eVinci, may improve heat pipe performance by up to a factor of 2 [14]. This approah was not undertaken in this thesis.

Therefore, there are still several improvements that warrant a closer investigation which would further push the fuel utilization and economic competitiveness of the microreactor concept. One final study has been conducted. In a “perfect world” scenario, all the proposed improvements are

pushed to their limits while still maintaining a safety margin. Suppose we live in a "perfect world". The question is how far could this concept go? describes the proposed design parameters, followed by the "perfect world" improvements that might be made. These changes have NOT been scrutinized to the same detail as the proposed design parameters, but offers a glimpse of what further improvements future work optimizing this design might yield.

Table 4-1. Comparison of proposed reactor parameters and idealized improvements for a "perfect world."

Parameter	Current	"Perfect World"	Comment
Moderator rod radius	0.7125 cm	0.8250 cm	Largest expansion possible whilst remaining on the cusp of undermoderated
Reflector thickness (axial and radial)	30 cm	60 cm	Diminishing returns as thickness increases, reactor must remain transportable
HP adiabatic length	30 cm	60 cm	Adiabatic length at minimum must be long enough to pass through the axial reflector
HP wick porosity	0.868	0.900 [62]	Improves thermal operating limits, which permits a higher operating power
HP sintered particle size (radius)	45 μm	27 μm	Particle size updated to balance out the change in porosity
Thermal power	15 MWth	20 MWth	Assumed HP with improved porosity increase margin on hotspots that permit increasing thermal power to 20 MWth
Conversion Efficiency	33.33%	40%	Higher temperatures might enable better efficiency

The following chart compares three different cycles. The "Real" or proposed cycle is the most realistic option which has accounted for thermal limits, reactivity control, reactivity safety feedback, and so on. The "Ideal" cycle is for the reactor configuration with all the above listed improvements if there was a "perfect world" (or enough engineering budget/manpower!). It should be noted that the "ideal" cycle is still somewhat grounded in reality as discussed above. For

instance, the reactor *should* still be undermoderated (albeit barely), the improved heat pipe limits *should* permit a higher operating power, and so on.

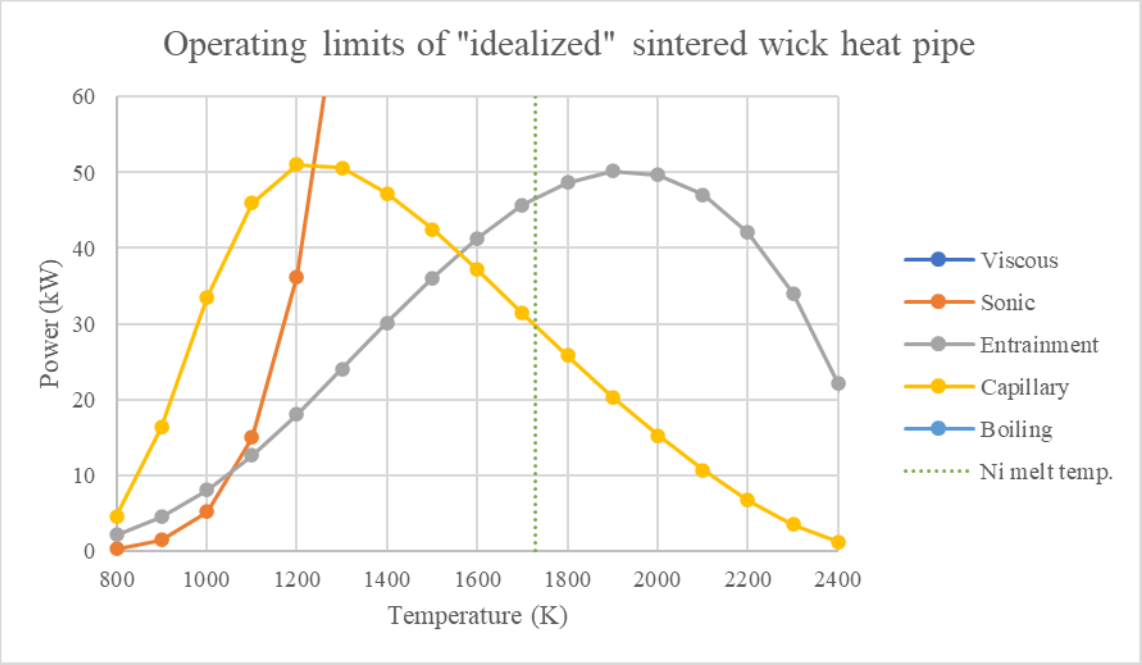

Figure 4-1. Improved thermal operating limits of the "perfect" reactor.

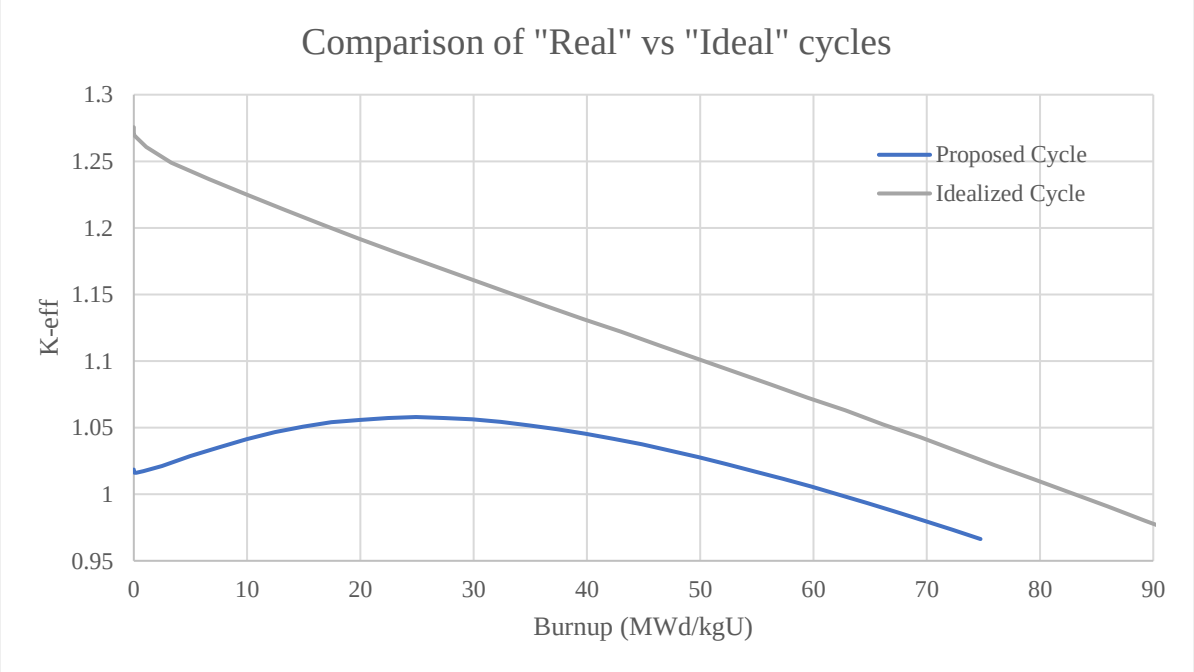

Figure 4-2. Cycle burnup of the real vs. ideal reactor.

Compared to the realistic reactor, the idealized reactor improves the discharge burnup from 62.1 MWd/kgU to 83.0 MWd/kgU. In both cases, the cycle length stayed relatively constant at about 25 years, whilst the ideal reactor operated at a higher thermal power. Undertaking the same simplistic economic estimates of the breakeven cost for the idealized reactor shows:

Table 4-2. Breakeven budget of the idealized microreactor with fuel and material costs accounted for.

Monthly income for a given Cost of Electricity for the Idealized Reactor									
COE $/kWh	$0.10	$0.15	$0.20	$0.25	$0.30	$0.35	$0.40	$0.45	$0.50
Income (month)	$346K	$520K	$694K	$867K	$1.04M	$1.21M	$1.39M	$1.56M	$1.73M
Interest	Reactor Breakeven Budget (Millions of $) (including fuel cost estimate of $32.2 M)								
0%	134.35	217.63	300.91	384.18	467.46	550.74	634.01	717.29	800.57
1%	113.73	186.70	259.67	332.63	405.60	478.57	551.53	624.50	697.47
2%	96.48	160.82	225.16	289.50	353.85	418.19	482.53	546.87	611.21
3%	81.97	139.05	196.14	253.22	310.31	367.40	424.48	481.57	538.65
4%	69.69	120.64	171.59	222.54	273.48	324.43	375.38	426.33	477.28
5%	59.25	104.98	150.71	196.44	242.17	287.89	333.62	379.35	425.08
6%	50.33	91.59	132.86	174.12	215.39	256.65	297.92	339.18	380.45
7%	42.66	80.09	117.51	154.94	192.37	229.80	267.23	304.66	342.09
8%	36.03	70.14	104.26	138.37	172.49	206.60	240.72	274.83	308.95

The assumptions regarding the idealized reactor are overgenerous, but not altogether unreasonable. The ideal reactor suggests there is still much room for improvements, making a tantalizing case for the economic competitiveness for microreactors with more optimization and engineering effort. Another study could be conducted to calculate the breakeven period or payback period for the reactor at a given cost of electricity, lending another dimension to the economic considerations of a particular design.

In this thesis, control sliders were selected over control drums or control rods. Control sliders are similar to control drums in that they both act on the periphery of the core and are embedded in

the radial reflector, but control sliders are closer to the core and therefore better neutronically coupled, resulting in a higher reactivity worth. However, due to heat pipe capillary pumping considerations (insufficient pumping action against gravity), the reactor must be oriented with its axis parallel to the ground. This complicates the use of control sliders considerably. The grooved slots required to give sliders access to the core means a slider on the underside of the core could simply fall out of its slot and the sliders above the core might fall in. Mechanisms to move the sliders themselves, such as a rail lining the inside of the slider grooves, would need to be resilient to high temperatures and neutron flux. Since the sliders and grooves are straight, rectangular slabs/channels, any warping or buckling of either (perhaps due to thermal cycling, neutron flux, or mechanical damage) could cause damage that prevents the insertion or withdrawal of the sliders. Control rods were rejected primarily since the axial space outside the core would be occupied by heat pipes and a heat conversion system. However, since the heat pipes are single-ended and the reactor lies flat, control rods might be inserted from the opposite side that heat pipes terminate. However, control rods would require some redesign of the fuel lattice of the active core and so this solution was not pursued here. Finally, the proposed core cycle length is 25 years. The control sliders are 5 cm thick boron-carbide slabs enriched to 100% B-10; at the beginning of cycle, they are certainly opaque to neutrons and would perform as analyzed. However, over the length of the cycle, the boron content will steadily deplete, reducing the efficacy of the sliders, and a significant amount of helium buildup would occur. Internal pressure or cracking from helium buildup is another alarming cause for concern and must be accounted for in the design. Further work is recommended to thoroughly analyze and compare control sliders against control drums, particularly mechanical and thermal considerations which were not assessed here.

Additionally, the expansion of the core lattice was necessary to accommodate larger heat pipes to meet thermal limits, but consequently also reduced the effectiveness of the external control sliders. If the core lattice pitch could be tightened, it would restore some efficacy of the control sliders. This might be achieved by designing a more effective heat pipe, such as a double-ended pipe or improved wick. The size of fuel and moderator rods do not occupy the entire lattice pitch, and since no heat pipes are directly adjacent to another, the lattice pitch could be reduced by allowing heat pipes to overlap into the extra spacing of neighboring fuel and moderator rods.

Emergency shutdown of this reactor may also prove problematic, particularly the instability at low temperatures and apparent positive moderator reactivity coefficient. Based on the BOC reactivity worth of the control rod insertion, it is not clear if the shutdown rod would be sufficient to provide enough reactivity change to shutdown the reactor at its maximum reactivity in the cycle. It was noted the neutron flux distribution is highly depressed in the center of the core at BOC due to the presence of GdN-loaded rods at the center of the core. The flux distribution would be more centrally peaked at max reactivity which would increase the reactivity worth of the core; but this must be rigorously verified. One “simple” fix might be increasing the size of the shutdown rod channel and shutdown rod itself such that it would provide enough reactivity worth even with the positive moderator coefficient. Another possibility is the use of resonance absorbers in fuel (such as erbia) to absorb neutrons at the thermal energy peak, but would incur a residual penalty to reactivity and discharge burnup [18].

Another aspect of criticality safety that requires more investigating are reactivity feedback coefficients. At present, only an isothermal temperature reactivity coefficient over the full core at beginning of cycle was investigated. Since YH_2 is expected to have a positive moderator coefficient [53], it will be important to verify the remaining reactivity coefficients are sufficiently

negative for criticality safety. These would include fuel, graphite, and coolant reactivity temperature coefficients. Since the core is designed as a solid monoblock with solid fuel, there are no liquids or gases (aside from sodium coolant contained in fixed-volume heat pipes); thermal expansion will also be important rather than a void coefficient seen in conventional water-cooled reactors.

Appendix

A. Main Reactor Parameters

Table A-1. Parameters of the reactor core.

Reactor Core Main Parameters		
Item	**Value**	**Comment**
Active core diameter	150 cm	
Active core height	150 cm	
Fuel rod radius	0.7115 cm	
Total number fuel rods	708 uranium nitride (UN)	
Moderator rod radius	0.7125 cm	
Total number mod. Rods	1404 yttrium hydride (YH_2)	
Heat pipe outer radius	0.9600 cm	
Total number heat pipes	1224	
Enrichment	19.75% U-235 99.99% N-15	All nitrogen-containing materials at 99.99% ^{15}N
Radial reflector thickness	30 cm	
Axial reflector thickness	30 cm	
Core lattice pitch	2.020 cm	
Reactor thermal power	15 MWth	
Reactor electric power	5 MWe	Assumed 33% conversion efficiency
Average discharge burnup	~60 MWd/kgU	
Nominal cycle length	25 years	
Fuel cladding material	0.05 mm Silicon Carbide (SiC)	
Moderator cladding	0.01 mm Niobium substrate, 0.04 mm SiC	Based on ANL Advanced Moderator Module
Burnable absorber coating	BN	100% enriched ^{10}B
Burnable absorber fuel mixing	Gadolinium nitride (GdN) UN composite	Natural gadolinium in 11% of fuel rods
Control sliders	5 cm thick Boron Carbide (B_4C) slabs	100% enriched ^{10}B
Shutdown control rod	24 cm diameter B_4C rod	100% enriched ^{10}B

Table A-2. Parameters of the heat pipe design.

Heat Pipe Main Parameters		
Item	**Value**	**Comment**
Outer diameter	1.920 cm	
Inner diameter	1.800 cm	
Wick thickness	0.3250 cm	
Vapor core radius	0.5750 cm	
Coolant	Sodium metal	
Wick type	Sintered nickel metal powder	
Wick porosity	0.868	
Sintered powder size (radius)	45 microns	
Calculated permeability	2.03E-09 m^2	
Nickel melting temperature	1728 K	
Evaporator length	150 cm	Height of the active core
Adiabatic length	30 cm	Axial reflector thickness
Condenser length	60 cm	
Inclination angle	0 degrees	Horizontal/flat
Operating temperature range	~1400 K to 1500 K	Cannot exceed 1528 K for conservative treatment of heat pipe failure

B. Full Core Power Distribution Plots

The distribution of fission power production in each fuel pin for each depletion step in the cycle is shown in the following figures. Take note how the gadolinium-loaded fuel pins are “cold” initially, but produce more power later in the cycle as GdN burns away.

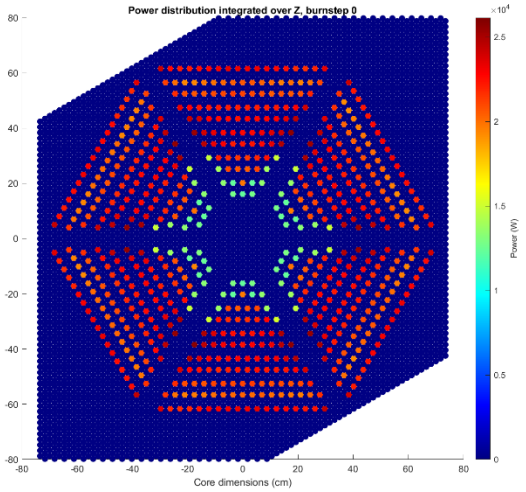
Power distribution integrated over Z, burnstep 0
Core dimensions (cm)
Power (W)
×10^4

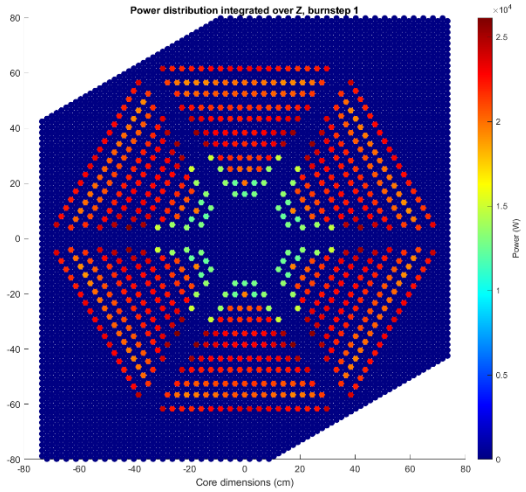
Power distribution integrated over Z, burnstep 1
Core dimensions (cm)
Power (W)
×10^4

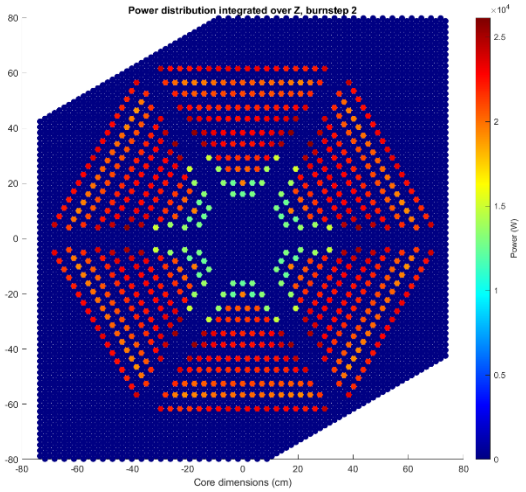
Power distribution integrated over Z, burnstep 2
Core dimensions (cm)
Power (W)
×10^4

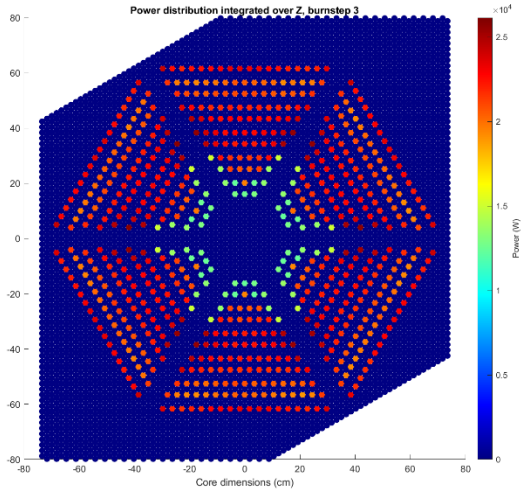
Power distribution integrated over Z, burnstep 3
Core dimensions (cm)
Power (W)
×10^4

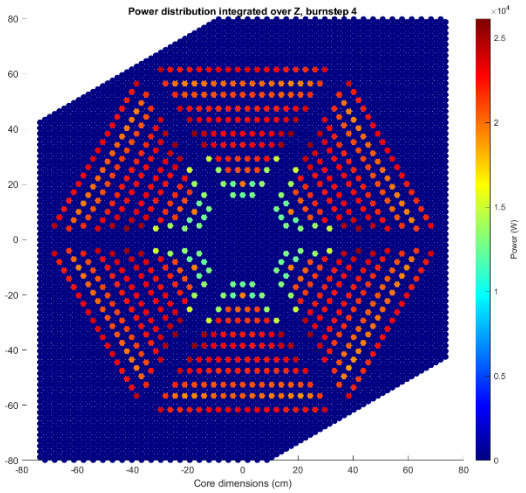
Power distribution integrated over Z, burnstep 4
Core dimensions (cm)
Power (W)
×10^4

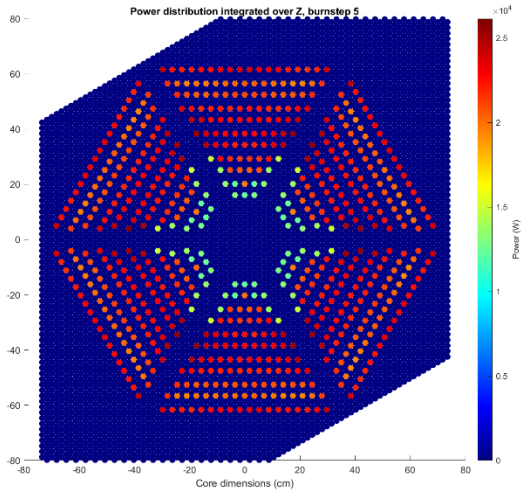
Power distribution integrated over Z, burnstep 5
Core dimensions (cm)
Power (W)
×10^4

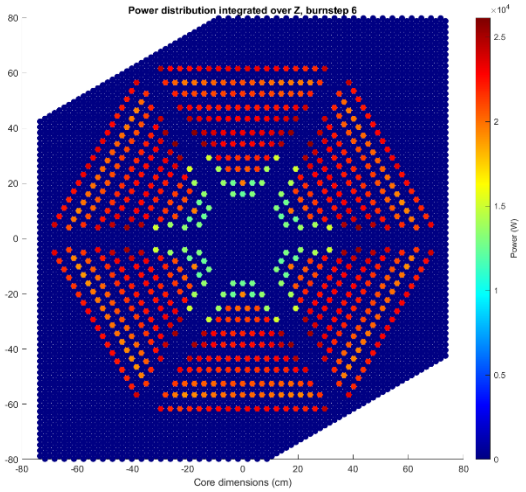
Power distribution integrated over Z, burnstep 6
Core dimensions (cm)
Power (W)
×10^4

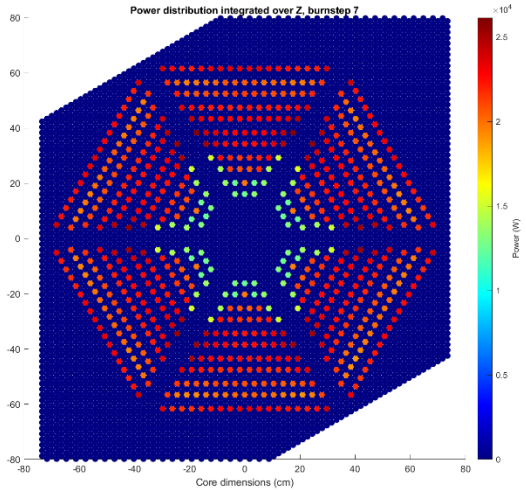
Power distribution integrated over Z, burnstep 7
Core dimensions (cm)
Power (W)
×10^4

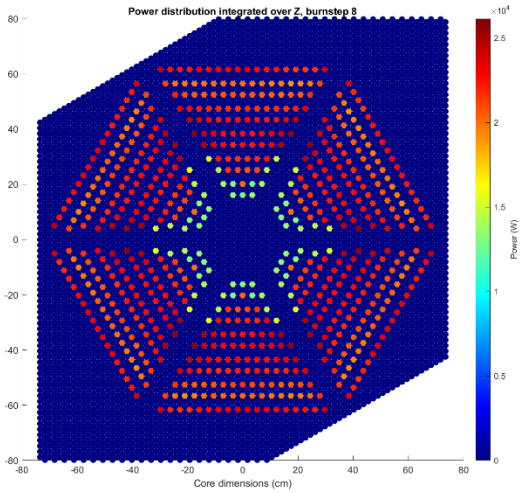
Power distribution integrated over Z, burnstep 8
Core dimensions (cm)
Power (W)
×10^4

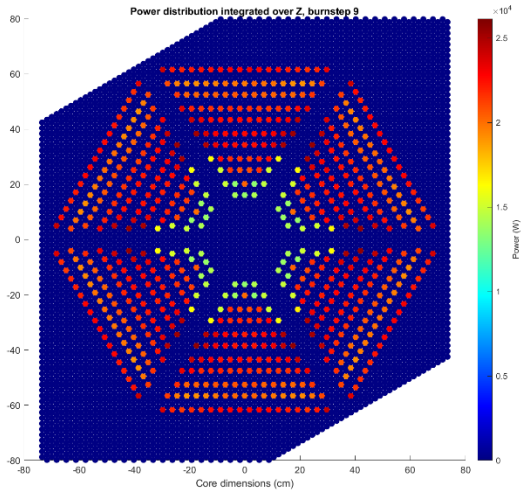
Power distribution integrated over Z, burnstep 9
Core dimensions (cm)
Power (W)
×10^4

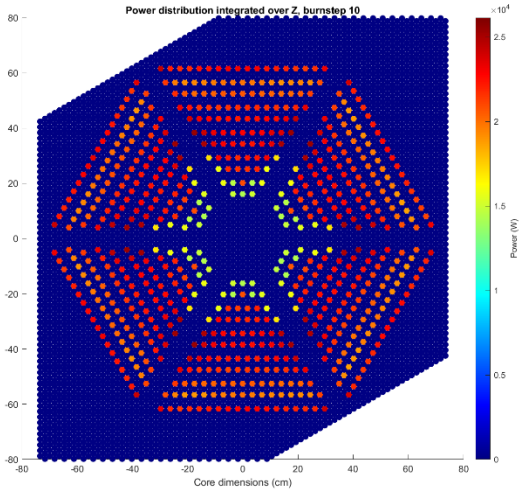
Power distribution integrated over Z, burnstep 10
Core dimensions (cm)
Power (W)
×10^4

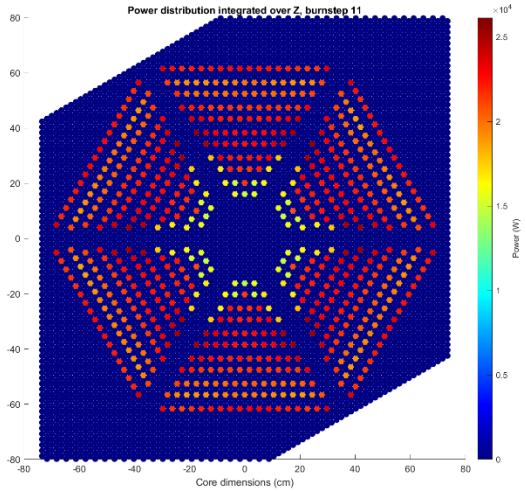
Power distribution integrated over Z, burnstep 11
Core dimensions (cm)
Power (W)
×10^4

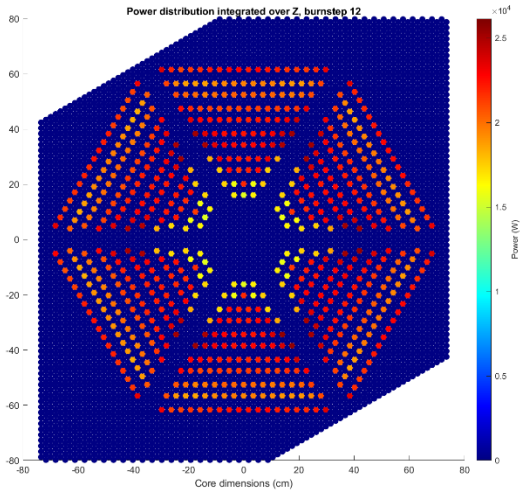
Power distribution integrated over Z, burnstep 12
Core dimensions (cm)
Power (W)
×10^4

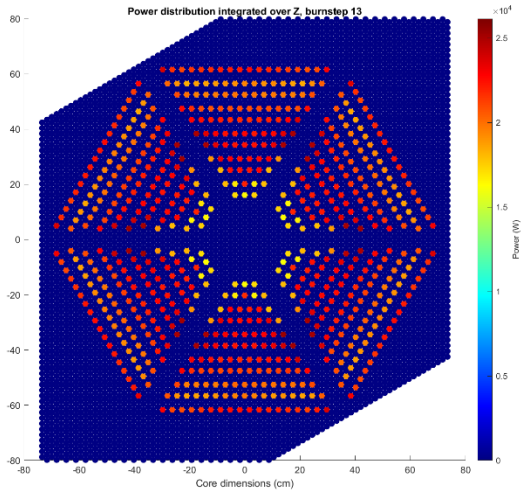
Power distribution integrated over Z, burnstep 13
Core dimensions (cm)
Power (W)
×10^4

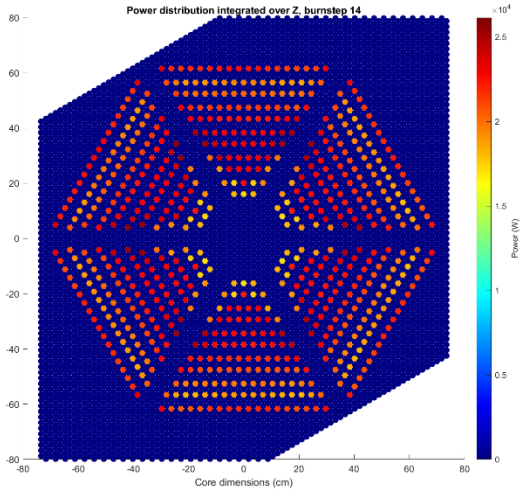
Power distribution integrated over Z, burnstep 14
Core dimensions (cm)
Power (W)
×10^4

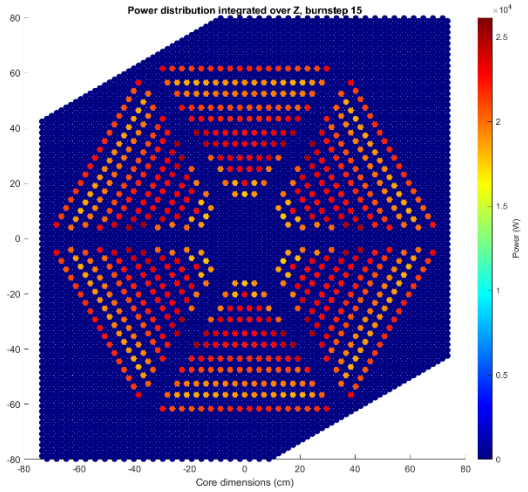
Power distribution integrated over Z, burnstep 15
Core dimensions (cm)
Power (W)
×10^4

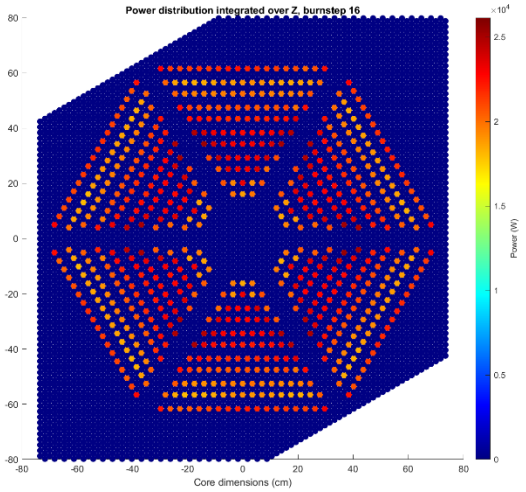
Power distribution integrated over Z, burnstep 16
Core dimensions (cm)
Power (W)
×10^4

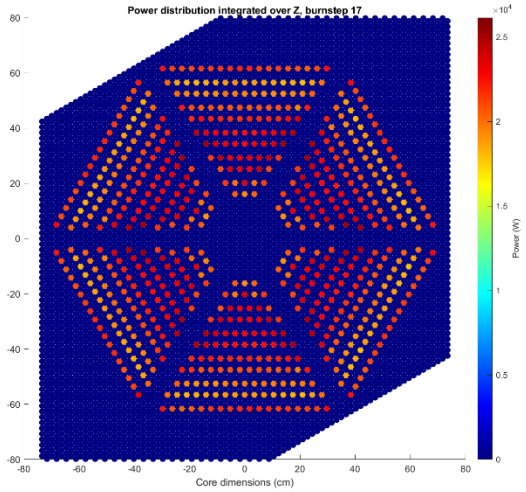
Power distribution integrated over Z, burnstep 17
Core dimensions (cm)
Power (W)
×10^4

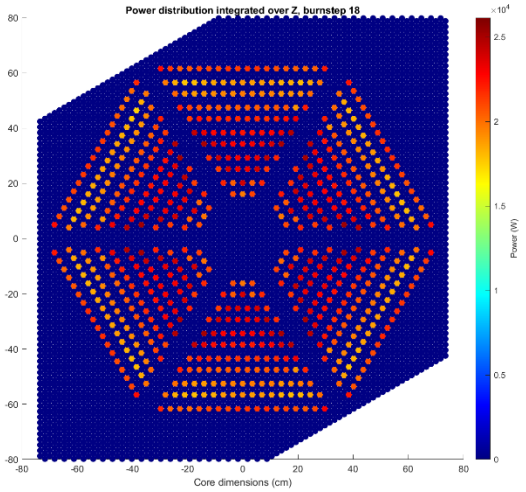
Power distribution integrated over Z, burnstep 18
Core dimensions (cm)
Power (W)
×10^4

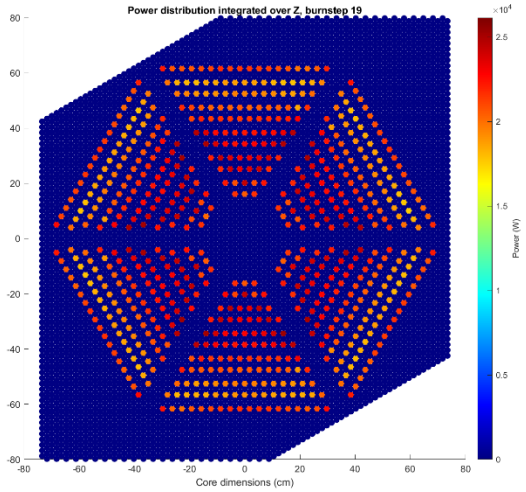
Power distribution integrated over Z, burnstep 19
Core dimensions (cm)
Power (W)
×10^4

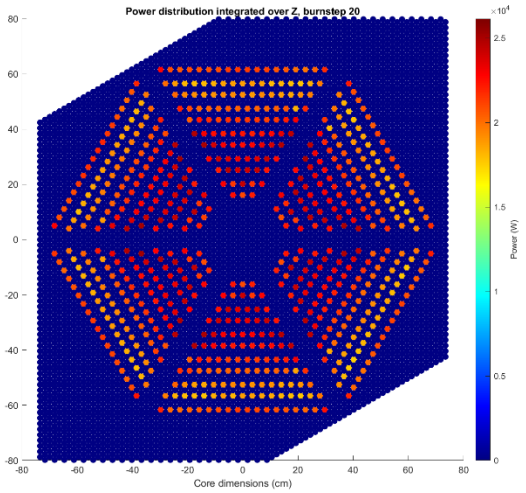
Power distribution integrated over Z, burnstep 20
Core dimensions (cm)
Power (W)

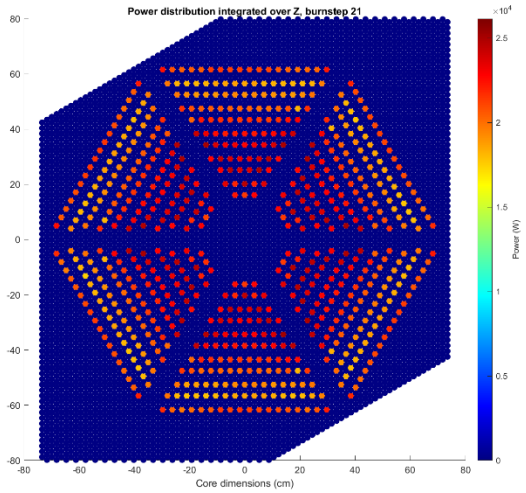
Power distribution integrated over Z, burnstep 21
Core dimensions (cm)
Power (W)

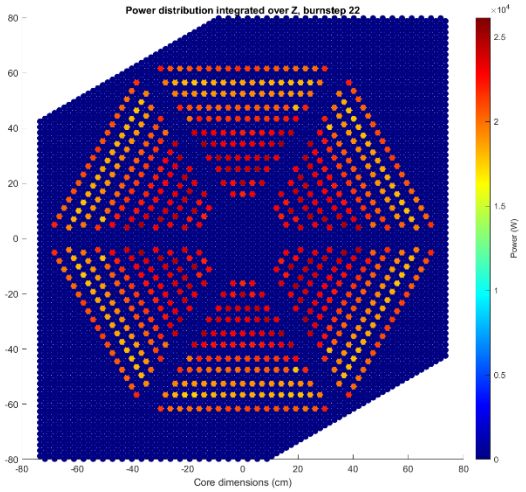
Power distribution integrated over Z, burnstep 22
Core dimensions (cm)
Power (W)

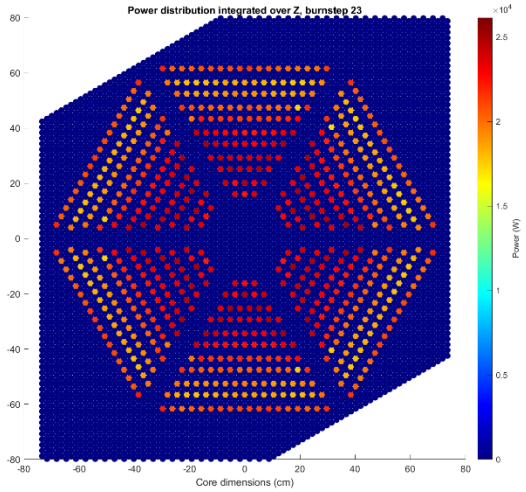
Power distribution integrated over Z, burnstep 23
Core dimensions (cm)
Power (W)

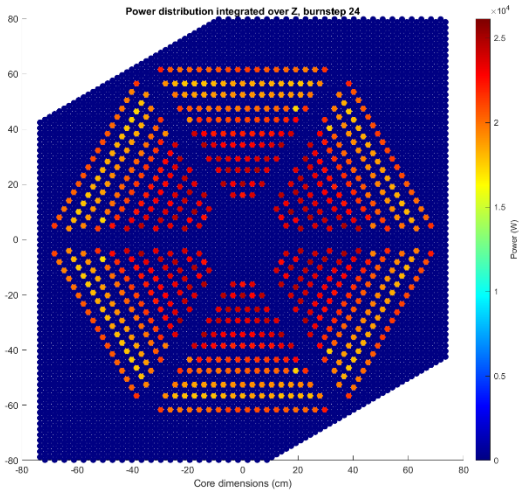
Power distribution integrated over Z, burnstep 24
Core dimensions (cm)
Power (W)

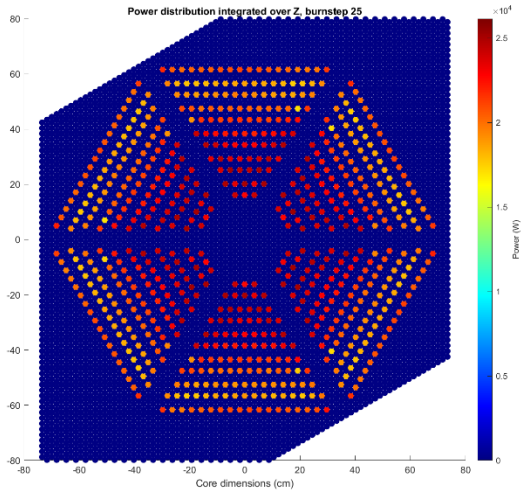
Power distribution integrated over Z, burnstep 25
Core dimensions (cm)
Power (W)

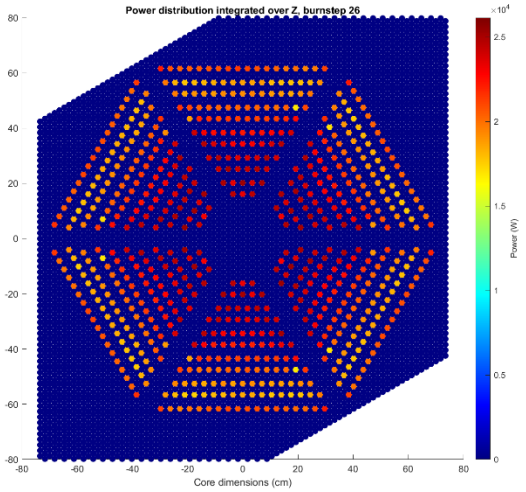
Power distribution integrated over Z, burnstep 26
Core dimensions (cm)
Power (W)

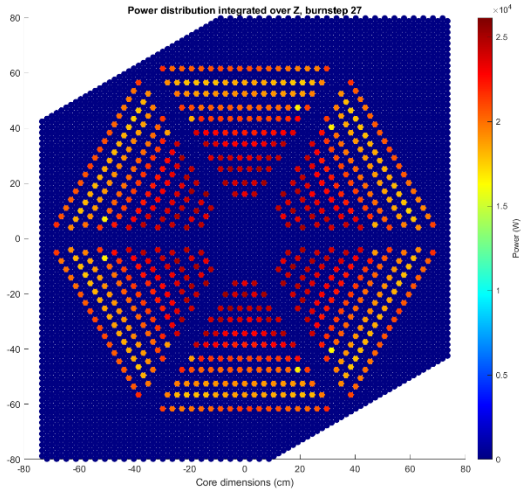
Power distribution integrated over Z, burnstep 27
Core dimensions (cm)
Power (W)

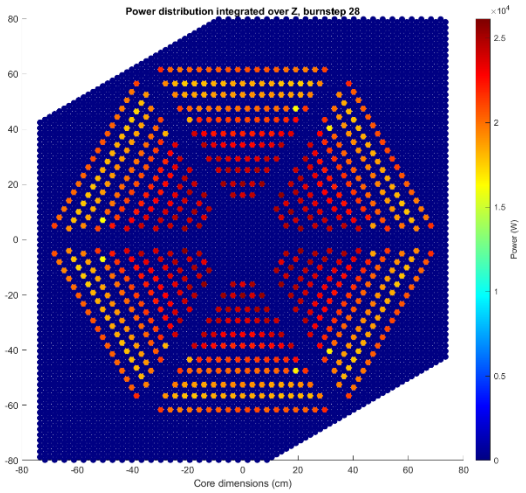
Power distribution integrated over Z, burnstep 28
Core dimensions (cm)
Power (W)
×10^4

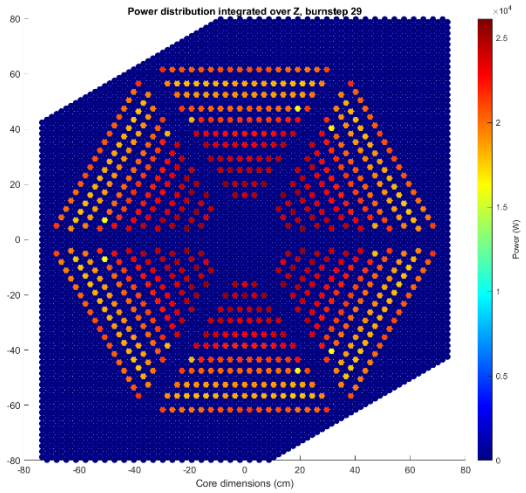
Power distribution integrated over Z, burnstep 29
Core dimensions (cm)
Power (W)
×10^4

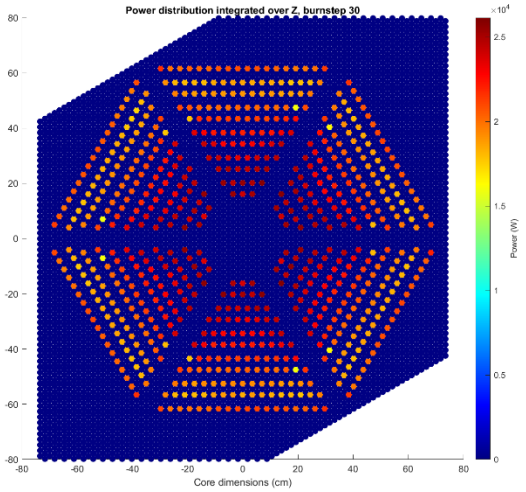
Power distribution integrated over Z, burnstep 30
Core dimensions (cm)
Power (W)
×10^4

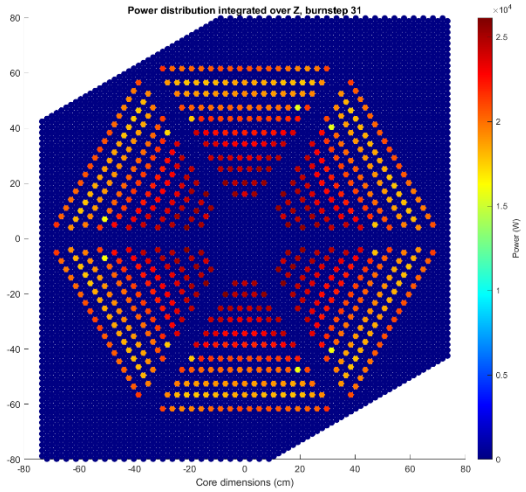
Power distribution integrated over Z, burnstep 31
Core dimensions (cm)
Power (W)
×10^4

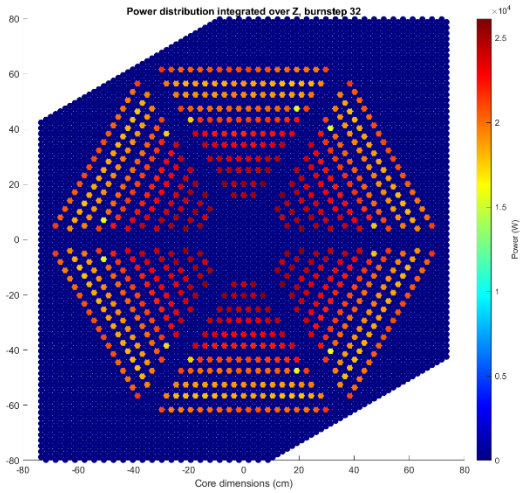

C. Material Properties

All thermophysical properties of sodium liquid and vapor except for the vapor dynamic viscosity was based on the Fink and Leibowitz's report produced at Argonne National Laboratory (report number ANL/RE-95/2) [77]. The dynamic viscosity of sodium vapor was not available in this report and was instead sourced from Golden and Tokar's review of sodium properties (report number ANL-7323) [78]. The properties of sodium used for heat pipe operational limit calculations are reproduced below. Values highlighted in yellow are interpolated linearly between given data points. Values highlighted in red are extrapolated values using either a linear or power law data fit, depending on which type of fit best matches the provided data points.

Table A-3. Thermophysical properties of sodium coolant.

Thermophysical properties of sodium					
Temp (K)	Enthalpy of vaporization (kJ/kg)	Liquid density (kg/m^3)	Vapor density (kg/m^3)	Saturated Vapor Pressure (Pa)	Saturated Vapor Pressure (atm)
371	4532	925.38	9.84E-10	1.422E-04	1.41E-09

Table A-3 continued					
400	4510	919	1.24E-09	1.800E-04	1.78E-09
500	4435	897	5.03E-07	8.990E-02	8.87E-07
600	4358	874	2.63E-05	5.570E+00	5.49E-05
700	4279	852	4.31E-04	1.050E+02	1.04E-03
800	4197	828	3.43E-03	9.410E+02	9.28E-03
900	4112	805	1.70E-02	5.147E+03	5.08E-02
1000	4025	781	6.03E-02	1.995E+04	1.97E-01
1100	3933	756	1.68E-01	6.016E+04	5.94E-01
1200	3838	732	3.94E-01	1.504E+05	1.49E+00
1300	3738	706	8.05E-01	3.257E+05	3.21E+00
1400	3633	680	1.48E+00	6.398E+05	6.22E+00
1500	3523	653	2.50E+00	1.113E+06	1.10E+01
1600	3405	626	3.96E+00	1.828E+06	1.80E+01
1700	3279	597	5.95E+00	2.828E+06	2.79E+01
1800	3143	568	8.54E+00	4.610E+06	4.11E+01
1900	2994	537	1.19E+01	5.870E+06	5.78E+01
2000	2829	504	1.60E+01	7.991E+06	7.89E+01
2100	2640	469	2.12E+01	1.055E+07	1.04E+02
2200	2418	431	2.77E+01	1.357E+07	1.34E+02
2300	2141	387	3.63E+01	1.706E+07	1.64E+01
2400	1747	335	4.93E+01	2.103E+07	2.08E+02
2469	991	269	8.57E+01	2.409E+07	2.37E+02
2500	652	239	1.02E+02	2.547E+07	2.51E+02
2503.7	0	219	2.19E+02	2.564E+07	2.53E+02
Temp (K)	Liquid Heat Capacity at const P, Cp (kJ/kg*K)	Liquid Heat Capacity at const. V, Cv (kg/kg*K)	Liquid ratio of spec heats (Cv/Cp)	Vapor Heat Capacity at const P, Cp (kJ/kg*K)	Vapor Heat Capacity at const V, Cv (kJ/kg*K)
371	1.383	1.262	1.096	0.747	0.389
400	1.372	1.241	1.106	0.860	0.490
500	1.334	1.170	1.140	1.250	0.840
600	1.301	1.104	1.178	1.800	1.310
700	1.277	1.045	1.222	2.280	1.710
800	1.260	0.994	1.268	2.590	1.930
900	1.252	0.951	1.317	2.720	1.980
1000	1.252	0.914	1.370	2.700	1.920
1100	1.261	0.885	1.425	2.620	1.810
1200	1.279	0.862	1.484	2.510	1.680
1300	1.305	0.844	1.546	2.430	1.580
1400	1.340	0.830	1.614	2.390	1.510
1500	1.384	0.819	1.690	2.360	1.440

Table A-3 continued

1600	1.437	0.811	1.772	2.340	1.390
1700	1.500	0.803	1.868	2.410	1.380
1800	1.574	0.795	1.980	2.460	1.360
1900	1.661	0.784	2.119	2.530	1.330
2000	1.764	0.768	2.297	2.660	1.300
2100	1.926	0.768	2.508	2.910	1.300
2200	2.190	0.791	2.769	3.400	1.340
2300	2.690	0.872	3.085	4.470	1.440
2400	4.012	1.172	3.423	8.030	1.760
2469	8.274	2.463	3.359	290.240	12.296
2500	36.279	16.371	2.216	417.030	17.030
2503.7	39.622	18.031	2.197	432.163	17.595
Temp (K)	Vapor ratio of spec heats (Cv/Cp)	Surface energy or Surface tension (N/m)	Liquid Dynamic Viscosity (Pa*s)	Vapor Dynamic Viscosity (Pa*s)	Liquid Thermal Conductivity (W/mK)
371	1.923	0.2007	6.88E-04	1.487E-05	89.44
400	1.755	0.1977	5.99E-04	1.504E-05	87.22
500	1.488	0.1871	4.15E-04	1.565E-05	80.09
600	1.374	0.1766	3.21E-04	1.626E-05	73.70
700	1.333	0.1662	2.64E-04	1.690E-05	68.00
800	1.342	0.1559	2.27E-04	1.748E-05	62.90
900	1.374	0.1456	2.01E-04	1.809E-05	58.34
1000	1.406	0.1354	1.81E-04	1.869E-05	54.24
1100	1.448	0.1253	1.66E-04	1.930E-05	50.54
1200	1.494	0.1153	1.53E-04	1.991E-05	47.16
1300	1.538	0.1054	1.43E-04	2.052E-05	44.03
1400	1.583	0.0956	1.35E-04	2.113E-05	41.08
1500	1.639	0.0859	1.28E-04	2.170E-05	38.24
1600	1.683	0.0763	1.22E-04	1.960E-05	35.44
1700	1.746	0.0669	1.17E-04	2.020E-05	32.61
1800	1.809	0.0576	1.12E-04	2.080E-05	29.68
1900	1.902	0.0485	1.08E-04	2.140E-05	26.57
2000	2.046	0.0395	1.04E-04	2.200E-05	23.21
2100	2.238	0.0308	1.01E-04	2.260E-05	19.54
2200	2.537	0.0224	9.80E-05	2.320E-05	15.48
2300	3.104	0.0143	9.50E-05	2.380E-05	10.97
2400	4.563	0.0067	9.20E-05	2.440E-05	5.92
2469	18.311	0.0022	8.00925E-05	2.481E-05	2.02
2500	24.488	0.0002	7.90786E-05	2.500E-05	0.27
2503.7	24.562	0	7.89593E-05	2.502E-05	0.05

Thermal conductivity (in W/m-K) of pure metals with respect to temperature is provided in a review by Abu-Eishah (in W/m-K) as a multiple linear regression model [79]. The fitting equation is:

$$k = aT^b e^{cT} e^{\frac{d}{T}}$$

For molybdenum, the fitting constants were given as:

- $a = 84.1335$
- $b = 0.065655$
- $c = -2.24456 * 10^{-4}$
- $d = 50.99060$

and was found valid in the temperature range from 50 to 2800 K. The R^2 value for this fit was 0.9933.

For nickel, the fitting constants were given as:

- $a = 1001.544$
- $b = -0.493261$
- $c = 7.220 * 10^{-4}$
- $d = 39.46008$

and is valid in the temperature range from 30 K to 1500 K. Nickel melts at 1728 K. In this analysis, the thermal conductivity is extrapolated out using this linear regression model to 1700 K when computing the boiling limit for a sintered nickel wick. Since the boiling limit is rare and usually not a concern for liquid metal heat pipes, this extrapolation is not expected to be problematic, but could warrant a closer investigation in future work.

D. S(α,β) Testing (ENDF/B-VIII.0 update)

Neutron thermal scattering data, S(α,β), is important for any system with moderators. ENDF/B-VIII.0 included evaluations for important materials like yttrium hydride and uranium nitride that were hitherto unavailable [31]. Serpent natively has only included data up to ENDF/B-VI [80], and only recently has Serpent (in version /2.1.32) been able to process and use data in continuous energy format made available from ENDF/B-VII onwards. Data files for ENDF/B-VIII.0 were downloaded from Los Alamos National Lab's nuclear data website in ACE library format [81]. A limited scope comparison study was performed for thermal scattering data from ENDF/B-VIII.0 between MCNP6.2 [82] and Serpent 2.1.32 [32]. Both codes were used to test S(α,β) data in an identical geometry consisting of an infinite square lattice of 0.8150 cm diameter UO_2 (or UN for the case with UN S(α,β) data) with a lattice pitch of 1 cm. The space between fuel pins is filled with the moderator material being tested. Fuel material was set to 900 K and moderator material to 600 K (if data available). Graphite was tested with a 21.2 cm pitch and 2.80 cm diameter natural uranium metal fuel due to the low moderating ratio of graphite. Only one temperature was tested with the expectation that any major differences generated by both codes would be apparent regardless of which temperature cross sections were used. Both ENDF/B-VII and VIII S(α,β) data were tested. Most comparisons were made with 2500 neutrons per generation, 20 skipped generations, and 200 active generations, with some materials re-tested to lower uncertainty if results did not seem conclusive (indicated). At these run parameters, the uncertainties are on the order of ~100 pcm. New materials added in VIII and not present in VII are indicated with blank columns. The root mean square of the variances indicates the level of agreement of the results between different tests; a value of 0 indicates perfect agreement (which would be suspicious anyhow).

The first column is the material tested. The second and third columns are the material designations in ENDF/B-VII.1 and ENDF/B-VIII.0 respectively for the element in question. For instance, “o-beo” indicates oxygen in beryllium oxide (BeO), “be-beo” indicates beryllium in BeO, and “be-beo + o-beo” indicates both were used. The following columns report the differences in the generated K-eff calculations and are color-coded according to how closely each comparison appeared to agree. These columns are organized in sets of 3: the first is the RMS of the variance, the second is the absolute difference in K-eff calculated for each material, and the last is the absolute difference divided by the RMS. A value less than 5 in this column is treated as good agreement and any values greater than 5 indicate some differences either in the codes or data files and must be treated with caution.

Most materials indicate good agreement between the two codes and between ENDF/B-VII.1 and ENDF/B-VIII.0. Comparisons between B-VII.0 and B-VIII.1 evaluations with the same code (MCNP to MCNP, Serpent to Serpent) are mostly consistent, with the major outlier being uranium in UO_2 and uranium in UN (see below). The results for silicon carbide do not indicate very good or very poor agreement. Since silicon carbide in the concept microreactor exists as a 0.4 mm or 0.5 mm layer on moderator and fuel pins, it was decided to cautiously include silicon carbide $S(\alpha,\beta)$ since the impact is expected to be minimal anyway. Some further testing may be warranted, however.

There is a known issue/bug* in MCNP6.2 in that the code cannot handle the isotopes U-233 or U-235 for thermal scattering. This issue is set to be fixed in the future release of MCNP6.3. A possible workaround is manually replacing “92233” and “92235” with “0” and adding blank delimiters to conserve the column format. However, Serpent also appears to have problems using uranium thermal scattering data from B-VIII.0 and the cause is not known. Uranium thermal

scattering is expected to, at most, have an impact in the hundreds of pcm on K-eff and so for the work done in this thesis, all simulations do not include thermal scattering data for any uranium-containing materials.

*Note: from communications from the MCNP team in the MCNP users' mailing list.

A note on thermal scattering data temperatures: Serpent is unable to interpolate temperatures for S(α,β) cross section data in continuous energy format (ENDF/B-VII and later). Since S(α,β) data for yttrium hydride is used and only available from ENDF/B-VIII.0, temperature cannot be interpolated for yttrium hydride. There exists discrete energy format S(α,β) data for graphite from ENDF/B-VI that could be interpolated to proper temperatures, but for consistency, all cross sections used are from the ENDF/B-VIII.0 evaluation with no temperature interpolation. For temperatures which there does not exist a data file at that temperature, the next closest or highest temperature is selected. Ex: graphite at 296 K is selected for 300K. For yttrium hydride, data files for 800 K and 1000 K exist but not 900 K, so 1000 K is selected to use instead.

Table A-4. Thermal scattering data validity and comparison between MCNP vs. Serpent and ENDF/B-VII.1 vs ENDF/B-VII

Material	**B-VII.0 designation**	**B-VIII.1 designation**	**MCNP B-VII.1 vs. MCNP B-VIII.0**			**Serpent B-VII.1 vs. Serpent B-VIII.0**		
			RMS Var.	**Abs. Diff.**	**AD/RMSV**	**RMS Var.**	**Abs. Diff.**	**AD/RMSV**
Light water	lwtr	h-h2o	0.001332	0.00453	3.4	0.001591	0.00184	1.2
ZrH_2	h-zr	h-zrh	0.000969	0.0029	3.0	0.000707	0.00068	1.0
	zr-h	zr-zrh	0.000979	0.00295	3.0	0.000722	0.00072	1.0
	h-zr + zr-h	h-zrh + zr-zrh	0.000905	0.00091	1.0	0.000742	0.00206	2.8
Be	be	be-met	0.001492	0.00548	3.7	0.00145	0.00163	1.1
BeO	be-o	be-beo	0.001513	0.00496	3.3	0.001308	0.00105	0.8
	o-be	o-beo	0.001457	0.00374	2.6	0.00145	0.00378	2.6
	be-o + o-be	be-beo + o-beo	0.001329	0.00164	1.2	0.001492	0.00114	0.8
Graphite	grph	grph	0.001096	0.00493	4.5	0.001501	0.00215	1.4
PE	poly	h-poly	0.001766	0.00527	3.0	0.001485	0.00193	1.3
UO_2	u-o2	u-uo2	0.001046	0.12005	114.7	0.00136	0.06286	46.2
	o2-u	o-uo2	0.00094	0.00429	4.6	0.001544	0.05895	38.2
	u-o2 + o2-u	u-uo2 + o-uo2	0.00121	0.11818	97.7	0.001376	0.06224	45.2
			MCNP B-VII.1 vs. Serpent B-VII.1			**MCNP B-VIII.0 vs. Serpent B-VIII.0**		
			RMS Var.	**Abs. Diff.**	**AD/RMSV**	**RMS Var.**	**Abs. Diff.**	**AD/RMSV**
Light water	lwtr	h-h2o	0.001494	0.00303	2.0	0.00144	0.00334	2.3
ZrH_2	h-zr	h-zrh	0.00086	0.00163	1.9	0.000836	0.00195	2.3
	zr-h	zr-zrh	0.000924	0.0054	5.8	0.000792	0.00317	4.0
	h-zr + zr-h	h-zrh + zr-zrh	0.000817	6E-05	0.1	0.000839	0.00121	1.4
Be	be	be-met	0.001465	0.00052	0.4	0.001478	0.00333	2.3
BeO	be-o	be-beo	0.00141	0.00081	0.6	0.001419	0.0052	3.7
	o-be	o-beo	0.001443	0.00087	0.6	0.001443	0.00311	2.2
	be-o + o-be	be-beo + o-beo	0.001394	0.00117	0.8	0.001513	0.00684	4.5
PE	poly	h-poly	0.001259	0.00227	1.8	0.001934	0.00107	0.6
UO_2	u-o2	u-uo2	0.00111	0.00028	0.3	0.001309	0.18319	140.0
	o2-u	o-uo2	0.001317	0.00153	1.2	0.001239	0.06477	52.3
	u-o2 + o2-u	u-uo2 + o-uo2	0.00137	0.00241	1.8	0.001217	0.18283	150.2
YH_2		h-yh2	N/A	N/A	N/A	0.001521	0.0018	1.2

	Not available in B-VII.0	y-yh2	N/A	N/A	N/A	0.001676	0.00293	1.7
		h-yh2 + y-yh2	N/A	N/A	N/A	0.0016	0.00167	1.0
Graphite (10/30% porosity)	10/30% porosity not available in B-VII.0	grph	0.001181	0.0004	0.3	0.001322	0.00848	6.4
		grph10	N/A	N/A	N/A	0.001414	0.00272	1.9
		grph30	N/A	N/A	N/A	0.001365	0.00547	4.0
UN	Not available in B-VII.0	n-un	N/A	N/A	N/A	0.001289	0.01339	10.4
		u-un	N/A	N/A	N/A	0.00124	0.02155	17.4
		n-un + u-un	N/A	N/A	N/A	0.001248	0.01136	9.1
SiC	Not available in B-VII.0	c-sic	N/A	N/A	N/A	0.001219	0.00774	6.3
		si-sic	N/A	N/A	N/A	0.001074	0.00742	6.9
		c-sic + si-sic	N/A	N/A	N/A	0.001182	0.00675	5.7

References

[1] U.S. Department of Energy, "Advanced Small Modular Reactors," [Online]. Available: https://www.energy.gov/ne/nuclear-reactor-technologies/small-modular-nuclear-reactors. [Accessed 8 March 2021].

[2] U.S. Department of Energy, "What is a Nuclear Microreactor?," [Online]. Available: https://www.energy.gov/ne/articles/what-nuclear-microreactor. [Accessed 8 March 2021].

[3] Office of Nuclear Energy, "The BIG Potential for Nuclear Microreactors," 7 August 2019. [Online]. Available: https://www.energy.gov/ne/articles/big-potential-nuclear-microreactors. [Accessed 13 March 2021].

[4] US Department of Energy, "Title 10 - Energy Chapter III - Department of Energy Part 830 - NUCLEAR SAFETY MANAGEMENT," 1 January 2014. [Online]. Available: https://www.govinfo.gov/app/details/CFR-2014-title10-vol4/CFR-2014-title10-vol4-part830. [Accessed 13 March 2021].

[5] US Department of Energy, "HAZARD CATEGORIZATION AND ACCIDENT ANALYSIS TECHNIQUES FOR COMPLIANCE WITH DOE ORDER 5480.23, NUCLEAR SAFETY ANALYSIS REPORTS," US Department of Energy, Washington D.C., 1992.

[6] R. F. Wilson, "SNAP 10A - A Status Report," *Progress in Astronautics and Rocketry*, vol. 16, pp. 581-593, 1966.

[7] D. I. Poston, M. Gibson, T. Godfroy and P. McClure, "Design of the KRUSTY Reactor," in *American Nuclear Society - Nuclear and Emerging Technologies for Space*, LaGrange Park, IL, 2018.

[8] B. H. Yan, C. Wang and L. G. Li, "The technology of micro heat pipe cooled reactor: A review," *Annals of Nuclear Energy*, vol. 135, 2020.

[9] B. A. Gabaraev and Y. S. Cherepnin, "Innovative Designs of Nuclear Reactors," *Nuclear Power and Energy Security*, pp. 235-246, 2010.

[10] International Atomic Energy Agency, "Advances in Small Modular Reactor Technology Developments - A Supplement to: IAEA Advanced Reactors Information System (ARIS)," International Atomic Energy Agency, Vienna, Austria, 2018.

[11] E. M. A. Hussein, "Emerging small modular nuclear power reactors: A critical review," *Physics Open*, vol. 5, pp. 1-19, 2020.

[12] M. Valore and V. N. Kucukboyaci, Interviewees, *The Versatility of Microreactors: Opportunities Beyond Traditional Electrical Power Generation.* [Interview]. 2 April 2021.

[13] R. S. Reid, M. A. Merrigan and J. T. Sena, "Review of liquid metal heat pipe work at Los Alamos," in *AIP Conference Proceedings 217*, 1991.

[14] J. D. Galloway, V. J. Lawdensky, D. I. Poston, H. R. Trellue and M. E. Blood, "Effects of Heat Pipe Failures in Microreactors," Los Alamos National Laboratory, Los Alamos, New Mexico, 2020.

[15] A. Foss, J. Smart, H. Bryan, C. Dieckmann, B. Dold and P. Plachinda, "NRIC Integrated Energy Systems Demonstration Pre-Conceptual Designs," Idaho National Laboratory, Idaho Falls, ID, 2021.

[16] V. Mehta, P. McClure and D. Kotlyar, "Hydrogen Loss Effects on Microreactors for Space and Planetary Nuclear Power Production," in *AIAA Propulsion and Energy Forum*, Indianapolis, 2019.

[17] L. Mason, J. Casani, J. Elliot, J.-P. Fleurial, D. MacPherson, B. Nesmith, M. Houts, R. Bechtel, J. Werner, J. Kapernick, D. Poston, A. L. Qualls, R. Lipinski, R. Radel, S. Bailey and A. Weitzberg, "A Small Fission Power System for NASA Planetary Science Missions," National Aeronautics and Space Administration, Cleveland, Ohio, 2011.

[18] F. Franceschini and B. Petrovic, "Fuel with advanced burnable absorbers design for the IRIS reactor core: Combined Erbia and IFBA," *Annals of Nuclear Energy,* vol. 36, no. 8, pp. 1201-1207, 2009.

[19] D. I. Poston, D. D. Dixon and P. R. e. a. McClure, "A Simple, Low Power Fission Reactor For Space Exploration Power Systems," in *Proceedings for Nuclear and Emerging Technologies in Space,* Albuquerque, NM, 2013.

[20] N. Oi, S. Hirayama, I. Tanabe, A. Muramatsu and T. Kawada, "Preperation of High Density Uranium Nitride and Uranium Carbonitride Fuel Pellets," *Journal of Nuclear Science and Technology,* vol. 9, no. 9, pp. 521-527, 1972.

[21] S. B. Ross, M. S. El-Genk and R. B. Matthews, "Thermal conductivity correlation for uranium nitride fuel between 10 and 1923 K," *Journal of Nuclear Materials,* vol. 151, no. 3, pp. 318-326, 1988.

[22] J. H. Harding and D. G. Martin, "A recommendation for the thermal conductivity of UO2," *Journal of Nuclear Materials,* vol. 166, no. 3, pp. 223-226, 1989.

[23] G. J. Youinou and R. S. Sen, "Impact of Accident-Tolerant Fuels and Claddings on the Overall Fuel Cycle: A Preliminary Systems Analysis," *Nuclear Technology,* vol. 188, no. 2, pp. 123-138, 2014.

[24] B. Feng, E. Shwageraus, F. Benoit and M. S. Kazimi, "Light Water Breeding with Nitride Fuel," *Progress in Nuclear Energy,* vol. 53, no. 7, pp. 862-866, 2011.

[25] X.-C. Ding, T. Kaneshiki, M. Arima, M. Nomura, T. Suzuki and Y. Fujii, "High enrichment of 15N isotope by ion exchange for nitride fuel development," *2008,* vol. 50, no. 2-6, pp. 504-509, Progess in Nuclear Energy.

[26] X. Hu, C. Silva and K. A. Terrani, "Development of Yttrium Hydride Moderator for the Transformational Challenge Reactor," *Transactions of the American Nuclear Society,* vol. 122, no. 1, 2020.

[27] A. P. Shivprasad, T. E. Cutler, J. K. Jewell, V. K. Mehta, S. Widgeon Paisner, C. A. Taylor, C. N. Taylor, H. R. Trellue, D. W. Wootan and E. P. Luther, "Advanced Moderator Material Handbook," Los Alamos National Laboratory, Los Alamos, New Mexico, 2020.

[28] Y. Miao, N. Stauff, S. Bhattacharya, A. Yacout and T. K. Kim, "Advanced Moderation Module - Advanced Moderation Module for High-Temperature Micro-Reactor Applications," Department of Energy, Argonne, 2020.

[29] A. P. Shivpasad, D. M. Frazer, V. K. Mehta, M. W. D. Cooper, T. A. Saleh, J. T. White, J. R. Wermer, E. P. Luther and D. V. Rao, "Elastic moduli of high-density, sintered monoliths of yttrium dihydride," *Journal of Alloys and Compounds,* vol. 826, pp. 1-13, 2020.

[30] X. Hu, D. Schappel, C. M. Silva and K. A. Terrani, "Fabrication of yttrium hydride for high-temperature moderator applicationi," *Journal of Nuclear Materials,* vol. 539, pp. 1-9, 2020.

[31] D. A. Brown and e. al., "ENDF/B-VIII.0: The 8th Major Release of the Nuclear Reaction Data Library with CIELO-project Cross Sections, New Standards and Thermal Scattering Data," *Nuclear Data Sheets,* vol. 148, pp. 1-142, 2018.

[32] J. Leppänen and e. al., ""The Serpent Monte Carlo code: Status, development and applications in 2013."," *Annals of Nuclear Energy,* vol. 82, pp. 142-150, 2015.

[33] J. -P. A. Reiner and M. L. Grossbeck, "Developmemt of Improved Burnable Poisons for Commercial Nuclear Power Reactors," Oak Ridge National Laboratory, Oak Ridge, TN, 2001.

[34] J. W. McMurray, R. D. Hunt, C. M. Silva, G. W. Helmreich and R. L. Seibert, "Production of UN kernels with Gd additive as burnable absorber," U.S. Department of Energy, Oak Ridge, TN, 2018.

[35] G. Kim and S. Ahn, "Thermal conductivity of gadolinium added uranium mononitride fuel pellets sintered by spark plasma sintering," *Journal of Nuclear Materials,* vol. 546, pp. 1-9, 2021.

[36] G. Giudicelli, "Acheivable Power Uprates in Pressurized Water Reactors Using Uranium Nitride Fuel," Massachusetts Institute of Technology, 2017.

[37] J. R. Secker and R. D. Erwin, "ZrB2: The optimum integral fuel burnable absorber for PWRs," in *Transactions of the American Nuclear Society*, Washington, D.C. , 1990.

[38] J. R. Secker, J. E. Prichett, D. Y. Chung and H. W. Keller, "Design and operational experience with Westinghouse ZrB2 integral fuel burnable absorbers in advanced PWR fuel," in *Proceedings of the 1988 International Reactory Physics Conference Vol. 1*, LaGrange Park, IL, 1988.

[39] L. R. Eisenstatt and K. C. Radford, "Method for coating a nuclear fuel with boron nitride". United States Patent 4560575, 24 December 1985.

[40] G. Gündüz, İ. Uslu and H. H. Durmazuçar, "Boron-Nitride Coated Nuclear Fuels," *Nuclear Technology*, vol. 116, no. 1, pp. 78-90, 1996.

[41] G. Gunduz, I. Uslu, C. Tore and E. Tanker, "Boron Nitride Coated Uranium Dioxide and Uranium Dioxide-Gadolinium Oxide Fuels," in *Water reactor fuel element modelling at high burnup and its experimental support*, Windermere, United Kingdom, 1994.

[42] G. Gunduz, "Boron nitride - boron hybrid coating on uranium dioxide-gadolinium oxide fuel," International Atomic Energy Agency, Vienna, Austria, 1997.

[43] H. H. Durmazuçar, Ü. Çolak, B. Sarıkaya and G. Gündüz, "Burnup characteristics and performance of boron nitride and boron coated urania and urania-gadolina fuels," *Nuclear Engineering and Design,* vol. 203, no. 1, pp. 57-64, 2000.

[44] G. E. Spriggs, "Chapter 13.5 - Properties of diamond and cubic boron nitride," in *Materials - Powder Metallurgy Data. Refractory, Hard and Intermetallic Materials*, P. Beiss, R. Ruthardt and H. Warlimont, Eds., Berlin, Springer Materials, 2002, pp. 13.91-13.185.

[45] L. L. Snead and S. J. Zinkle, "Use of Beryllium in Space Reactors," *AIP Conference Proceedings,* vol. 768, p. 746, 2006.

[46] Institute of Rare Earths and Strategic Metals, "Strategic metals prices in February 2020," Institute of Rare Earths and Strategic Metals, 5 February 2020. [Online]. Available: https://en.institut-seltene-erden.de/prices-for-strategic-metals-in-february-2020/. [Accessed 16 June 2021].

[47] C. Fosberg, B. Zohuri and S. Lam, "Heat-Pipe Exchangers for Salt-Cooled Fission and Fusion Reactors to Avoid Salt Freezing and Control Tritium: A Review," *Nuclear Technology,* vol. 206, pp. 1642-1658, 2020.

[48] A. G. Lanin, I. M. Zalivin, V. N. Turchin and E. B. Bojko, "Mechanical properties of zirconium, titanium, and yttrium hydride alloys," *Problemy Prochnosti,* vol. 16, no. 4, pp. 83-88, 1984.

[49] C. L. Whitemarsh, "Review of Zircaloy-2 and Zircaloy-4 Properties Relevant to N. S. Savannah Reactor Design," Oak Ridge National Laboratory, Oak Ridge, TN, 1962.

[50] J. D. Arregui-Mena, R. N. Worth, G. Hall, P. D. Edmondson, A. B. Giorla and T. D. Burchell, "A Review of Finite Element Method Models for Nuclear Graphite Applications," *Archives of Computational Methods in Engineering,* vol. 27, pp. 331-350, 2020.

[51] I. Uslu, U. Colak, M. Tombakoglu and G. Gunduz, "The Production, Characterization, and Neutronic Performance of Boron Nitride Coated Uranium Dioxide Fuel," in *International Conference on CANDU Fuel,* Pembroke, Canada, 1995.

[52] J.-P. A. Renier and M. L. Grossbeck, "Development of Improved Burnable Poisons for Commercial Nuclear Power Reactors (ORNL/TM-2001/238)," Oak Ridge National Laboratory , Oak Ridge, TN, 2001.

[53] H. R. Trellue, J. O'Brien, R. S. Reid, D. Gullien and P. Sabharwall, "Microreactor Agile Nonnuclear Experimental Testbed Test Plan (LA-UR-20-20824)," Los Alamos National Laboratory, Los Alamos, NM, 2020.

[54] A. Peakman, Z. Hodgson and B. Merk, "Advanced micro-reactor concepts," *Progress in Nuclear Energy,* vol. 107, pp. 61-70, 2018.

[55] R. Kimura and S. Wada, "Temperature Reactivity Control of a Calcium-Hydride Moderated Small Reactor Core with Poison Nuclides," *Nuclear Science and Engineering,* vol. 193, no. 9, pp. 1013-1022, 2019.

[56] B. Zohuri, Heat Pipe Design and Technology: Modern Applications for Practical Thermal Management, Alburquerque, NM: Springer, 2016.

[57] J. M. Seitzman, "Stagnation Properties and Mach Number," Georgia Institute of Technology, 2001-2002. [Online]. Available: http://seitzman.gatech.edu/classes/ae3450/stagpropmachnumber.pdf. [Accessed 24 May 2021].

[58] P. K. Holland and R. H. S. Winterton, "The radii of surface nucleation sites which initiate sodium boiling," *Nuclear Engineering and Design,* vol. 24, no. 3, pp. 388-392, 1973.

[59] A. Faghri, "Heat Pipes: Review, Opportunities and Challenges," *Frontiers in Heat Pipes,* vol. 5, no. 1, pp. 1-48, 2014.

[60] A. Ghandi, A. Sharma, R. Pachau, B. Lalremruata, M. Mehta, P. N. Patil, S. V. Suryanarayana, L. S. Danu, B. K. Nayak and A. Kumar, "Neutron radiative capture cross section for sodium with covariance analysis," *The European Physical Journal,* vol. 57, no. 1, pp. 1-12, 2021.

[61] J. H. Rosenfeld, D. M. Ernst, J. E. Lindemuth, J. L. Sanzi, S. M. Geng and J. Zuo, "An Overview of Long Duration Sodium Heat Pipe Tests," in *American Institute of Physics Conference Proceedings 699*, 2004.

[62] B. Holley and A. Faghri, "Permeability and effective pore radius measurements for heat pipe and fuel cell applications," *Applied Thermal Engineering,* vol. 26, pp. 448-462, 2006.

[63] G. Hansen, E. Næss and K. Kristjansson, "Sintered Nickel Powder Wicks for Flat Vertical Heat Pipes," *Energies,* vol. 8, pp. 2237-2357, 2015.

[64] X. Gong Ming, X. Ke Hang, Z. Yong and C. Lin, "Development of sintered Ni-Cu wicks for loop heat pipes," *Science in China Series E: Technological Sciences,* vol. 52, no. 6, pp. 1607-1612, 2009.

[65] D. Deng, D. Yang, Y. Tang, J. Peng, X. Han and M. Pan, "Evaluation of capillary performance of sintered porous wicks for loop heat pipe," *Experimental Thermal and Fluid Science,* vol. 50, pp. 1-9, 2013.

[66] R. A. Lowden, S. D. Nunn, J. O. K. Jr., R. J. Parten and C. D. Bryan, "Powder Metallurgy Fabrication of Molybdenum Accelerator Target Disks," Oak Ridge National Laboratory, Oak Ridge, TN, 2015.

[67] Millipore Sigma, "GF11817907 Nickel Safety Data Sheet," Sigma-Aldrich, 7 Feburary 2021. [Online]. Available: https://www.sigmaaldrich.com/US/en/sds/aldrich/gf11817907?sdslanguage=en. [Accessed 10 June 2021].

[68] R. Cochran and N. Tsoulfanidis, The Nuclear Fuel Cycle: Analysis and Management, LaGrange Park, IL: American Nuclear Society , 1990.

[69] C. W. Kingsbury, *Fuel Cycle Cost and Fabrication Model for Fluoride-Salt High-Temperature Reactor (FHR) "Plank" Fuel Design Optimization,* Atlanta, GA: Georgia Institute of Technology, 2015.

[70] K. Barrett, S. Brag-Sitton and D. Galicki, "Advanced LWR Nuclear Fuel Cladding System Development Trade-off Study (INL/EXT-12-27090)," Idaho National Laboratory, Idaho Falls, 2012.

[71] J. Secker, F. Franceschini and S. Ray, "Accident Tolerant Fuel and Resulting Fuel Efficiency Improvements," in *Advances in Nuclear Fuel Management V (ANFM 2015)*, Hilton Head Island, SC, 2015.

[72] G. R. Robinson, J. M. Hammarstrom and D. W. Olson, "Graphite, Chapter J," in *Critical Mineral Resources of the United States - Economic and Environmental Geology and Prospects for Future Supply*, Reston, VA, U.S. Department of the Interior, 2017.

[73] International Atomic Energy Agency (IAEA), "Approaches for Assessing the Economic Competitiveness of Small and Medium Sized Reactors," International Atomic Energy Agency, Vienna, Austria, 2013.

[74] Nuclear Energy Institute, "Cost-Competitiveness of Micro-Reactors for Remote Markets," Nuclear Energy Institute, 2019.

[75] Massachusetts Institute of Technology, "The Future of Nuclear Energy in a Carbon Constrained World," Massachusetts Institute of Technology, Cambridge, MA, 2018.

[76] G. Holdman, G. Roe, S. Colt, H. Merkel and K. Mayo, "Small Scale Nuclear Power: an option for Alaska? Update January 2021," University of Alaska Fairbanks, Fairbanks, AL, 2021.

[77] J. K. Fink and L. Leibowitz, "Thermodynamic and Transport Properties of Sodium Liquid and Vapor," Argonne National Laboratory, Argonne, IL, 1995.

[78] G. H. Golden and J. V. Tokar, "Thermophysical Properties of Sodium," Argonne National Laboratory, Argonne, IL, 1967.

[79] S. I. Abu-Eishah, "Correlations for the Thermal Conductivity of Metals as a Function of Temperature," *International Journal of Thermophysics,* vol. 22, no. 6, pp. 1855-1868, 2001.

[80] R. E. McFarlane, "New Thermal Neutron Scatttering Files for ENDF/B-VI Release 2," Los Alamos National Laboratory, Los Alamos, 1994.

[81] Nuclear Information Service, "An Introduction to the ENDF Formats," Los Alamos National Laboratory, 23 January 1998. [Online]. Available: https://t2.lanl.gov/nis/endf/index.html. [Accessed 12 April 2021].

[82] C. J. Werner, J. S. Bull, C. J. Solomon and e. al., MCNP6.2 Release Notes, Los Alamos: Los Alamos National Laboratory, 2018.